

University of Nottingham
UK | CHINA | MALAYSIA

Centrifuge tests of monopile foundations under cyclic lateral loading

Kunkun Cheng (ID:4293928)

Nottingham Centre for Geomechanics

The University of Nottingham

Submitted to Proceed to the Degree of Doctor of Philosophy

Abstract

Wind energy has attracted growing interest due to the global energy crisis. This has led to an emphasis on the development of offshore wind turbines (OWTs). Monopile foundations have been widely adopted to support OWTs due to their construction simplicity. The OWT foundation generally undergoes a large number of load cycles as the result of wind, wave and turbine blade rotation. On sustaining such load, pile head rotation must be less than 0.5 degree. In order to meet this requirement, engineers must understand the monopile behaviour under monotonic and cyclic loading.

The design of monopile foundations is based on p-y method, in which soil is treated as a series of non-linear springs. Research on monopile response to lateral loads shows the current design guidance API (2011) overestimate the p-y curves for stiff piles. This may result in uncertainty about the safety of OWTs.

The majority of previous research on this topic has focused on short-term pile response under to cyclic loading and the applied cycles was limited to low thousands. In this study, cyclic loading at least 20,000 cycles was applied to a 60mm model pile, equivalent to a 6m prototype foundation, in sand to investigate the long-term behaviour of pile under cyclic loading. The cyclic loading can be generally classified as one-way (force with a constant direction) and two-way (force direction reversed) load and the magnitude and the bias of the load can vary. A new loading device was developed to apply cyclic loads with different characteristics in the centrifuge. In addition, the pile was instrumented with Fibre Bragg sensors, which allowed the measurement of bending moments along the pile.

The study shows that the pile head displacement accumulates and then levels off in the long

term for one-way tests. For two-way tests, it decreases after the first cycle and then levels off. This suggests that the one-way loading scenario is more damaging for monopile foundations. It was also observed that the stiffness of the pile increases and then stabilise for both one-way and two-way tests. A hyperbolic model was proposed to predict the pile stiffness development. The change in bending moment along the pile during cyclic tests was examined. The results show a reduction in bending moments for both one-way and two-way tests. Cyclic p-y curves were derived based on the bending moment profile of the pile. It is shown that the cyclic p-y curves become stiffer with cycles, which indicates a stiffening soil-pile system.

In addition, a pushover test was performed on the pile and the results confirm that the API method over-predicts the soil response for monopile foundations. Furthermore, the displacement-force curve from monotonic tests can provide useful information for the cyclic test study.

Acknowledgement

I would like to extend my deepest appreciation to my supervisory team for their invaluable guidance and support throughout my PhD journey. Professor Alec Marshall has been particularly approachable, always making time for my questions and concerns. His encouragement and belief in my abilities have been a tremendous source of motivation. Dr. Charles Heron's meticulous attention to detail and willingness to proofread the majority of my thesis greatly enhanced the quality of my work. I am grateful to Dr. Luke Prendergast for his insightful feedback and expertise.

I extend my gratitude to Dr. Geyang Song, whose assistance with the application of fibre Bragg sensors was crucial to the advancement of my experimental work. I am grateful to my colleague and friend, Dr. Jingmin Xu, with whom I have shared countless hours in the centrifuge room, not only advancing our research but also building a mutual support. I also thank Dr Ge Cui for his help.

I must express my sincere appreciation to the team of technicians, Mr Luke Bedford, Mr Steven Lawton, Mr Jim Meakin, Mr Steve Gange and Mr Andrew Maddison. Special thanks to Dr Mir Hashemi Afrapoli, whose expertise in the design of the experimental loading system was invaluable.

I am also grateful to the University of Nottingham for awarding me the Faculty of Engineering Research Excellence PhD Scholarship. The resources and opportunities provided by the university have been fundamental to the completion of my PhD.

Finally, I want to thank my wife, Xingjuan Wu, for the immense happiness and love she has given me. I also thank my father, Liwen Cheng, and my mother, Yuxia Zhang, for their support.

Declaration

I hereby declare that except where specific reference is made to the work of others, the contents of this dissertation are original and have not been submitted in whole or in part for consideration for any other degree or qualification in this, or any other university. This dissertation is my own work and contains nothing which is the outcome of work done in collaboration with others, except as specified in the text.

Kunkun Cheng

March 2024

Contents

Abstract i

Acknowledgement iii

Declaration iv

List of Figures xiii

List of Tables xiv

Nomenclature xiv

1 Introduction **1**

1.1 Aims and objectives 3

2 Literature Review **5**

2.1 Overview 5

2.2 Foundations of offshore wind turbines 5

2.3 OWT Foundation Design Requirements 7

2.3.1 Dimensions of a typical 5MW offshore wind turbine 8

2.3.2 Loads on a typical 5MW OWT 9

2.3.3 Design requirements 10

2.3.3.1 Pile displacement and rotation 10

2.3.3.2 Natural frequency . . . 11
2.4 Monotonic response of monopile foundations . . . 14
2.4.1 Introduction . . . 14
2.4.2 Failure modes of piles . . . 14
2.4.3 Soil Failure Mode . . . 14
2.4.3.1 Ultimate soil resistance . . . 15
2.4.4 p-y method . . . 20
2.4.4.1 Development . . . 20
2.4.4.2 Limitations of p-y method . . . 23
2.4.4.3 Governing differential equation . . . 26
2.4.5 Subgrade reaction approach . . . 27
2.4.6 Elastic Continuum Approach . . . 27
2.5 Cyclic lateral loading effects on pile foundations . . . 28
2.5.1 Introduction . . . 28
2.5.2 The effect of number of load cycles . . . 29
2.5.3 The effect of loading characteristics . . . 31
2.5.4 The effect of loading order . . . 36
2.5.5 The effect of loading direction . . . 37
2.6 Chapter summary . . . 38

3 Methodology **40**

3.1 Introduction . . . 40
3.2 Centrifuge modelling of monopiles in sand . . . 40

3.2.1 The University of Nottingham beam centrifuge . . . 40
3.2.2 Scaling laws . . . 41
3.2.3 Scaling errors . . . 45
3.2.3.1 Scaling of soils . . . 45
3.2.3.2 Variation of the acceleration field . . . 45
3.3 Model preparation . . . 47
3.3.1 Sand preparation . . . 47
3.3.2 The pile . . . 47
3.3.3 Pile installation . . . 48
3.4 Monotonic test kit . . . 51
3.5 Cyclic test kit . . . 53
3.5.1 Introduction . . . 53
3.5.2 Loading principle . . . 53
3.5.3 Control program . . . 56
3.6 Fibre Bragg Grating . . . 58
3.6.1 Introduction . . . 58
3.6.2 Installation of FBGs . . . 59
3.6.3 Calibration of FBGs . . . 59
3.6.3.1 Strain Calibration of FBGs . . . 60
3.7 Measurement and instrumentation . . . 66
3.8 Test procedure and summary of tests . . . 67

4 Monotonic Test Results **68**

4.1 Introduction . . . 68
4.2 Backbone curve . . . 69
4.3 Bending moment evolution . . . 70
4.4 Lateral soil reaction and pile deflection . . . 73
4.5 Derivation of p-y curves . . . 82
4.6 Summary . . . 86

5 Cyclic Test Results **87**

5.1 Introduction . . . 87
5.2 Pile head displacement . . . 89
5.3 Pile secant stiffness . . . 98
5.4 Bending moments . . . 109
5.5 Soil behaviour and pile displacement during cyclic tests . . . 118
5.6 Cyclic p-y curve . . . 123
5.7 Summary . . . 129

6 Practical implications **131**

6.1 Implications for the design . . . 131
6.2 Pile head displacement . . . 131
6.3 Bending moment . . . 132
6.4 Stiffness of the pile-soil system . . . 133

7 Conclusion **135**

7.1 Introduction . . . 135
7.2 Monotonic loading . . . 136

7.3 Cyclic lateral loading 137

7.4 Implication for design 138

7.5 Recommendation for future research 139

References **141**

A Figures: load and pile head displacement during tests **149**

List of Figures

2.1 Foundations for offshore turbine (Doherty and Gavin, 2012) 6

2.2 Growth in size of wind turbines (Koh and Ng, 2016) 8

2.3 The 5 MW reference offshore wind turbine (Katsanos et al., 2017) 9

2.4 Equivalent loads on 5MW offshore wind turbine foundation (modified from Cuéllar, 2011) 10

2.5 Excitation ranges for OWT structures (Arshad and O'Kelly, 2013) 12

2.6 Structural model for wind-turbine system (Arshad and O'Kelly, 2013) 13

2.7 Soil failure mechanisms (Randolph and Gourvenec, 2017) 15

2.8 Soil pressure profile at failure (after Prasad and Chari (1999)) 16

2.9 Ultimate soil resistance behaviour, after Reese et al. (1974) 17

2.10 Distribution of pressures around a laterally loaded pile (Zhang et al., 2005) 20

2.11 C coefficients for API (API, 2011) 21

2.12 Characteristic shape of p-y curves for static and cyclic loading in sand (Reese and Van impe, 2011) 22

2.13 Coefficient k for API (API, 2011) 23

2.14 Parabolic formulation for initial stiffness (Lesny and Wichtmann, 2006) 25

2.15 Pile element (Hetényi, 1946) . . . 26
2.16 Cyclic loading with different ζ_b and ζ_c (LeBlanc et al., 2010a) . . . 31
2.17 Functions relating T_b and T_c to relative density R_d and characteristics of cyclic load (LeBlanc et al., 2010a) . . . 32
2.18 Functions relating K_b and K_c to relative density and characteristics of cyclic load (LeBlanc et al., 2010a) . . . 33
2.19 Envelopes of pile rotation measured for an increasing load sequence and an equivalent decreasing load sequence (LeBlanc et al., 2010b) . . . 37

3.1 Typical sketch of general arrangement of centrifuge, after Ellis et al., 2006 . . . 41
3.2 Inertial stresses in a centrifuge model and gravitational stresses in the corresponding prototype (Taylor, 1995) . . . 42
3.3 Stress variation with depth in a centrifuge model and the prototype (Taylor, 1995) 46
3.4 sand preparation and pile installation . . . 50
3.5 Monotonic test setup . . . 52
3.6 Cyclic test kit . . . 54
3.7 The cyclic load control apparatus . . . 55
3.8 Sketch for load calculation . . . 56
3.9 Fibre Bragg positions on pile . . . 58
3.10 Top view for fibre Bragg cables . . . 59
3.11 Bending calibration setup . . . 63
3.12 Correlation between strains and fibre Bragg wavelength change . . . 64

4.1 Monotonic backbone curve . . . 69

4.2 Measured bending moments 70
4.3 Schematic: bending moment along the pile (prototype scale) 71
4.4 Bending moment above sand surface 72
4.5 Bending moment profile for different head loads with corresponding soil reaction profile derived from polynomial fits 75
4.6 Bending moment (a) and soil reaction (b) along the pile 76
4.7 Pile displacement profile 80
4.8 Rotation depth ratio for loads 81
4.9 Bending moment and pile displacement along the pile 81
4.10 p-y curves at different depths 82
4.11 P-y curves from API and the experiment 84

5.1 Force and pile head displacement for kc02 89
5.2 Force against head displacement for the nth cycle 91
5.3 Force against head displacement for the nth cycle (continued) 92
5.4 One-way 1st cycles 93
5.5 Two-way 1st cycles 94
5.6 Maximum displacement 97
5.7 Minimum displacement 97
5.8 Pile secant stiffness definition 98
5.9 The secant stiffness against cycles 99
5.10 Normalised stiffness against the cycle number 102
5.11 Normalised stiffness against the cycle number (continued) 103

5.12 Normalised stiffness 106

5.13 Coefficients with cyclic magnitude ratio and cyclic loading ratio 107

5.14 Coefficients with cyclic magnitude ratio and cyclic loading ratio 108

5.15 BM development for cycle 1 and 10000 110

5.16 Max normalised BM against cycles 112

5.17 Normalised max BM against cycles 114

5.18 Zero load BM against cycles 115

5.19 Maximum bending moment at 8m depth 117

5.20 Maximum bending moment slope at 8m depth (slope shown in brackets) 117

5.21 Soil reaction and pile displacement: kc01_one+530 ($H_{min} = 0, H_{max} = 530$N) 120

5.22 Soil reaction and pile displacement: kc06_two-180+700 ($H_{min} = -180$N, $H_{max} = 700$N) 121

5.23 Soil reaction and pile displacement: kc07_two+-525 ($H_{min} = -525$N, $H_{max} = 525$N) 122

5.24 p-y cyclic curve: kc01_one+530 ($H_{min} = 0, H_{max} = 530$N) 124

5.25 p-y curves at 9m depth 127

5.26 p-y curves at 9m depth (continued) 128

6.1 Pile head rotation 133

A.1 load during tests 150

A.2 load during tests (continued) 151

A.3 Pile head displacement during tests 152

A.4 Pile head displacement during tests (continued) 153

List of Tables

2.1 Typical design loads for a 2MW turbine LeBlanc et al. (2010a) 11

2.2 Loads frequency (Arshad and O'Kelly, 2013) 12

3.1 Centrifuge scaling laws (Taylor, 1995) 43

3.2 Properties of HST95 Congleton sand (Lauder, 2010) 47

3.3 Properties of the model pile and corresponding prototype monopile 48

3.4 Cyclic test information 57

3.5 1st orientation (P1 at the top) 62

3.6 2nd orientation (S2 at the top) 62

3.7 3rd orientation (P2 at the top) 62

3.8 4th orientation (S1 at the top) 62

3.9 Calibration factors for seven positions 65

3.10 Bending moment factors 66

3.11 Centrifuge tests 67

5.1 Cyclic tests 88

Nomenclature

Roman symbols

ΔF	force applied on the pile, the difference between F_1 and F_2
a, b, c	empirical factors
A_p	cross section area of the pile
C_u	coefficient of uniformity
D	diameter of pile
d_2	distance from the centre of the sliding mass to the cable
d_{50}	average grain size
d_{plate}	length of the plate
E_p	Young's modulus of pile
e_{max}	maximum void ratio
e_{min}	minimum void ratio
E_s	Young's modulus of soil

F_1 force measured by load cell 1

F_2 force measured by load cell 2

FM_1 bending moment at Position 1

g gravitational acceleration

G_s specific gravity

$H_{\max}$ maximum load of the cyclic loading

$H_{\min}$ minimum load of the cyclic loading

H_{ref} reference horizontal load capacity

$H_{N,\max}$ maximum load at the N_{th} cycle

$H_{N,\min}$ minimum load at the N_{th} cycle

I_p second moment area of pile

I_D relative density

k calibration factor

K_1 secant stiffness of the first cycle

k_1 bending moment factor at Position 1

K_a active earth pressure coefficient

K_N secant stiffness of the N^{th} cycle

K_p passive earth pressure coefficient

L pile length

L_{em} pile embedded depth

M bending moment

M_1 mass of dead weight

M_2 sliding mass

M_{total} total mass of the plate

N the number of load cycles

N_g stress-based scaling factor

N_s geometrical scaling factor

p soil reaction

t_p wall thickness of pile

y pile displacement

$y_{N,\max}$ maximum displacement at the N_{th} cycle

$y_{N,\min}$ minimum displacement at the N_{th} cycle

Y_N pile head displacement after N cycles

z pile depth

Greek symbols

$\Delta\lambda$ change of fibre reading wavelength

ϵ strain

γ' effective unit weight of the soil

$\gamma_{\text{dry,max}}$ maximum dry unit weight

$\gamma_{\text{dry,min}}$ minimum dry unit weight

κ the accumulation rate of pile secant stiffness

ϕ'_{crit} critical friction angle

ϕ'_{peak} peak friction angle

ρ density

ρ'_{sat} buoyant density

σ_v vertical stress

ζ_b cyclic magnitude ratio

ζ_c cyclic loading ratio

Chapter 1

Introduction

The demand for renewable energy has grown significantly over the last decades, driven by concerns over climate change, diminishing fossil fuel resources, and the desire for energy security. As a response to this problem, many countries have put great effort into the development of wind energy. Hence, many offshore wind farms have been constructed around the world. The expenditure of the construction is usually extremely high. The cost of foundations accounts for about 20% of the total expenses of a project (Oh et al., 2018). Therefore, the design of foundations for offshore wind turbines (OWTs) needs to be given proper consideration. Moreover, the foundations are commonly subjected to various loads: wind loads, current loads, wave loads and the self-weight. These loads result in significant horizontal cyclic loads and vertical dead loads, which can be detrimental to the OWT performance. In order to make sure OWT foundations meet serviceability requirements through their entire life-cycle, the design of foundations also requires critical attention. There are several types of foundations used for OWTs, namely gravity foundations, monopile foundations, jacket foundations and floating structure foundations (Doherty and Gavin, 2012). Monopile foundations have been mostly utilised and represent

78.8% of foundations for installed OWTs (EWEA, 2014). The popularity of monopile foundations is attributed to the simplicity of construction and relatively low cost.

Given the prevalence of monopile foundations, their design should undergo strict scrutiny to ensure the durability and reliability of the foundations. However, the design codes (API, 2011 and DNV, 2016) may not be satisfactory with respect to several factors. Firstly, the current design codes are based on oil and gas platforms, which have dissimilar loading conditions and geometries. The loads on oil and gas platforms are dominated by vertical loading with relatively small lateral loading. In contrast, OWTs are primarily subjected to lateral loading and the vertical loading is relatively small. Secondly, the design requirements of platforms consider the ultimate limit state, whereas OWTs are governed by serviceability limit state requirements where the foundation displacements and rotations are crucial. Thirdly, the codes in use are based on a small number of load cycles, however, OWT foundations will experience an extremely large number of load cycles during their life cycle. Therefore, the current codes for the design of monopile foundations could be improved. This leads to the need for research on the response of monopile foundations subjected to a large number of load cycles.

Research on this topic has involved both experiments and numerical simulations. In terms of experimental approaches, there are three methods: 1-g tests, N-g tests, and full-scale tests. In this study, the focus is on N-g tests, in which geotechnical centrifuges are used to investigate monopiles under cyclic loads. Most research employing this method applies only a small number of cycles, which may not accurately represent long-term behavior. Consequently, this study aims to bridge this gap by applying a large number of cycles, seeking to understand the long-term response of monopiles subjected to cyclic loads. To achieve this, a new device was developed to apply cyclic loads with large numbers of cycles in the centrifuge. Before conduct-

ing cyclic tests, monotonic tests, in which an increasing one-way load is applied to the pile, were carried out to demonstrate pile response under monotonic loads and also provide a reference to cyclic tests. From monotonic tests, the change of pile head displacement will be demonstrated in response to a monotonic load. In addition, the displacement and soil reaction along the pile can be obtained from bending moments measured by fibre optic strain sensors installed on the pile. The soil response at a certain depth can then be obtained by combining the soil reaction and pile displacement. This soil response at all depths is referred to as p-y curves, which are the core of the API method. The p-y curves from experiments will be compared with those of the API method. The results from monotonic tests can also provide a reference for cyclic tests as the cyclic tests begin with a section of increasing one-way force. In terms of cyclic tests, results from a programme of cyclic tests are presented, using the developed loading device to apply cyclic loads with different characteristics, including one-way and two-way loading and varying loading magnitude. Through these tests, the long-term behavior of the pile and soil will be demonstrated and the effects of loading analyzed. These include pile head displacement, pile stiffness, soil reaction, pile displacement along the pile, and cyclic p-y curves. This study provides valuable data showing the long-term response of piles under cyclic loading and analysis explaining the effects of different cyclic loading on pile behaviour.

1.1 Aims and objectives

The aim of this project is to achieve a better understanding of the long-term behaviour of offshore wind turbine monopile foundations. Offshore wind farms located in the North Sea are considered in this research, which are typically within sandy deposits (Kirkwood, 2015). The

study will focus on the response of monopiles subjected to a large number of load cycles in sand. The long-term effects of cyclic loading characteristics on pile-soil stiffness and pile head displacement are of interest. The objectives are listed below.

1. To design and develop a novel loading device capable of applying cyclic loading of various loading characteristics in a centrifuge. This experimental equipment will enable the acquisition of a novel data set of piles under cyclic loading of various characteristics in sand.

2. To carry out centrifuge monotonic tests of an instrumental pile in the same configuration as cyclic tests. The experimental p-y curves from monotonic tests will be compared with p-y curves used in the API method to show the validity of the API method.

3. To demonstrate the development of pile head displacement, secant pile-soil stiffness, and pile bending moments over a large number of load cycles and analyse the effects of loading characteristics on these parameters. This will provide valuable insights on the pile response under cyclic loading and show the validity of findings from previous research.

4. To derive soil reactions and pile displacements along the pile from bending moments over cycles and show their development with load cycles. Cyclic p-y curves will be derived based on soil reaction and pile displacement data. The effects of load cycles and loading characteristics on p-y curves will be analysed to better understand the soil behaviour of the pile-soil system under cyclic loading.

Chapter 2

Literature review

2.1 Overview

This section provides a literature review for research on monopiles under cyclic loading as well as some background about offshore wind turbine structures. Firstly, information about OWT foundations is presented, including foundation types, loads on foundations, and design requirements. Secondly, previous research on monotonic load effects on monopile foundations is summarised. Thirdly, cyclic lateral load effects on pile foundations reported by other researchers are introduced.

2.2 Foundations of offshore wind turbines

Various types of foundations have been used for OWTs, including gravity base foundations, monopile foundations, jacket structure foundations, and floating foundations. The foundation used in a specific project depends on the loads, the water depth, and the seabed sediment. Fig-

ure 2.1 shows these foundations schematically. These foundations are explained in detail in the following text.

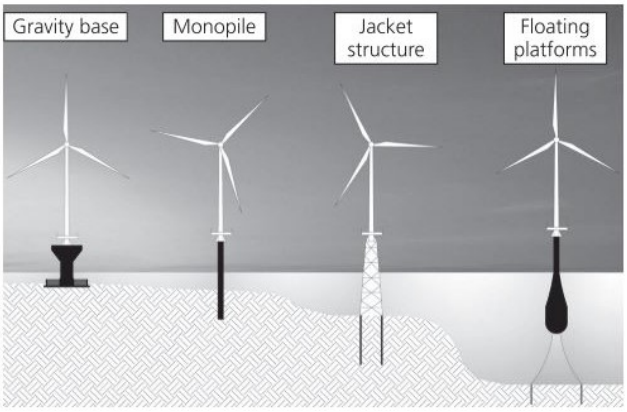


Figure 2.1: Foundations for offshore turbine (Doherty and Gavin, 2012)

1. Gravity base foundation

   Gravity foundations consist of a large block made of concrete or steel. They secure the turbine through their significant weight. Such a foundation requires a large base area to resist the overturning of the turbine. Consequently, seabed preparation is necessary before constructing a gravity base foundation. These foundations are typically used in shallow water since the cost of transporting them to deeper waters is prohibitive, and the overturning moment becomes significant in deeper water.

2. Monopile foundation

   A monopile is a single, large-diameter, open-ended steel tube. It stabilises the turbine by mobilising the horizontal earth pressure of the soils. Owing to its simple geometry, it's convenient to manufacture and transport to the construction site. As monopiles are open-ended tubes, they are typically driven into the seabed, making their installation straightforward. Monopiles are economical for use in water depths up to 35m (Doherty and Gavin,

2012).

3. Jacket structure foundation

   The jacket structure foundation consists of a three or four-legged steel lattice frame anchored to the seabed using a single pile beneath each leg. It is typically used in water depths ranging from 35 to 60m. Since it offers minimal resistance to ocean waves and current flow, it is suitable for severe maritime conditions. Furthermore, the requirement for seabed preparation is relatively low, allowing it to be installed in complex site conditions without compromising the structure's stiffness (Arshad and O'Kelly, 2013).

4. Floating foundation

   The floating foundation secures the turbine using catenary mooring, making it suitable for very deep waters. Research is ongoing to address new design challenges. In the future, it might be possible to commercialise this type of foundation. However, its commercial viability remains uncertain (Doherty and Gavin, 2012).

Among the various foundation systems, monopile foundations are immensely popular in shallow waters. Therefore, this research will focus on monopile foundations.

2.3 OWT Foundation Design Requirements

The size of offshore wind turbines has been steadily increasing, as illustrated in Figure 2.2. To optimise economic benefits, 5MW wind turbines are gaining popularity due to their overall cost reduction per rated MW. 5MW offshore wind turbines can be supported by monopiles with diameters ranging from 5m to 7.5m and are typically installed in water depths of approximately

30m (Koh and Ng, 2016). A majority of studies have focused on relatively smaller diameter piles (D<5m). There's a pressing need to understand the complex behaviour of large diameter piles when subjected to cyclic loading. Consequently, this research considers the large diameter monopile for 5MW offshore wind turbines.

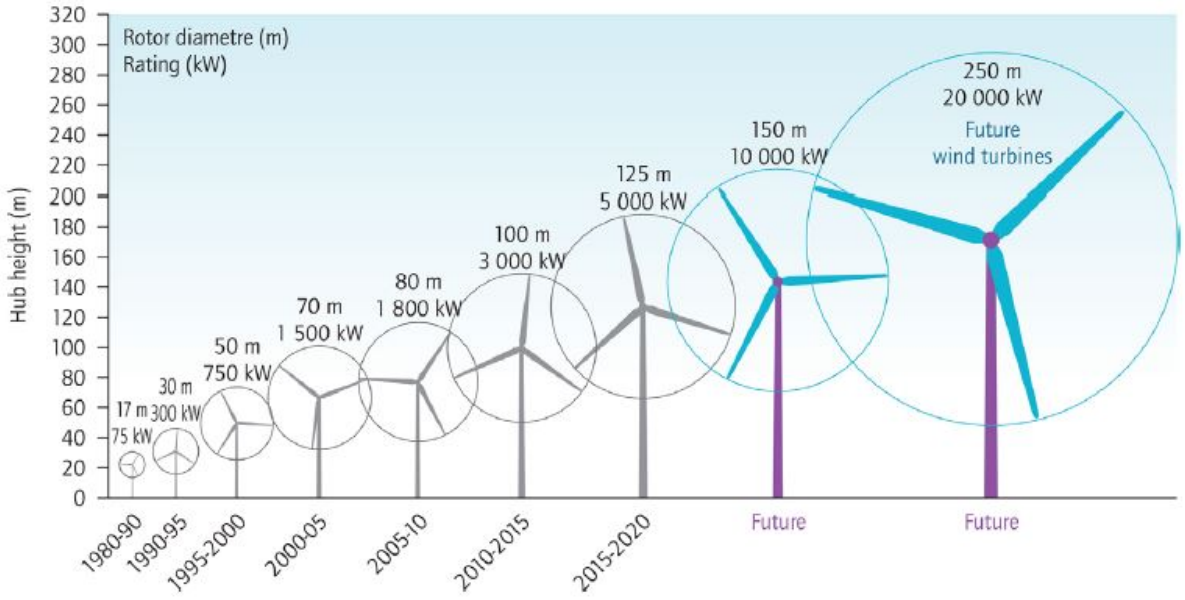


Figure 2.2: Growth in size of wind turbines (Koh and Ng, 2016)

2.3.1 Dimensions of a typical 5MW offshore wind turbine

The monopile for a 5MW OWT typically has a diameter ranging from 6 to 8m, a wall thickness varying between 0.05 to 0.1m, and an embedded depth of 20 to 40m (Achmus and Abdel-Rahman, 2005). The properties of a reference monopile for a 5MW OWT are described by Katsanos et al. (2017), as illustrated in Figure 2.3.

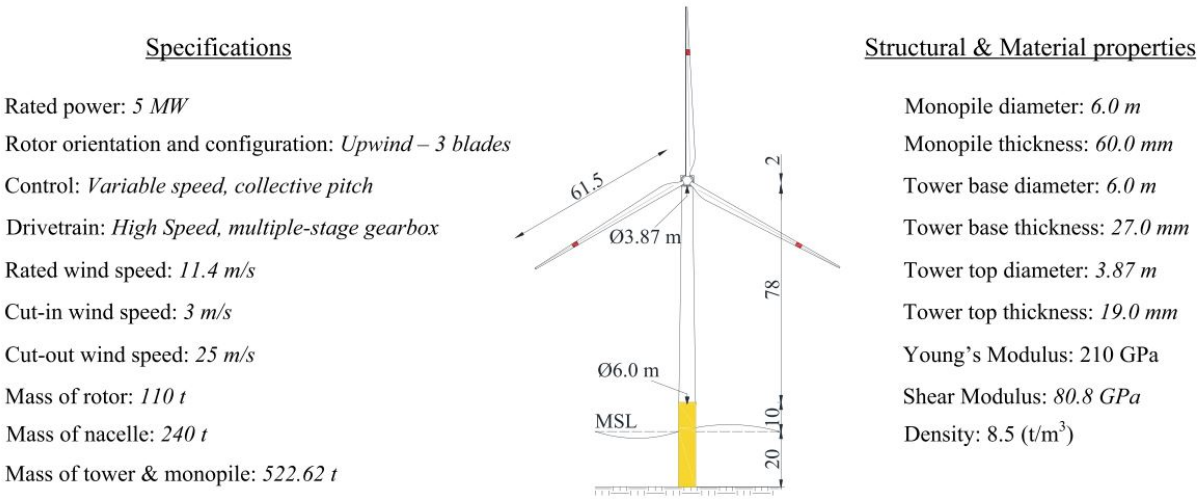


Figure 2.3: The 5 MW reference offshore wind turbine (Katsanos et al., 2017)

2.3.2 Loads on a typical 5MW OWT

The loads exerted on an OWT encompass its dead weight, wind loading, hydrodynamic loading, rotational loading, and blade loading. Clearly, wind loading arises from wind action. Hydrodynamic loading stems from currents and waves; its magnitude is influenced by wave kinematics, density, water depth, and the shape of the foundation (Cuéllar, 2011). Rotational loading is a cyclic load originating from the eccentricity of the turbine rotors, while blade loading arises due to changes in aerodynamics as a blade passes the tower. These loads impose significant horizontal force and a moment on the monopile foundation. This force can be decomposed into a resultant force that acts on a monopile with an eccentricity accounting for the bending moment. As illustrated in Figure 2.4, an equivalent lateral load (H) is applied to a 5MW offshore wind turbine monopile foundation. This load has a lever arm (L_e) measured from the seabed surface, and it induces a corresponding moment ($M = H * L_e$) from the eccentric load (not depicted in the figure).

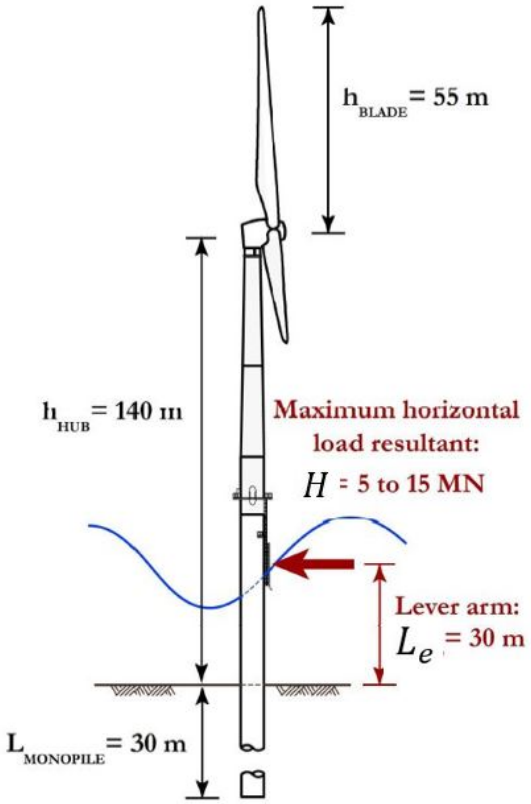


Figure 2.4: Equivalent loads on 5MW offshore wind turbine foundation (modified from Cuéllar, 2011)

2.3.3 Design requirements

2.3.3.1 Pile displacement and rotation

The design of offshore wind turbines (OWTs) is governed by three criteria: the ultimate limit state (ULS), the serviceability limit state (SLS), and the fatigue limit state (FLS). The ULS pertains to the maximum load capacity of the foundations. The SLS defines the state up to which the OWT can function correctly, while the FLS sets the threshold beyond which the structure may fail due to cumulative loading effects. Notably, the design of OWTs is primarily driven by the serviceability limit state. To satisfy the SLS, Achmus et al. (2009) posits that the pile head rotation should not exceed 0.5 degrees. Additionally, Malhotra (2007) suggests that the pile head

deflection be confined within 10% to 20% of the pile diameter. LeBlanc presents design loads for a 2MW OWT in Table 2.1. The methodologies for load calculations are provided in DNV GL (2016). Given these stringent limits, accurately predicting pile head displacement and rotation becomes imperative.

Table 2.1: Typical design loads for a 2MW turbine LeBlanc et al. (2010a)

	Number of cycles	Moment (MNm)	Lateral load (MN)	Vertical Load (MN)
ULS	1	95	4.6	5.0
SLS	10^2	45	2.0	5.0
FLS	10^7	28	1.4	5.0

2.3.3.2 Natural frequency

The fundamental natural frequency of an OWT plays a crucial role in its design. Resonance can occur if the frequency of external forces aligns closely with this fundamental natural frequency, leading to heightened stress within the structure. Consequently, the OWT's design must ensure that its natural frequency does not match the frequencies of external forces (Bhattacharya et al., 2013; Arshad and O'Kelly, 2013).

As previously discussed, an OWT is exposed to various dynamic loads, including wind loading, hydrodynamic loading, rotational loading, and blade loading. The frequencies of these loads are presented in Table 2.2 (Arshad and O'Kelly, 2013). Notably, wind loads exhibit a low frequency. This low frequency arises because wind loads are deemed quasi-steady, attributed to the vast windward area (Journée and Massie, 2001).

The frequency range of the turbine rotor is commonly referenced as the first excitation frequency, denoted as '1P'. For a three-bladed turbine, the blade passing frequency range is termed as '3P'. These frequencies are depicted in Figure 2.5. Within this figure, the frequency range

Table 2.2: Loads frequency (Arshad and O'Kelly, 2013)

Load type	Frequency
Wind loading	less than 0.1Hz
Hydrodynamic loading	0.07- 0.5Hz
Rotational loading	0.17-0.33Hz
Blade loading	0.5-1Hz

prior to 1P is labelled as the soft-soft zone. The interval between 1P and 3P is designated as the soft-stiff zone. The range beyond 3P represents the stiff-stiff zone. The design frequency of the OWT is strategically positioned within the soft-stiff zone (DNV GL, 2016; Ward, 2016). Both the soft-soft and stiff-stiff zones are deemed undesirable for design purposes and are thus avoided. Structures in the soft-soft zone are viewed as overly flexible, leading to deflections that exceed serviceability limits. Conversely, structures in the stiff-stiff zone can become excessively rigid, resulting in redundant material use and superfluous costs.

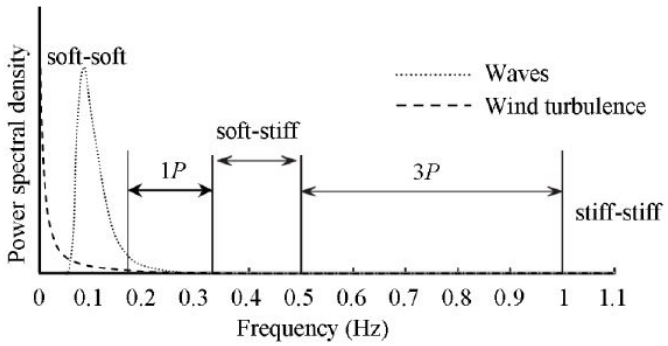


Figure 2.5: Excitation ranges for OWT structures (Arshad and O'Kelly, 2013)

Estimating the fundamental natural frequency of a monopile foundation is feasible. An OWT can be conceptualized as a cantilevered vertical strut, depicted in Figure 2.6. In this representation, the turbine's mass is treated as a point load at the monopile foundation's apex. Thus, the natural frequency can be approximated using Equation 2.1 (Arshad and O'Kelly, 2013).

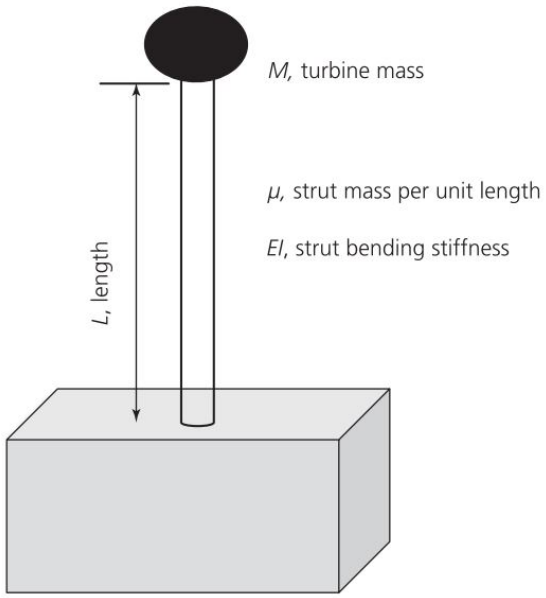


Figure 2.6: Structural model for wind-turbine system (Arshad and O'Kelly, 2013)

$$f_{\text{nat}}^2 = \frac{3.04}{4(\pi)^2} \frac{EI}{(0.227\mu L + M)L^3} \tag{2.1}$$

where μ is the strut mass per unit length, L is the length of the monopile foundation and EI is its flexural stiffness. The strength of this method lies on its simplicity of computation and clear mechanical interpretation. However, it is limited to long and flexible pile foundations. An alterative is the rotational spring method where the foundation is modelled as a beam hinged at a rotation centre and constrained by a rotational spring. This model is considered more reliable as it took into consideration of soil-pile interaction and thus was adopted to calculate the overall natural frequency of offshore wind turbine with large diameter and rigid foundations (Wang et al., 2022). In addition, the stiffness of the rotational spring changes over cycles. Since there is a connection between the stiffness and the natural frequency of offshore wind turbines, it is necessary to investigate the change of stiffness to ensure the natural frequency is within the soft-stiff zone through the life-span of offshore wind turbines.

2.4 Monotonic response of monopile foundations

2.4.1 Introduction

In order to properly support wind turbines, monopile foundations must resist significant lateral loads and moments originating from various sources. The main considerations in the design process encompass two aspects. The first is related to preventing excessive lateral deflection and rotation of the pile. The second aims to prevent pile failure concerning soil and pile strength (Randolph and Gourvenec, 2017). This underscores the importance of understanding the pile foundation's response to monotonic loads.

2.4.2 Failure modes of piles

Poulos and Hull (1989) introduced a criterion to determine the failure mode of a pile based on the magnitude of the rigidity parameter, R. This parameter is given by:

$$R = \left(\frac{E_p I_p}{E_s}\right)^{0.25} \tag{2.2}$$

where E_p is the Young's modulus of the pile, I_p is the moment of inertia of the pile, and E_s represents Young's modulus of soil. According to Poulos and Hull (1989), a pile is deemed rigid if its length is less than $1.48R$ and considered flexible if its length exceeds $4.44R$.

2.4.3 Soil Failure Mode

Theoretically, two different failure mechanisms were proposed based on proximity to the ground surface and at depth:

1. Close to the ground surface, an assumption was made that a conical wedge forms ahead of the pile and is lifted, as shown in Figure 2.7. Behind the pile, a gap forms. This wedge overcomes the friction between the pile, shear within the soil, and its self-weight.

2. Below a certain depth, the wedge is not likely to occur. Instead, the soil tends to flow around the pile, as illustrated in Figure 2.7. This is due to the low resistance offered by a flow mechanism.

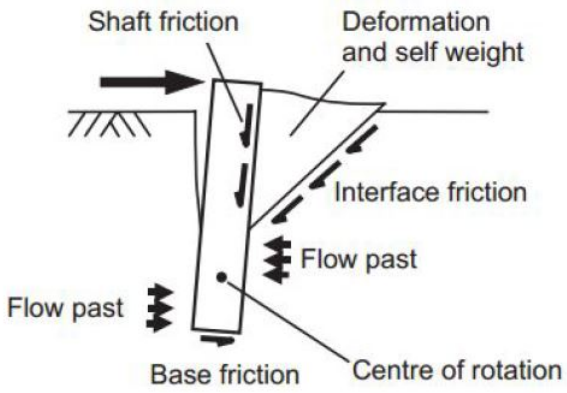


Figure 2.7: Soil failure mechanisms (Randolph and Gourvenec, 2017)

2.4.3.1 Ultimate soil resistance

Hansen (1961) assumed that the soil pressure reverses below the rotation point, as depicted in Figure 2.8. He proposed that the ultimate soil resistance can be calculated using Equation 2.3.

$$P_u = (q_z k_q^z + c k_c^z) D \tag{2.3}$$

where q_z represents the sum of the passive and active earth pressures, given by $q_z = k_p + k_a$. The term c denotes the cohesion, while k_q^z and k_c^z are factors dependent on the effective friction angle.

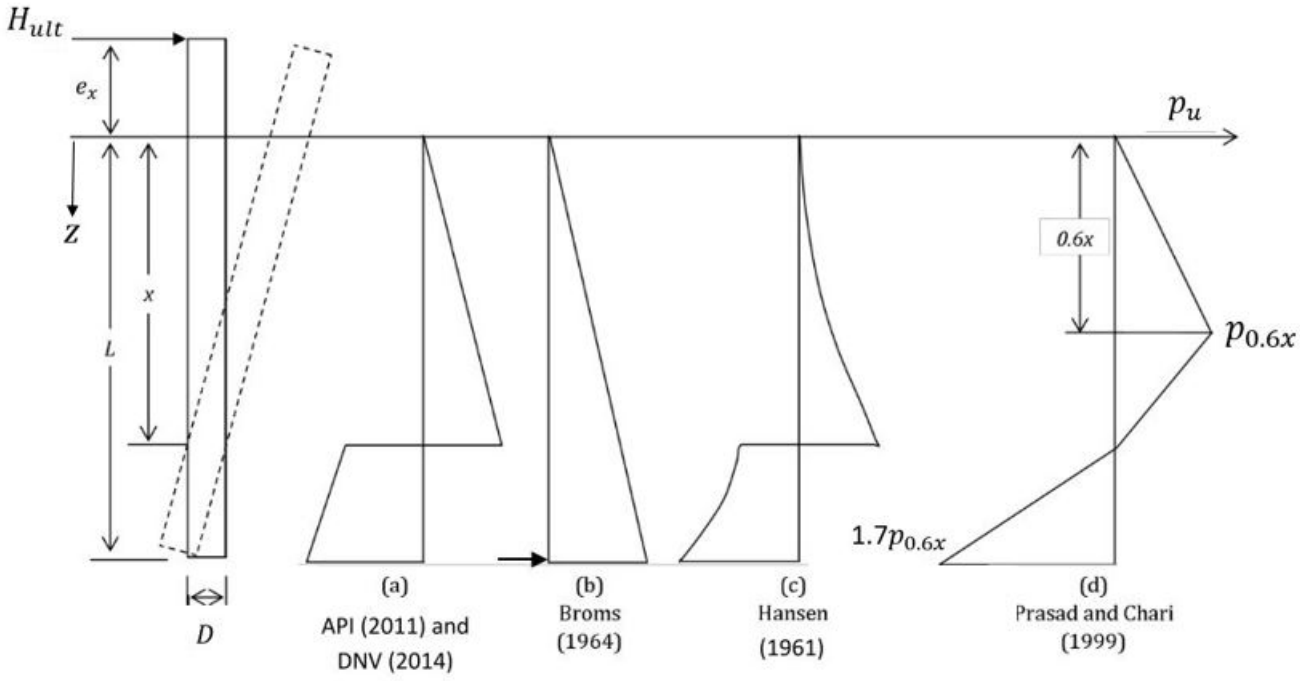


Figure 2.8: Soil pressure profile at failure (after Prasad and Chari (1999))

Broms (1964) conducted small-scale tests on rigid piles subjected to lateral loads. From his experiments, he deduced that the ultimate lateral resistance in cohesionless soil can be approximated by

$$P_u = 3K_p\gamma zD \tag{2.4}$$

where K_p is the passive earth pressure coefficient. Broms suggested that the soil pressure profile at failure assumes a triangular shape, with a point load representing the soil pressure below the rotation point, as illustrated in Figure 2.8.

Reese et al. (1974) proposed equations to calculate the ultimate soil resistance, assuming that the soil adheres to the Mohr-Coulomb criterion. At shallow depths, a wedge failure mechanism was considered. The interface between the pile and the soil is assumed to be frictionless. Although this assumption may not hold as the soil-pile interaction will lead to an increasing

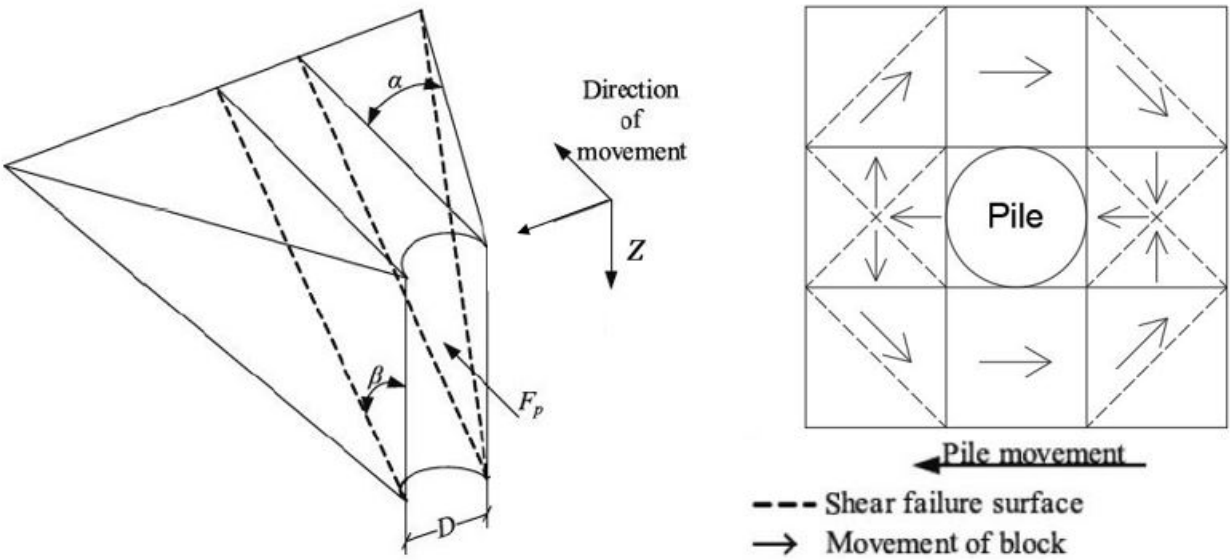


Figure 2.9: Ultimate soil resistance behaviour, after Reese et al. (1974)

friction between soil and pile, it offers a way to establish an analytical model. The ultimate soil resistance is calculated using Equation 2.5. The dimensions of the wedge are depicted in Figure 2.9(a).

$$p_{u,\text{shallow}} = \gamma' z\Big[D(K_p - K_a) + z(K_p - K_0)\sqrt{K_p}\tan\alpha + zK_0\sqrt{K_p}(\frac{1}{\cos\alpha} + 1)\tan\phi'\sin\beta\Big] \quad (2.5)$$

where γ' is the effective unit weight of the soil, z represents depth, $K_a = \tan^2(\pi/4 - \phi'/2)$ is the active earth pressure coefficient, K_p is the passive earth pressure coefficient, ϕ' is the internal friction angle, D is the diameter, K_0 is the in situ lateral pressure coefficient, and α and β are the wedge dimensions as illustrated in Figure 2.9(a), which relate to the relative density and applied load.

At greater depths, the ultimate soil resistance is predicted using Equation 2.6, which is based

on the flow mechanism. A schematic representation of this is depicted in Figure 2.9(b).

$$p_{u,\text{deep}} = \gamma' z D(K_p^3 + K_0 K_p^2 \tan\phi' - K_a) \tag{2.6}$$

The ultimate soil resistance is determined by the lesser magnitude of the two modes mentioned above. An empirical parameter, denoted as A, is introduced to adjust the value, ensuring that the theoretical results align with the test outcomes.

$$p_u = \min\{A p_{u,\text{shallow}}, A p_{u,\text{deep}}\} \tag{2.7}$$

$$A \approx 3 - 0.8\frac{z}{D} \geq 0.9 \tag{2.8}$$

Prasad and Chari (1999) suggested that the soil pressure at the rotation point is zero since no strain occurs at the point, as shown in Figure 2.8. Small scale tests using a pressure transducer on a rigid pile were conducted to investigate the ultimate soil resistance. It was found that the maximum soil pressure above the rotation point is at a depth of $0.6x$, where x is the depth of the rotation point. The magnitude of this maximum soil pressure is given by Equation 2.9. The lateral soil pressure at the pile toe was measured as $1.7p_{0.6x}$. Straight lines were assumed to connect these two points and the rotation point, as depicted in Figure 2.8.

$$p_{0.6x} = [10^{1.3\tan\phi + 0.3}]\gamma(0.6x) \tag{2.9}$$

The ultimate lateral load at the pile head and the depth of the rotation point can be derived by considering horizontal and moment equilibrium. The results are presented in Equation 2.10

and Equation 2.12, respectively.

$$H_{\text{ult}} = \int_0^L 0.8pDdz \tag{2.10}$$

$$H_{\text{ult}} e_x = \int_0^L 0.8pDzdz \tag{2.11}$$

$$x = \frac{1}{2.1996}\left[-(0.567 + 1.7\text{e}_x) + (5.307L^2 + 7.29\text{e}_x^2 + 10.541\text{e}_x L)^{0.5}\right] \tag{2.12}$$

Zhang et al. (2005) considered the friction of the soil-pile interface and proposed Equation 2.13 to calculate the ultimate soil resistance. Figure 2.10 illustrates the pressure distribution around the pile.

$$p_u = (0.8p_z + \tau_z)D \tag{2.13}$$

$$p_z = K_p \gamma' z \tag{2.14}$$

$$\tau_z = K_h \gamma' z \tan\delta \tag{2.15}$$

where K_h is the lateral earth pressure coefficient; K_p is the passive earth pressure coefficient; δ is the angle of friction at the soil-pile interface.

API (2011) and DNV (2014) simplified the equations proposed by Reese et al. (1974) and provided the following equations to calculate the ultimate soil resistance. This method is commonly adopted by industry.

$$p_u = \min\left\{c_1 z + c_2 D, c_3 D\right\}\gamma' z \tag{2.16}$$

where γ' is the effective soil weight. Coefficients c_1, c_2 and c_3 are dependent on the internal friction angle determined from the Figure 2.11.

The PISA (Pile-Soil Analysis) joint industry project aimed to improve monopile foundation

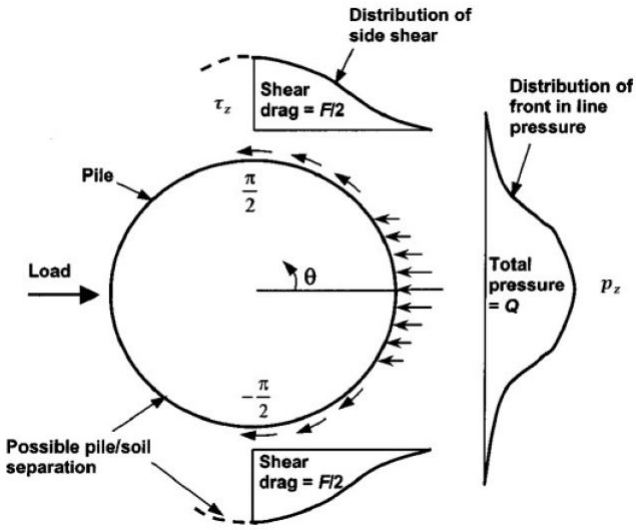


Figure 2.10: Distribution of pressures around a laterally loaded pile (Zhang et al., 2005)

design through field testing, numerical modelling, and a new design methodology (Burd et al., 2020). A field test in Dunkirk, France, on dense to medium-dense sand investigated monopile behaviour under monotonic loading, reflecting offshore wind turbine conditions in the North Sea (McAdam et al., 2020). The study used 14 steel, open-ended piles with length-to-diameter (L/D) ratios from 3 to 10 and diameters of 0.273 m, 0.762 m, and 2.0 m by impact driving method. Results indicated stiffness and strength increased with the increasing length for medium-diameter piles. In addition, It is shown the pile behaviour transitions from flexural to rotational deflection modes as the L/D ratio decreases.

2.4.4 p-y method

2.4.4.1 Development

The p-y method is an extension of the Winkler model, which was developed by Winkler (Winkler, 1867). Winkler initially treated the soil as linear springs. The principle behind the p-y method

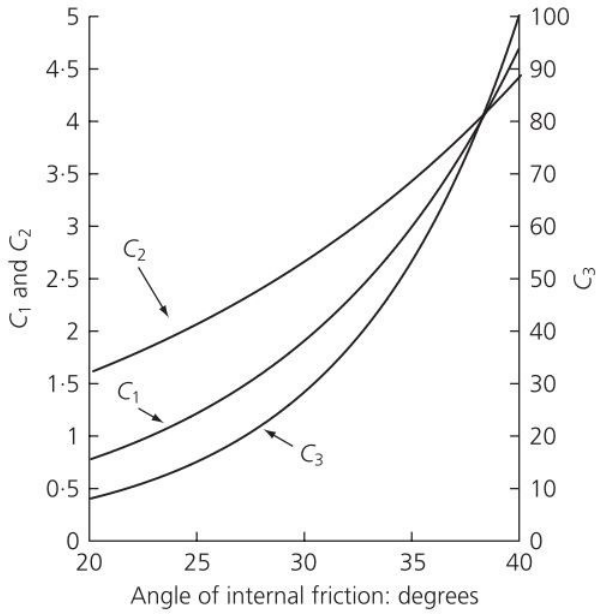


Figure 2.11: C coefficients for API (API, 2011)

involves modelling the deforming soil around the pile as independent non-linear springs. Central to the p-y method is the p-y curve, which describes the relationship between lateral load and displacement. This curve varies with depth along the pile. At a specific depth, the slope of a straight line connecting the origin to a point on the p-y curve is termed the secant stiffness of the p-y response (E_{py}). This is expressed in Equation 2.17. It is crucial to distinguish between the soil resistance acting on a pile per unit length (P) and the net pressure exerted on the pile (p). The relationship between these two parameters is detailed in Equation 2.18.

$$E_{py} = \frac{P}{y} \tag{2.17}$$

$$P = pD \tag{2.18}$$

Reese et al. (1974) provided a detailed procedure for developing the p-y curve for short-term static loading. This procedure is based on full-scale pile tests conducted at Mustang Island. Figure 2.12 illustrates a set of p-y curves. The curve begins with a linear portion, represented as $p = E_{py}^{0} y$. Subsequently, it transitions into a parabolic section after the displacement of $\frac{b}{60}$ (b is the pile diameter). After this segment, a linear relationship is observed, culminating at the ultimate soil resistance (p_u). Comprehensive explanations regarding the calculations of parameters shown in Figure 2.12 can be found in Reese et al. (1974).

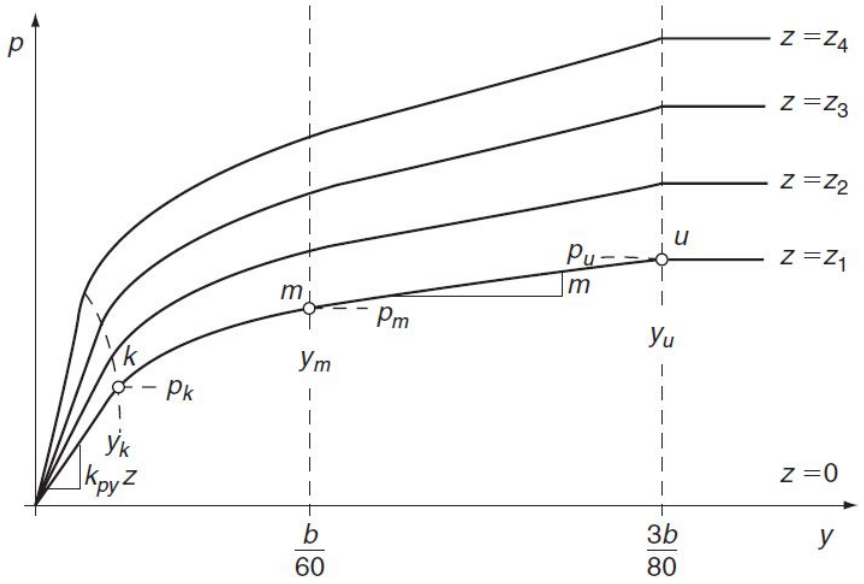


Figure 2.12: Characteristic shape of p-y curves for static and cyclic loading in sand (Reese and Van impe, 2011)

A considerable amount of research has been dedicated to the development of p-y curves. Murchison and O'Neill (1984) simplified the p-y curves proposed by Parker and Reese (1970) by introducing new factors varying with effective soil friction angle, ensuring that the mean square error in predicting pile head displacement was minimised.

The design codes from API (2011) and DNV (2014) integrated the p-y curves of Reese et al.

(1974) and Murchison and O'Neill (1984), presenting Equation 2.19 for p-y curves. The equations put forth by API and DNV are recognised as the current p-y method and are widely accepted in the industry.

$$p = Ap_u \tanh\left[\frac{kz}{Ap_u}y\right] \tag{2.19}$$

where k is the initial modulus of subgrade reaction, which is determined from Figure 2.13, p_u is defined in Equation 2.16, and A is estimated by Equation 2.8 ($A \approx 3 - 0.8\frac{z}{D} \geq 0.9$).

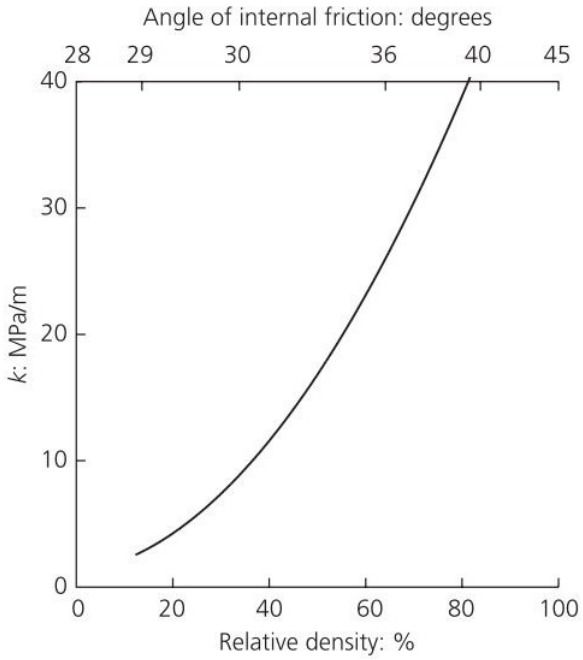


Figure 2.13: Coefficient k for API (API, 2011)

2.4.4.2 Limitations of p-y method

Several limitations are associated with the p-y method. The p-y method is based on the database provided by Reese et al. (1974) and Murchison and O'Neill (1984), which includes the behaviour of flexible piles up to a 1.22m diameter. This inevitably introduces some uncertainties about the p-y method.

1. The pile stiffness: The p-y method is verified for small-diameter flexible piles. However, for large-diameter piles, they tend to behave rigidly. Consequently, the validity of the method for such piles becomes uncertain. Considering that monopile foundations for OWTs are generally large diameter and exhibit stiff behaviour, it's essential to examine the appropriateness of using the existing p-y method to predict the behaviour of these stiff piles.

2. The initial stiffness: The initial stiffness of the p-y curves proposed by API and DNV is based on the assumption that the initial stiffness of the p-y curves increases linearly with depth. This can be observed in Equation 2.20. Reese et al. (1974),Terzaghi (1955) and Veric (1961) suggested the linear relationship is suitable for flexible piles.

$$E_{si} = \frac{dp}{dy}\Big|_{y=0} = AP_u \frac{(\frac{kz}{AP_u})}{\cosh^2(\frac{kz}{AP_u}y)}\Big|_{y=0} = kz \tag{2.20}$$

Lesny and Wichtmann (2006) recommended a parabolic relation between initial stiffness and depth for large diameter piles, as shown in Equation 2.21

$$E_{si} = E_{si,ref}\left(\frac{z}{z_{ref}}\right)^a \tag{2.21}$$

where $E_{si,ref}$ and z_{ref} are parameters determined from Figure 2.14, and a is selected as 0.6 to give the best fit in the study.

Sørensen (2012) suggested the initial stiffness is dependent on the depth, the pile diameter, and the soil modulus. Small-scale tests in a pressure tank were conducted with the application of a surcharge to the soil such that the soil properties for the small-scale tests

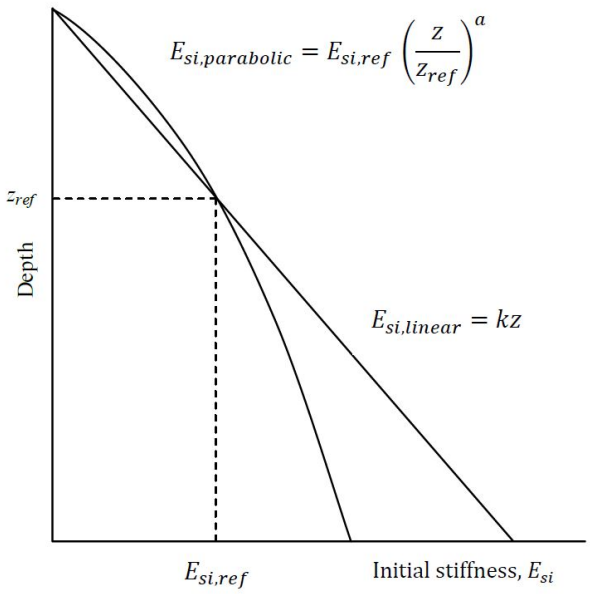


Figure 2.14: Parabolic formulation for initial stiffness (Lesny and Wichtmann, 2006)

are similar to the soil properties for sand around full-scale foundations. The relation is shown in Equation 2.22.

$$E_{si} = a\left(\frac{z}{z_{ref}}\right)^b\left(\frac{D}{D_{ref}}\right)^c\left(\frac{E_{si}}{E_{si,ref}}\right)^d \tag{2.22}$$

In this equation, z_{ref}, D_{ref}, and $E_{s,ref}$ are 1m, 1m, and 1MPa, respectively. The parameters a, b, c, and d are suggested to be 1000kPa, 0.3, 0.5, and 0.8, respectively, for the best fit. The soil modulus E_s is estimated using Equation 2.23, as proposed by Ibsen et al. (2009).

$$E_s = (1.15I_D + 20000)\left(\frac{\sigma_3^{'}}{100kPa}\right)^{0.58} \tag{2.23}$$

where I_D is the relative density and $\sigma_3^{'}$ is the confining pressure (kPa).

Klinkvort (2012) adopted a linear relation for the initial stiffness of rigid piles. Kirkwood (2015) proposed a bi-linear relation, suggesting that the slope of the initial stiffness line

changes after the rotation point for a rigid pile. To date, many researchers have carried out investigations on the initial stiffness for rigid piles, but the outcomes remain inconclusive.

3. The shear between Winkler Springs: The p-y method was developed using Winkler springs. This introduces a fundamental error associated with the p-y method as the shear stresses between the Winkler springs are ignored.

2.4.4.3 Governing differential equation

To implement the p-y method, it is crucial to solve a governing differential equation. The derivation of this equation has been presented by Hetényi (1946). The derivation assumes small deflections and a smooth soil-pile interface.

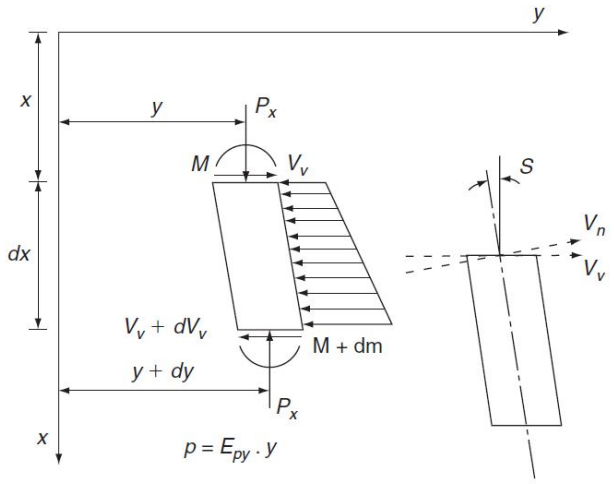


Figure 2.15: Pile element (Hetényi, 1946)

Considering a pile element as shown in Figure 2.15, the moment equilibrium results in the following equations.

$$(M + dM) - M + P_x dy - V_v dx = 0 \tag{2.24}$$

$$\frac{d^2M}{dx^2} + P_x \frac{d^2y}{dx^2} - \frac{dV_v}{dx} = 0 \tag{2.25}$$

Based on beam theory,

$$\frac{d^2M}{dx^2} = E_p I_p \frac{d^4y}{dx^4} \tag{2.26}$$

$$\frac{dV_v}{dx} = p = E_{py} y \tag{2.27}$$

The equation yields the governing differential equation 2.28.

$$E_p I_p \frac{d^4y}{dx^4} + P_x \frac{d^2y}{dx^2} + E_{py} y = 0 \tag{2.28}$$

where $E_p I_p$ is the pile stiffness.

2.4.5 Subgrade reaction approach

The subgrade reaction approach represents the earliest application of the Winkler method, wherein soil is modeled as a series of springs. The stiffness of these springs corresponds to the subgrade reaction modulus, K $[FL^{-2}]$. Additionally, K represents the initial gradient of the p-y curve. Matlock and Reese (1960) provided a closed-form solution to determine pile head deflection and rotation. It was assumed that K increased linearly with depth, given by the relationship $K = n_k z$, where n_k is the coefficient of subgrade reaction $[FL^{-3}]$.

2.4.6 Elastic Continuum Approach

The elastic method was formulated to precisely determine pile head displacement and rotation in an elastic soil. Based on an elastic and homogeneous soil with consistent stiffness and Poisson's ratio, Poulos (1971) developed specific equations. The friction between the soil and

pile was disregarded in this derivation. Furthermore, Randolph (1981) introduced solutions of a similar form for soils where the stiffness increases linearly with depth, given by Equation 2.29 and 2.30.

$$Y = I_{YH}\frac{H}{E_s L} + I_{YM}\frac{M}{E_s L^2} \tag{2.29}$$

$$\theta = I_{\theta H}\frac{H}{E_s L^2} + \theta_{YM}\frac{M}{E_s L^3} \tag{2.30}$$

where I_Y and I_θ are the influence factors for displacement and rotation, respectively. H and M refer to the influences accounting for horizontal load and moment separately.

The prerequisite of the elastic method is the elastic behaviour of soils. This is reasonably achieved when considering small pile deflection. The critical issue with this method is the determination of soil properties. This method relies heavily on the soil stiffness or shear modulus, which is challenging to determine in practice.

2.5 Cyclic lateral loading effects on pile foundations

2.5.1 Introduction

Since OWTs are commonly subjected to significant long-term cyclic loading resulting from environmental loads, the effect of cyclic loading on the foundation is a major design consideration. The current design codes, API and DNV, suggest degrading the ultimate soil resistance to account for cyclic loads with more than 50 load cycles (as shown in Equations 2.31 to 2.33). This suggestion is based on findings from the Mustang Island tests (Reese et al., 1974 and Cox et al., 1974). However, these tests applied only a small number of load cycles (fewer than 200 cycles), which is significantly fewer than the approximately 10^7 cycles of loading that a real OWT will

experience over a lifetime of 20 years. As a result, the current design codes may be insufficient for the design of OWT monopile foundations. It is crucial to predict the pile response to a large number of cyclic loads to ensure compliance with serviceability requirements. Several factors require investigation, including the number of load cycles, loading characteristics, loading order, and loading direction.

$$p = Ap_u \tanh\left[\frac{kz}{Ap_u}y\right] \tag{2.31}$$

Static loading $$A = 3 - 0.8\frac{z}{D} \geq 0.9 \tag{2.32}$$

Cyclic loading $$A = 0.9 \tag{2.33}$$

2.5.2 The effect of number of load cycles

Little and Briaud (1988) proposed the following equations to predict the lateral pile displacement after N cycles based on 6 full-scale tests using concrete and steel piles. In contrast to the API, they suggested that the soil resistance remained constant during cyclic loading.

$$p(N) = p(1) = \text{constant} \tag{2.34}$$

$$y(N) = y(1)N^{\alpha} \tag{2.35}$$

where $y(1)$ and $y(N)$ are lateral deformations in the first and Nth load cycles respectively, and α is an empirical parameter.

Long and Vanneste (1994) compared results of 34 full-scale pile tests in sand and proposed an empirical model (represented by Equation 2.36) to predict the pile head displacement. The

tests includes a wide range of soil density, pile type and material, construction technique, and cyclic load characteristics. In this model, it is assumed that the soil modulus increases linearly with depth. The model takes into account the effects of the number of load cycles, soil density, characteristics of the cyclic load, and the pile installation method.

$$Y_N = \frac{AH}{EI^{0.4}K_{hN}^{0.6}} + \frac{BM}{EI^{0.6}K_{hN}^{0.4}} \tag{2.36}$$

$$K_{hN} = K_{h1}N^{-t} \tag{2.37}$$

$$\zeta_c = \frac{H_{\min}}{H_{\max}} \tag{2.38}$$

where K_{h1} and K_{hN} are the coefficients of soil reaction for the 1st and Nth load cycles, respectively, A and B are constants accounting for the pile geometry and stiffness, t relates to cyclic loading ratio (ζ_c), pile installation method and relative density of sand, and H and M are the lateral load and bending moment, respectively. The cyclic loading ratio (ζ_c) is defined by the ratio of minimum and maximum lateral loads. It was found that one way loading ($\zeta_c = 0$) gives rise to greater displacements than partial unloading($\zeta_c > 0$).

In contrast, Lin and Liao (1999) compared 26 full-scale tests in sand with different relative density and suggested a logarithm relationship between the accumulated displacement of a pile and the number of load cycles, as represented by Equation 2.39.

$$Y_N = Y_1(1 + \beta \ln(N)) \tag{2.39}$$

where $Y(1)$ and $Y(N)$ are lateral deformations in the first and Nth load cycles respectively, and

β is an empirical parameter.

2.5.3 The effect of loading characteristics

Cyclic loading characteristics include the cyclic magnitude ratio, ζ_b, and cyclic loading ratio (or cyclic ratio), ζ_c, as defined as follow:

$$\zeta_{\mathrm{b}} = \frac{H_{\max}}{H_{\mathrm{ref}}} \tag{2.40}$$

$$\zeta_{\mathrm{c}} = \frac{H_{\min}}{H_{\max}} \tag{2.41}$$

where H_{ref} is the reference horizontal load capacity of the pile, and $H_{\max}$ and $H_{\min}$ are the maximum and minimum load of the cyclic loading, respectively. For one-way cyclic loading, ζ_c is equal to 0. For two-way cyclic loading, ζ_c is less than 0. Notably, $\zeta_c = -1$ represents symmetrical two-way cyclic loading. Figure 2.16 shows cyclic loading with varying characteristics concerning cyclic loading ratio and cyclic magnitude ratio.

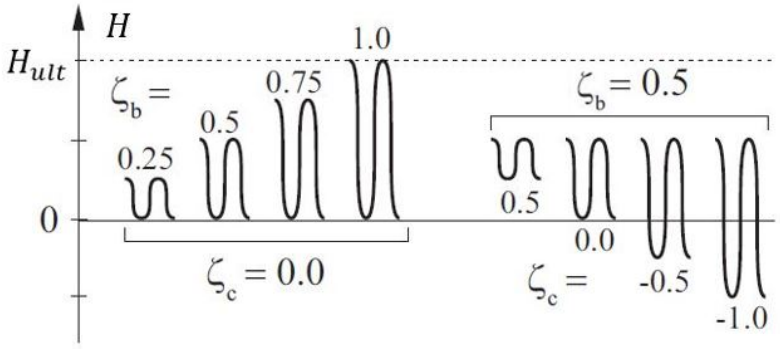


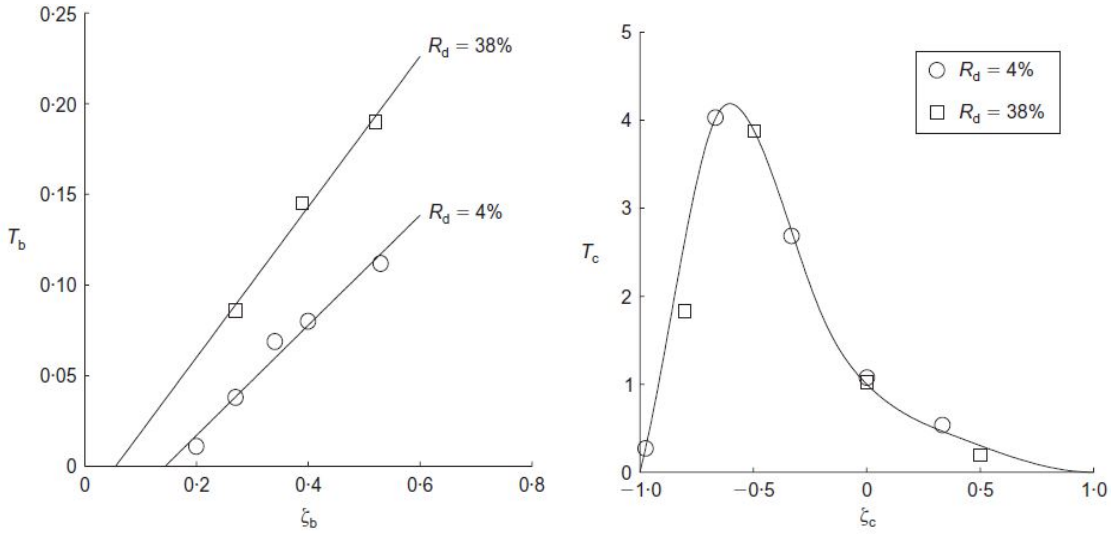
Figure 2.16: Cyclic loading with different ζ_b and ζ_c (LeBlanc et al., 2010a)

LeBlanc et al. (2010a) conducted a series of tests on stiff piles subjected to tens of thousands of lateral load cycles in drained sand at 1-g. The 80mm copper pile is equivalent to a proto-

type pile with a diameter of 4m. The results showed that the logarithmic equation provided an accurate fit for the accumulated pile head rotation for a number of load cycles less than 100. However, for larger numbers of load cycles, the logarithmic equation underestimated the accumulated rotation, and an exponential relation was a better fit for the results. The authors proposed that the accumulated rotation was related to the relative density, cyclic loading ratio, and cyclic magnitude ratio, as shown in Equation 2.42.

$$\frac{\theta_N}{\theta_s} = T_b(\zeta_b, I_D)\, T_c(\zeta_c) N^{0.31} \tag{2.42}$$

where θ_s is the rotation of the pile under the equivalent maximum cyclic load in a monotonic test. The dimensionless function T_b is dependent on relative density and cyclic magnitude ratio, while the dimensionless function T_c solely depends on the cyclic loading ratio. These functions were derived through curve fitting, as illustrated in Figure 2.17.



(a) T_b (b) T_c

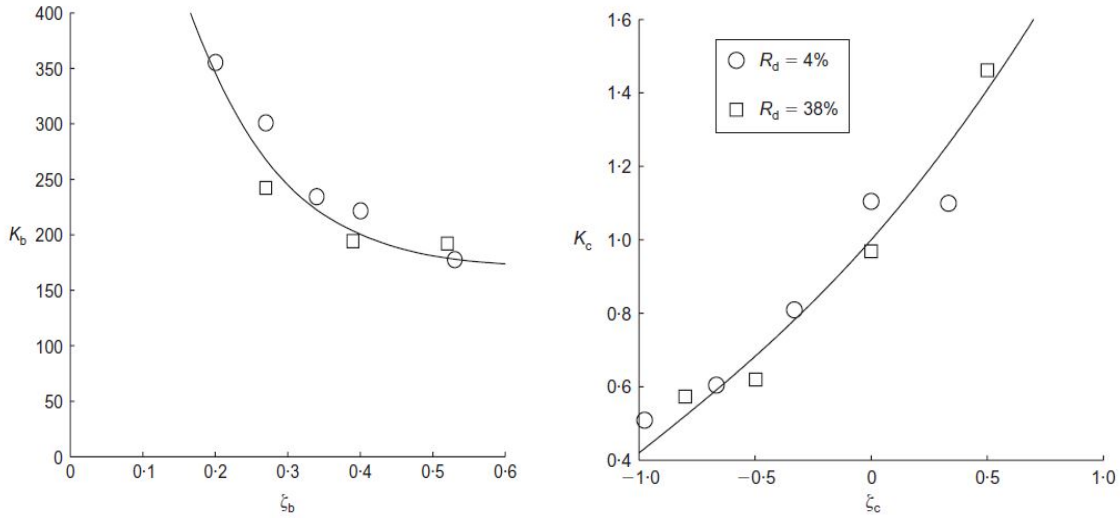
Figure 2.17: Functions relating T_b and T_c to relative density R_d and characteristics of cyclic load (LeBlanc et al., 2010a)

It was also pointed out that the dimensionless pile secant stiffness increases logarithmically with load cycles.

$$\tilde{k}_N = \tilde{k}_0 + A_k \ln(N) \tag{2.43}$$

$$\tilde{k}_0 = K_b(\zeta_b) K_c(\zeta_c) \tag{2.44}$$

where A_k is a dimensionless constant independent of both cyclic loading characteristics and the relative density. $K_b(\zeta_b)$ and $K_c(\zeta_c)$ are dimensionless functions determined by curve fitting, as shown in Figure 2.18.



(a) K_b (b) K_c

Figure 2.18: Functions relating K_b and K_c to relative density and characteristics of cyclic load (LeBlanc et al., 2010a)

It was observed that the highest accumulated rotation occurred for loading with $\zeta_c = -0.6$. This was four times greater than that observed in the one-way loading case. Taking into account the empirical dimensionless function T_c, the accumulated rotation for two-way loading was generally larger than for one-way loading.

Klinkvort and Hededal (2012) performed 12 cyclic centrifuge tests on monopiles in sand to

investigate the effects of cyclic loading characteristics on change of pile stiffness and accumulation of pile head displacements. The results confirmed that pile secant stiffness can be fitted well through a logarithmic function.

$$K_N = K_1(1 + \kappa \ln(N)) \tag{2.45}$$

The accumulation rate (κ) is dependent on the cyclic magnitude ratio and cyclic loading ratio, as shown in Equation 2.46.

$$\kappa(\zeta_c, \zeta_b) = \kappa_c(\zeta_c)\kappa_b(\zeta_b) \tag{2.46}$$

In order to determine the effects of both cyclic magnitude ratio and cyclic loading ratio, the influence of cyclic magnitude ratio was assumed to be linear with the accumulation rate. Consequently, the function of the cyclic loading ratio was derived through division. The two resulting empirical functions are presented below:

$$\kappa_c(\zeta_c) = -6.92\zeta_c + 1 \tag{2.47}$$

$$\kappa_b(\zeta_b) = 0.05\zeta_b + 0.02 \tag{2.48}$$

The secant stiffness of the first cycle was related to the secant stiffness of the monotonic test by the equation below,

$$K_1(\zeta_c, \zeta_b) = K_c(\zeta_c)K_s(\zeta_b) \tag{2.49}$$

The functions $K_b(\zeta_b)$ and $K_c(\zeta_c)$ are dependent on the cyclic magnitude ratio and cyclic load-

ing ratio, respectively, as shown in the following equations.

$$K_c(\zeta_c) = 1.64\zeta_c^2 + 3.27\zeta_c + 3.27 \tag{2.50}$$

$$K_s(\zeta_b) = \frac{P(\zeta_b)}{Y(\zeta_b)} \tag{2.51}$$

The results also confirmed that the accumulation of pile head displacement can be accurately described by a power function.

$$Y_N = Y_1 N^{\alpha} \tag{2.52}$$

The coefficient α is associated with both cyclic magnitude ratio and cyclic loading ratio. These two factors were assumed to be independent. In a similar manner, the linear effect of cyclic magnitude ratio on the coefficient was imposed. The functions were determined as follows,

$$\alpha(\zeta_c, \zeta_b) = T_c(\zeta_c) T_b(\zeta_b) \tag{2.53}$$

$$T_b(\zeta_b) = 0.61\zeta_b - 0.013 \tag{2.54}$$

$$T_c(\zeta_c) = (\zeta_c + 0.63)(\zeta_c - 1)(\zeta_c - 1.64) \tag{2.55}$$

Differentiation of $T_c(\zeta_c)$ indicates that the largest pile head displacement occurs for $\zeta_c = 0$. That means one-way cyclic loading is the most critical case. The results were based on tests using a 40mm steel model pile corresponding to a 3m diameter prototype pile. For larger piles, the relationships above require further verification. The prerequisite of the design framework

is that monopiles are installed in dense saturated sand under drained conditions. This drained condition is an reasonable assumption as the permeability of sand is relatively high.

2.5.4 The effect of loading order

Lin and Liao (1999) developed equations to predict the pile head displacement after N_a cycles of magnitude a followed by N_b cycles of magnitude b using the superposition theory. A logarithmic relationship between the accumulated displacement of a pile and the number of load cycles was adopted in the derivation. The derivation is given as follows:

The pile head displacements under a single load cycle of magnitude a after N_a load cycles is Y_{N_a}, calculated by Equation 2.39,

$$Y_{N_a} = Y_{1a}(1 + \beta_a \ln(N_a)) \tag{2.56}$$

Considering the pile then experienced a different cyclic loading of magnitude b, the same displacement could be achieved after N_b^* load cycles.

$$N_b^* = e^{\left(\frac{\frac{Y_{Na}}{Y_{1b}} - 1}{\beta_a}\right)} \tag{2.57}$$

$$Y_{N_a} = Y_{N_b^*} = Y_{1b}(1 + \beta_b ln(N_b^*)) \tag{2.58}$$

Hence, the pile head displacement under two subsequent sets of cyclic loads of magnitude a and b, after N_a and N_b load cycles, respectively, is calculated by,

$$Y_{N(a+b)} = Y_{1b}(1 + \beta_b ln(N_b^* + N_b)) \tag{2.59}$$

LeBlanc et al. (2010b) conducted two small-scale tests at 1-g to examine the proposal. The first test applied three sets of cyclic loads with loading magnitude 28%, 41%, and 53%, each after 1000 cycles, in an increasing order. The results were compared with the displacement obtained using Equation 2.59, and the error was less than 6%. The other test applied three sets of one-way cyclic loads (A, B, and C) with different magnitudes ($\zeta_{b,A} = 0.28, \zeta_{b,B} = 0.41$ and $\zeta_{b,C} = 0.53$) after different numbers of cycles: 10000, 100 and 10, respectively. These loads were applied in both increasing and decreasing orders. The results showed a small discrepancy between the different orders, as depicted in Figure 2.19. Peralta and Achmus (2010), on the other hand, observed a 25% difference in displacement for two different loading orders. These tests were also conducted at 1g.

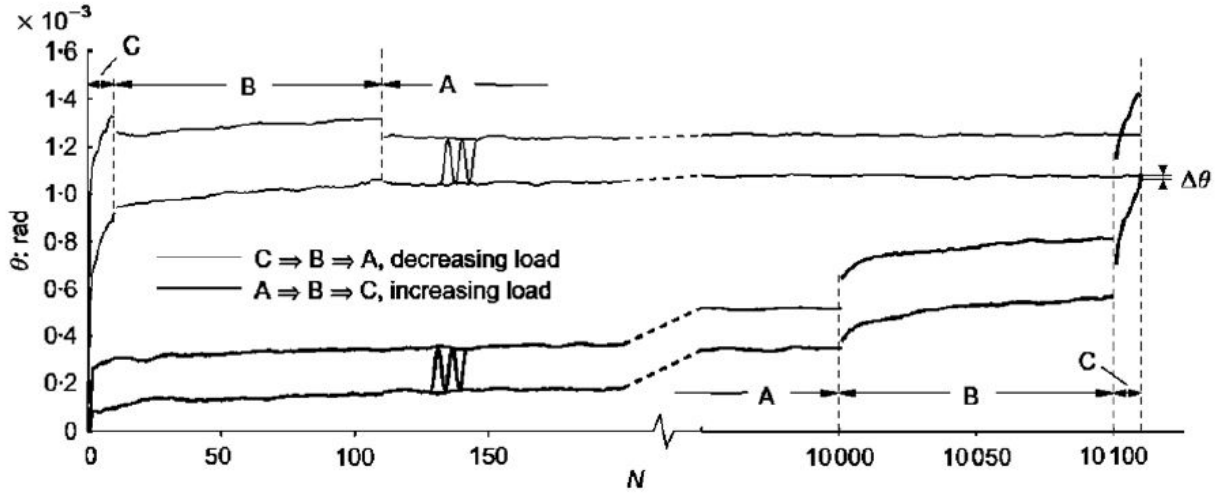


Figure 2.19: Envelopes of pile rotation measured for an increasing load sequence and an equivalent decreasing load sequence (LeBlanc et al., 2010b)

2.5.5 The effect of loading direction

The environmental loads on offshore wind turbines (OWTs) can vary in direction, resulting in multi-directional lateral cyclic loading. This variability in loading direction has the potential

to cause larger displacements and pose safety risks to OWTs. However, information about specific loading patterns on OWTs is often deemed confidential by corporations and is therefore unavailable to researchers. In the absence of this data, it becomes crucial to investigate the effects of various loading patterns on OWTs. Su and Yan (2013) and Nanda et al. (2017) conducted small-scale tests to investigate the pile response to loading of variable directions. In both tests, multi-directional lateral cyclic loading led to higher displacements compared to uni-directional loading.

2.6 Chapter summary

This chapter provided a literature review on monopiles under monotonic and cyclic loading. The following key points have been highlighted and will be further investigated in this study.

1. P-y curves in current design guidelines (API method) are based on flexible piles. For monopile foundations, which are considered to be stiff piles, the p-y formulation needs to be examined to determine the applicability of current design codes. This will be accomplished by performing monotonic tests on monopiles. The resulting p-y curves from these tests will then be compared with those from the design codes. In addition, cyclic p-y curves from the API method will be compared to the experimental cyclic p-y curves to show the validity of the method.

2. Much research has focused on investigating the response of monopiles under cyclic loading. However, most centrifuge studies have been confined to a limited number of cycles. The majority of these studies indicate a logarithmic relationship between pile head displacement and the number of load cycles. This relationship will be assessed for monopiles

subjected to a significant number of cycles (10^4). Additionally, the evolution of pile secant stiffness over numerous load cycles will be presented and compared with findings from other research.

3. To date, there is no consensus regarding the effect of the cyclic loading ratio on pile head displacements. The influence of cyclic loading characteristics, including cyclic loading ratio and cyclic magnitude ratio, on monopile foundations will be explored after ten thousand load cycles in sand.

Chapter 3

Methodology

3.1 Introduction

Geotechnical centrifuge testing will be employed as the main tool to investigate the the topic of this thesis. The application of centrifuge testing can achieve stress similarity between a full-scale prototype and a small-scale model by increasing the acceleration field of the small scale model. Centrifuge modelling allows the accurate simulation of the behaviour of soil in small scale models, since the soil behaviour is stress dependent.

3.2 Centrifuge modelling of monopiles in sand

3.2.1 The University of Nottingham beam centrifuge

The centrifuge is a medium-sized beam centrifuge with a swing platform. A illustration of the centrifuge is provided in Figure 3.1. The centrifuge is capable of spinning to 150 g (where g is gravity) and carrying a maximum payload of 500kg on the platform (at a reduced g-level). A

counterweight is located on the opposite side of the beam from the soil model to balance the centrifuge during flight. At the centre of the centrifuge are fluid/electric/data slip rings which allow water and high pressure air, power supply, and data transfer to be supplied/acquired to/from the model during tests.

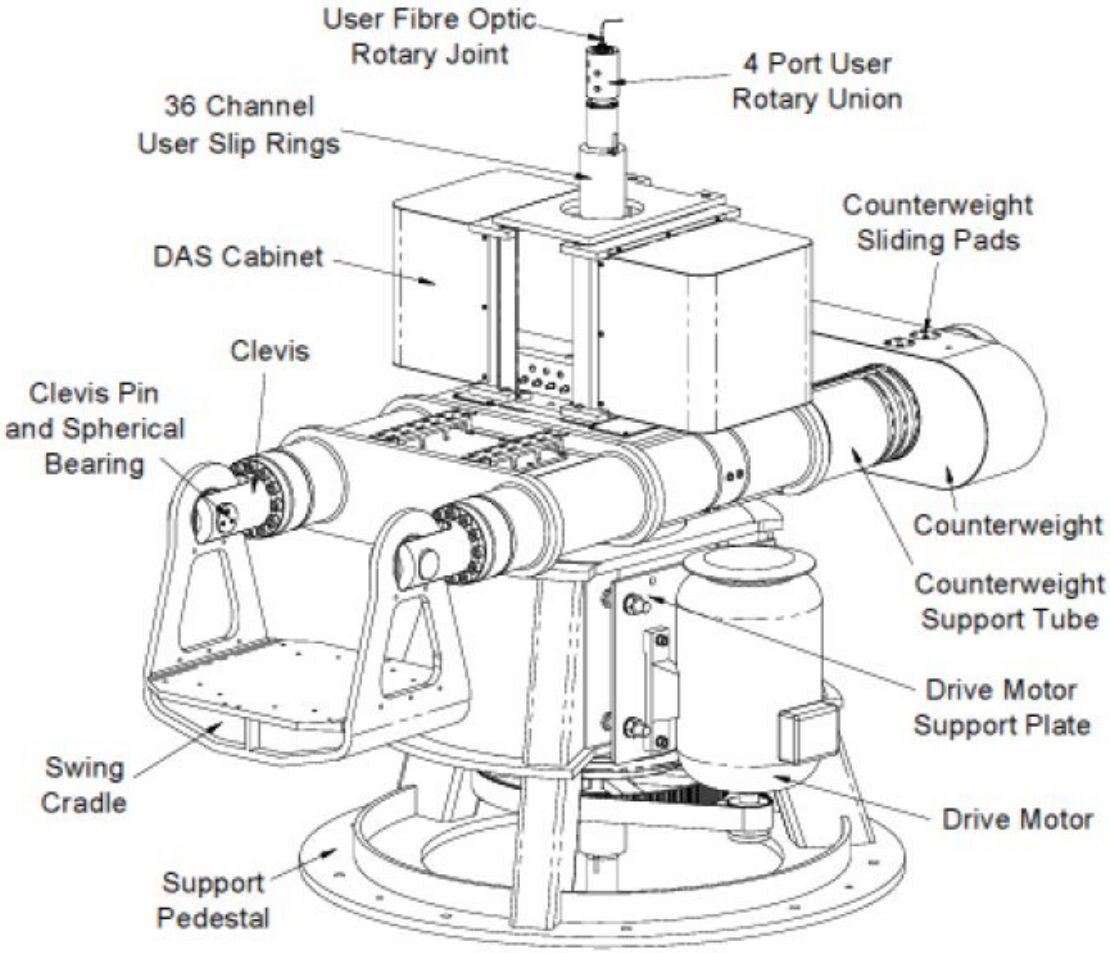


Figure 3.1: Typical sketch of general arrangement of centrifuge, after Ellis et al., 2006

3.2.2 Scaling laws

In order to achieve stress similarity, small scale models are designed carefully according to scaling laws that relate the small scale model to a full-scale prototype. Considering a centrifuge

model located at a radius, r, rotating at an angular velocity, w, the radial acceleration, a, is calculated by equation 3.1, as shown in Figure 3.2; the acceleration is equal to N multiples of gravitational acceleration, g.

$$a = r w^2 = Ng \tag{3.1}$$

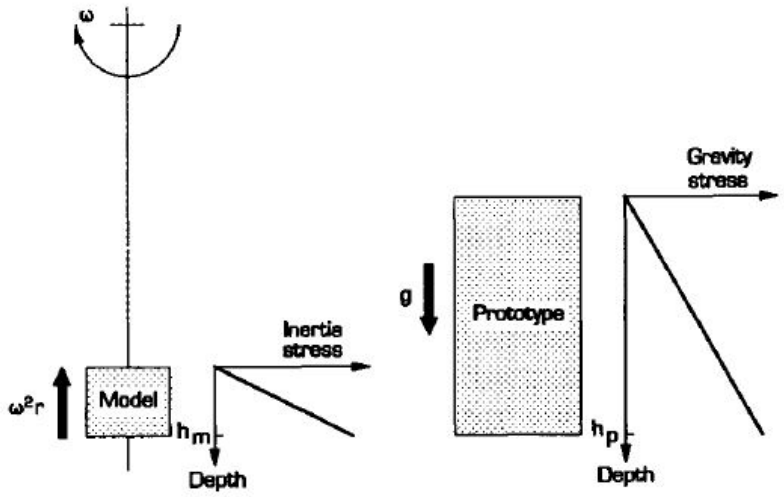


Figure 3.2: Inertial stresses in a centrifuge model and gravitational stresses in the corresponding prototype (Taylor, 1995)

In order to achieve stress similarity between the model and prototype, the following conditions must hold.

$$\sigma_{v,\text{model}} = \sigma_{v,\text{prototype}} \tag{3.2}$$

$$\rho N g z_{\text{model}} = \rho g z_{\text{prototype}} \tag{3.3}$$

where σ_v is vertical stress, ρ is density, z is soil depth, and N is a scaling factor. Considering the same soil density for both the model and the prototype, a scale factor for a linear dimension is 1: N, as seen in Equation 3.4.

$$z_{\text{model}} = \frac{1}{N} z_{\text{prototype}} \tag{3.4}$$

If a model is constructed at 1:N scale and the soil density is the same as in the prototype, stress similarity will be achieved between the two. Scale factors relating the model measurements to prototype values have been proposed and verified by a number of researchers, as summarised in Table 3.1.

Table 3.1: Centrifuge scaling laws (Taylor, 1995)

Parameter	Units	Dimensions	Model:Prototype
Gravity	g	LT^{-2}	$N:1$
Mass	kg	M	$1:N^3$
Force	N	MLT^{-2}	$1:N^2$
Stress	Nm^{-2}	$ML^{-1}T^{-2}$	1:1
Strain	-	-	1:1
Acceleration	ms^{-2}	LT^{-2}	$N:1$
Dynamic velocity	ms^{-1}	LT^{-1}	1:1
Displacement	m	L	$1:N$
Rotation	degree	-	1:1
Time (dynamic process)	s	T	$1:N$

According to Klinkvort et al. (2012), it is feasible to interpret tests in dry sand conditions as if they were carried out in saturated conditions. To achieve this, the effective vertical stress variation in a dry model and the saturated prototype must be identical. Adopting N_s as the geometric scaling factor between prototype and model, and N_g as the acceleration-based scaling factor, this leads to,

$$\sigma'_{v,\text{prototype}} = \rho'_{\text{sat}} \times g \times z_{\text{prototype}} = \sigma'_{v,\text{model}} = \rho_{\text{dry}} \times (N_g \times g) \times z_{\text{model}} \tag{3.5}$$

$$N_g = \frac{\rho'_{\text{sat}}}{\rho_{\text{dry}}} \times \frac{z_{\text{prototype}}}{z_{\text{model}}} = \frac{\rho'_{\text{sat}}}{\rho_{\text{dry}}} \times N_s \tag{3.6}$$

where ρ'_{sat} is buoyant density ($\rho'_{\text{sat}} = \rho_{\text{sat}} - \rho_{\text{water}}$). It can be seen that by increasing the gravity by N_g, identical soil stress can be achieved in a dry soil model compared to a saturated full-scale prototype which is N_s times larger than the model.

In this study, the HST95 Congleton sand was used, and the dry and saturated density are 1728.7 kgm^{-3} and 2071.4 kgm^{-3}, respectively(Lauder, 2010). Adopting the values of soil density ρ along with a geometric scaling factor $N_s = 100$, a value of $N_g = 62$ is obtained:

$$N_g = \frac{\rho'_{\text{sat}}}{\rho_{\text{dry}}} * N_{\text{s}} = \frac{1071.4\,\text{kgm}^{-3}}{1728.7\,\text{kgm}^{-3}} * 100 = 62 \tag{3.7}$$

The increase in gravity N_g and the geometrical scaling factor $N_{\text{s}} = \frac{z_{\text{prototype}}}{z_{\text{model}}}$ are not identical. In this research, the tests were performed at 62 g in dry sand to simulate 100 g in saturated sand.

Consequently, to obtain scaling factors for force and stress in this case, we consider a dry soil cube with dimensions a, b and c and a saturated soil cube with the same dimensions, along with a density for these cubes of ρ_{dry} and ρ_{sat} respectively. The force measured in the centrifuge model spun at an acceleration of N_g would be:

$$F_{\text{model}} = \rho_{\text{dry}} \times abc \times N_g \times g \tag{3.8}$$

The force in the full-scale prototype N_s times larger than the model is obtained as

$$F_{\text{prototype}} = \rho_{\text{sat}} \times abc \times N_s^3 \times g \tag{3.9}$$

Hence, the relationship between force measured in the centrifuge and the equivalent full-scale prototype force is

$$Factor_{\text{force}} = \frac{F_{\text{prototype}}}{F_{\text{model}}} = \frac{\rho_{\text{sat}}}{\rho_{\text{dry}}} \times \frac{N_s^3}{N_g} \tag{3.10}$$

Adopting the values of ρ for this study, this gives a force scaling factor of

$$Factor_{\text{force}} = \frac{2071.4}{1728.7} \times \frac{100^3}{62} = 19326 \tag{3.11}$$

3.2.3 Scaling errors

3.2.3.1 Scaling of soils

It is not feasible to scale sands down according to the geometric scaling factor; reducing the particle size of the sands in the centrifuge model by a scaling factor of N_g would change its continuum behaviour such that it would not represent the equivalent prototype in sands. In terms of centrifuge modelling of laterally loaded piles, the continuum behaviour is ensured provided the ratio between the pile diameter and the average grain size is larger than 60 (the ratio is 353 in this study)(Remaud, 1999).

3.2.3.2 Variation of the acceleration field

The acceleration field in a small scale centrifuge model varies across the depth of the model according to the distance from the centre of rotation of the centrifuge; as a result the nominal scaling factor adopted for the centrifuge test does not necessarily apply everywhere within the model. The centrifuge model is subjected to both radial acceleration and gravitational acceleration. The radial acceleration is equal to $w^2 r$ where w is angular velocity and r is the radius from the central axis of rotation of the centrifuge. This leads to a slightly different vertical stress dis-

tribution compared to that in the prototype, as shown in Figure 3.3. Schofield (1980) suggests the problem can be mitigated by choosing an effective centrifuge radius R_e to determine the scale factor N. This will achieve exact correspondence in stress between model and prototype at two-thirds model depth. The effective centrifuge radius is given by Equation 3.12. This radius was adopted in this study for all centrifuge tests to achieve stress correspondence at two-thirds model depth. After applying this rule, the maximum under-stress error (r_u) and over-stress error (r_o) can be calculated by Equation 3.13. The non-linear stress distribution results in relatively small errors for larger centrifuge models (Taylor, 1995), which applies to this study (the error is 3% in this study).

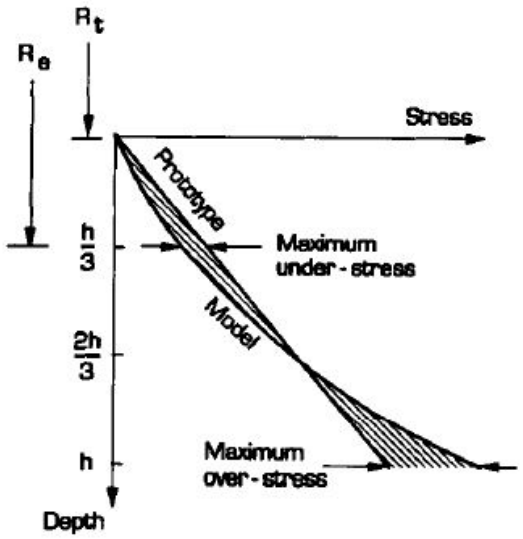


Figure 3.3: Stress variation with depth in a centrifuge model and the prototype (Taylor, 1995)

$$R_e = R_t + \frac{h}{3} \tag{3.12}$$

$$r_u = r_o = \frac{h}{6R_e} \tag{3.13}$$

3.3 Model preparation

3.3.1 Sand preparation

Sands used for this research were Congleton silica sands (HST95) from Bent Farm in Congleton, Cheshire. The properties of HST95 are summarised in Table 3.2.

Table 3.2: Properties of HST95 Congleton sand (Lauder, 2010)

Property	Symbol	Unit	Value
Average grain size	d_{50}	mm	0.17
Specific gravity	G_s	–	2.63
Coefficient of uniformity	C_u	–	1.9
Minimum dry unit weight	$\gamma_{\text{dry,min}}$	kNm^{-3}	14.59
Maximum dry unit weight	$\gamma_{\text{dry,max}}$	kNm^{-3}	17.58
Minimum void ratio	e_{min}	–	0.467
Maximum void ratio	e_{max}	–	0.796
Critical angle (direct shear)	ϕ'_{crit}	degree	32
Critical angle (triaxial shear)	ϕ'_{crit}	degree	32
Peak angle (direct shear)	ϕ'_{peak}	degree	-
Peak angle (triaxial test)	ϕ'_{peak}	degree	39

All centrifuge models were prepared using the air pluviation method to ensure consistency between tests. For dry sand, air pluviation can be used to achieve a specific relative density through the control of fall height and flow rate (Vaid and Negussey, 1984). For the tests presented in this thesis, samples were prepared to a relative density of 90% by pouring sand at a height of 1 m using a nozzle with five 3 mm diameter holes.

3.3.2 The pile

The dimensions of the model pile and corresponding prototype scale dimensions (using N_g = 100 as the geometric scaling factor) are shown in Table 3.3. The ratio D/d_{50} is larger than 60, hence the soil continuity is ensured. A 2kg aluminium pile cap (equivalent to 49.8kN in the

centrifuge) is plugged and fixed on the top of the pile. The separation of the pile to the edge of the container should be 8D to avoid boundary effects for laterally loaded piles (Reddy and Ayothiraman, 2015). However, the distance in this study is 4D. The effect has been investigated via the finite element method and it was suggested that the effect is negligible (Elvis, 2018). In addition, the pile head displacement is less than 6mm so the boundary effect is avoided in this study. The pile is closed-ended with a cap attached to its bottom. Additionally, the surface of the pile and its base are coated with sand to enhance coupling with the surrounding soil. This approach is logical, as the pile foundation is driven into the soil, ensuring that the pile-soil interface is rougher compared to the interaction between bare metal and soil.

Table 3.3: Properties of the model pile and corresponding prototype monopile

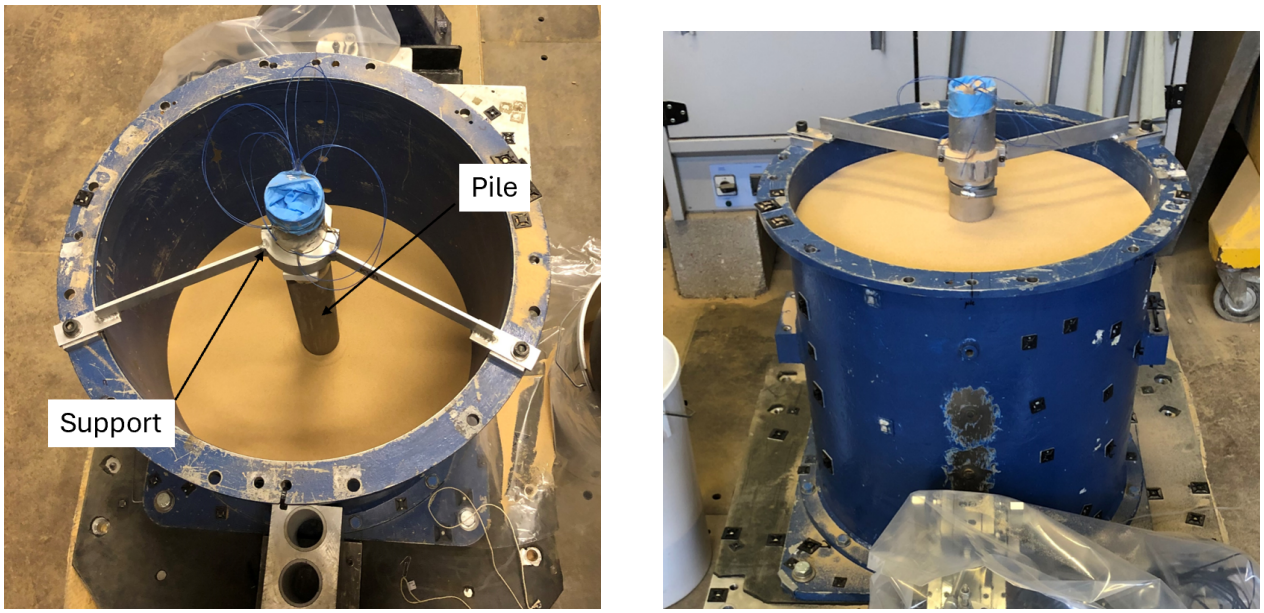
Property	Symbol	Unit	Model pile	Prototype
Diameter of pile	D	m	0.06	6
Total length	L	m	0.5	50
Embedded Depth	L_{em}	m	0.3	30
Wall thickness	t_p	m	0.003	0.18
Young's Modulus	E_p	GPa	70	210
Second moment area	I_p	m^4	2.188×10^{-7}	13.9481
Flexural stiffness	$E_p I_p$	MNm^2	0.0153	2.959×10^6
Cross Section Area	A_p	m^2	0.537×10^{-3}	3.291

3.3.3 Pile installation

In terms of pile installation methods for centrifuge tests, the pile can be installed at 1-g or at elevated g level. Klinkvort et al. (2012) performed centrifuge tests of five solid steel piles with different diameters which were installed at both 1-g and elevated g to investigate the installation effect. The procedure for in-flight installation was to prepare the sand and mount the package at 1-g and then spin the centrifuge up to install the pile at elevated g. After that, the centrifuge

was stopped and the package was replaced with lateral loading equipment. Results show that the initial stiffness and bearing capacity of pile force-displacement are greater for piles installed in-flight than those installed at 1-g. Kirkwood (2015) carried out centrifuge tests of open ended aluminium hollow piles which were driven into the sand at 1-g. Klinkvort and Hededal (2012) conducted centrifuge tests of two solid steel piles with different diameters. In the tests, the small diameter pile was installed at 1-g and the large diameter pile was installed at elevated g. The method of pile in-flight installation was the same as that used in Klinkvort et al. (2012). An issue associated with the adopted in-flight installation is the uncertainty of the effects caused by soil stress decreasing and increasing during spinning down (after installation) and then spinning back up (after installing the lateral loading equipment). Craig (1985) pointed out that the lateral capacity of a pile, in comparison with the prototype, would be reduced if the pile was driven into soil at 1-g.

The ideal situation would clearly be to install the pile at elevated g and then, without spinning down, apply lateral loading. Unfortunately, the technical challenges associated with this approach were not able to be overcome within this study. As a result, in this study, the pile was installed at 1-g. To minimise the effect of pile driving, was not driven into the sand at 1-g but rather sand was poured around the pile. To achieve this, the pile was placed in the container and secured by temporary supports during the sand pouring (after pouring sand to the level of the base of the pile)(see Figure 3.4). The supports were made of small-thickness aluminium sheet to reduce disturbance to the sand pouring. The supports were removed after completion of sand pouring. A closed-ended hollow pile was adopted to simulate plugged driven monopile foundations.



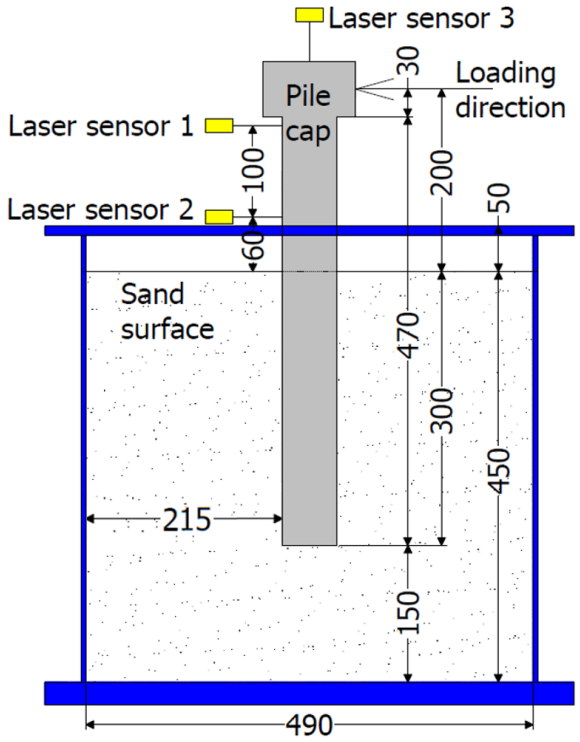
(a) Pile placed in the container

(b) Sand pouring completed

Figure 3.4: sand preparation and pile installation

3.4 Monotonic test kit

Monotonic lateral loading tests of the instrumented pile were carried out to obtain backbone curves for subsequent use in the analysis of cyclic lateral loading tests. A schematic drawing is presented in Figure 3.5a. The loading device used for monotonic tests is shown in Figure 3.5. The device was used to apply horizontal forces under displacement control conditions. A stepper motor and gear box drives a nut on a ball-screw toward the pile at a rate of 0.1 mm/s, with force applied to the pile cap measured with a load cell (5 kN capacity, 200 Series In-Line, Richmond Industries). The direction of force is kept horizontal regardless of the tilting of the pile due to the use of spherical connector attached to the loading side of the load cell. Two laser sensors (OADM 20I6460/S14F, Baumer) were used to measure the lateral displacement of the pile in order to calculate the rotation of the pile. A third laser sensor was located above the pile to measure the vertical displacement of the pile.



(a) Schematic drawing for both pushover tests and cyclic tests

m/mono1.PNG

(b) Front view

m/mono2.jpg

(c) Top view

Figure 3.5: Monotonic test setup

3.5 Cyclic test kit

3.5.1 Introduction

A new load control apparatus capable of applying both one-way and two-way cyclic lateral loads to a model pile was developed to investigate foundation response under a large number of load cycles. Figure 3.6 shows the cyclic test kit and Figure 3.7 shows a representation of the kit. A pile and sand are contained in a steel container. A cap is rigidly attached to the top of the pile and connected by steel cables and pulleys to a dead weight on one side of the pile and the loading system on the other side. The loading system is comprised of a mass block sitting on a pin-supported plate equipped with a carriage system and an AKM motor in conjunction with a 21.5:1 gearbox. The movement of the mass block is controlled by the rotation of the AKM motor through a circular disc and connection rod. The AKM motor and gearbox are secured on a gantry and a conveyance system which is controlled by a separate stepper motor and gearbox system.

3.5.2 Loading principle

The principle of the kit is to generate a load-control cyclic loading on the pile through the periodical movement of a sliding mass (M_2) (Figure 3.8) through the turning of the circular disc in Figure 3.7 via the AKM motor. The range of movement of M_2 is determined by the location of the connection point of the rod joining M_2 to the circular disc . The force applied on the pile is the load difference (ΔF) between the loads from the sliding mass side (F_2, measured by load cell 2) and the counterweight side (mass M_1, with F_1 measured by load cell1). F_2 also includes the weight of the plate, carriage rails and the hanger; the total mass (M_{total}) of these components

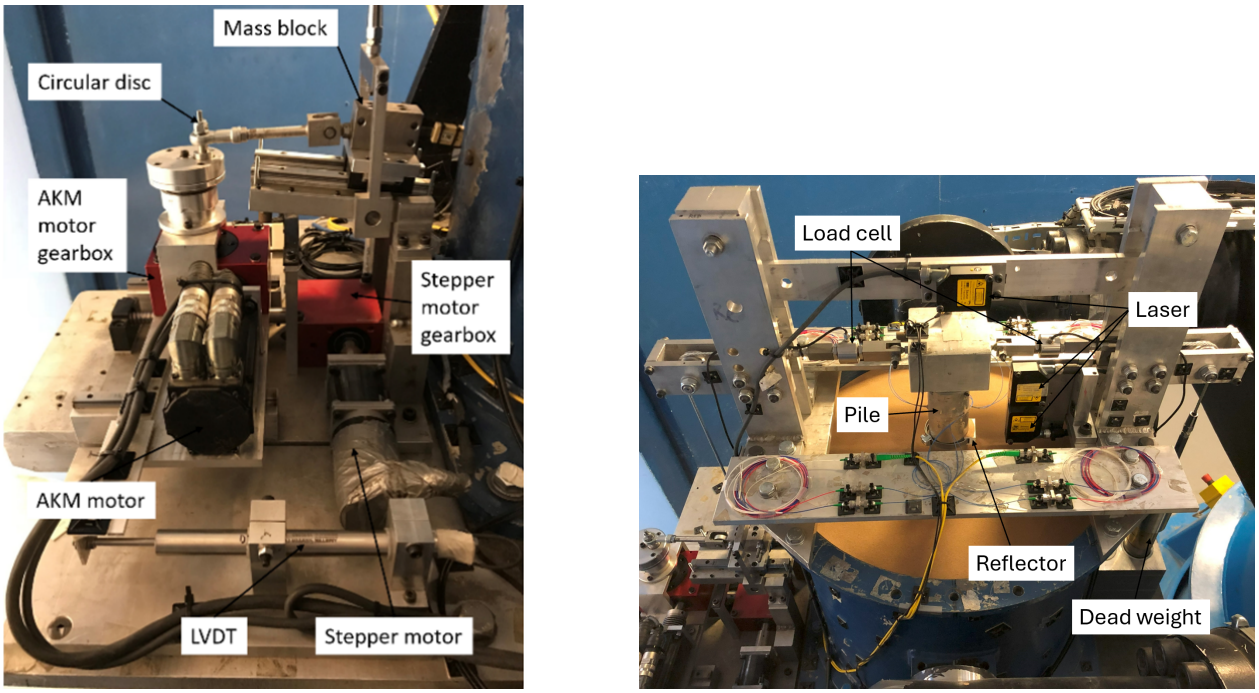


Figure 3.6: Cyclic test kit

(excluding M_2) is 1.33 kg. The length of the plate is d_{plate}, which is 160 mm. In Figure 3.8, d_1 is constant (40 mm) and d_2, the distance from the centre of the sliding mass M_2 to the cable (positive direction is away from the pin support), varies. The total range of d_2 in this study was 40 mm (i.e. the connection point on the circular disc was 20 mm from the centre of rotation of the AKM motor axis).

In Figure 3.7, the AKM motor and circular disc are mounted on a gantry that can be moved towards or away from the pile with the use of a stepper motor driven actuator. By adjusting the position of this gantry, the average value of d_2 can be varied (separate to the 40 mm range of d_2 controlled by the spinning the circular disc). The purpose of including this stepper motor driven gantry is to ensure, during centrifuge spin-up, that a balance between F_1 and F_2 is continuously achieved (by automatically adjusting the position of the gantry and the value of d_2), thereby ensuring the soil surrounding the pile is not disturbed by unwanted pile movements caused by

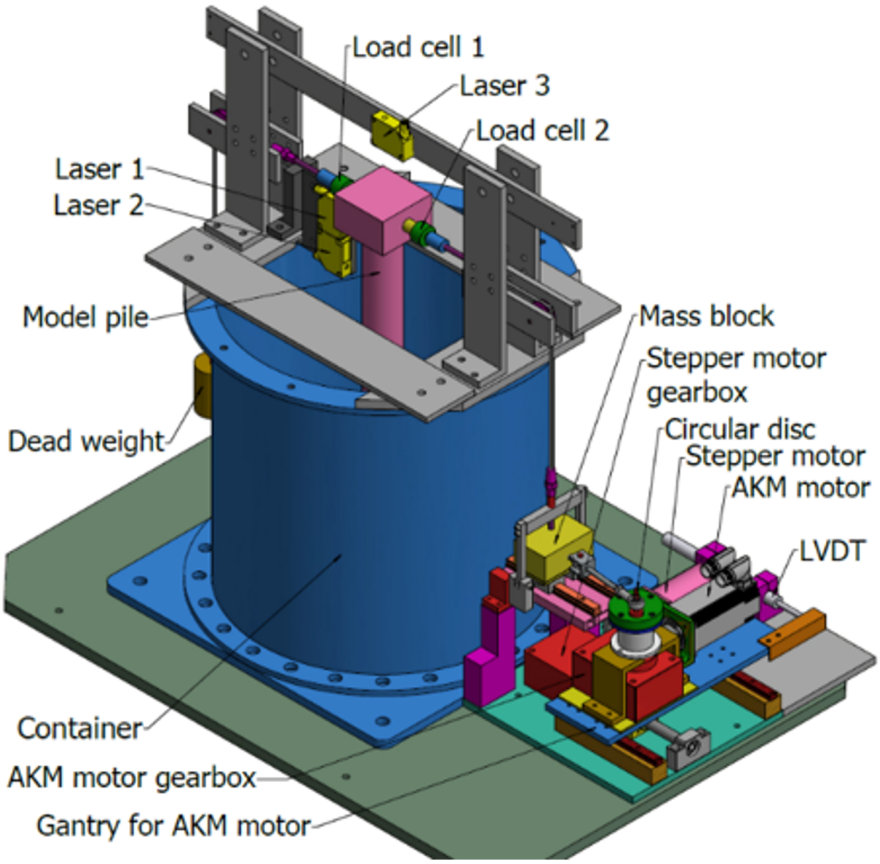


Figure 3.7: The cyclic load control apparatus

a force imbalance during spin-up.

F_1, F_2, and the load difference (ΔF) can be calculated as (where N_g is the acceleration-based scaling factor; this corresponds to the acceleration that the centrifuge was spun to in tests):

$$F_1 = N_g M_1 g \tag{3.14}$$

$$F_2 d_1 = N_g M_2 g (d_1 + d_2) + N_g M_{\text{total}} g \frac{d_{\text{plate}}}{2} \tag{3.15}$$

$$F_2 = N_g M_2 g \left(1 + \frac{d_2}{d_1}\right) + N_g M_{\text{total}} g \frac{d_{\text{plate}}}{2 d_1} \tag{3.16}$$

$$\Delta F = F_2 - F_1 \tag{3.17}$$

The balanced position of mass M_2 (i.e. the value of d_2) can be found by equating F_1 and F_2:

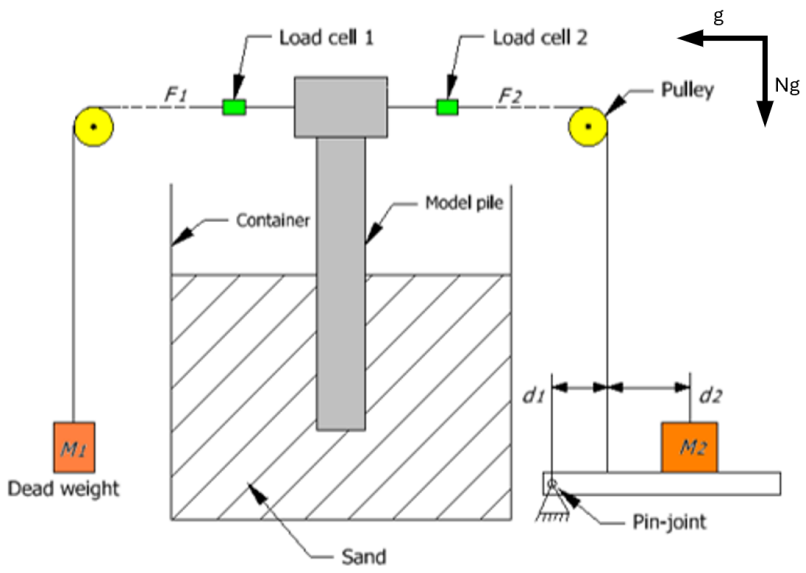


Figure 3.8: Sketch for load calculation

$$F_1 = F_2 \tag{3.18}$$

$$d_{2,\text{balance}} = \left(\frac{M_1}{M_2} - \frac{M_{\text{total}}}{M_2} \frac{d_{\text{plate}}}{2d_1} - 1 \right) d_1 \tag{3.19}$$

Note that, whilst these calculations allow for a pre-test evaluation of the location of the mass M_2, the control program for the stepper-motor (controlling the location of the gantry containing the AKM motor and circular disc) automatically adjusts the gantry location (i.e. d_2) to achieve a balance between F_1 and F_2.

3.5.3 Control program

A 'balance control' Labview program was developed to automatically balance F_2 and F_1 during the centrifuge spin-up stage by operating stepper motor (controlling d_2) while the AKM motor was kept stationary. This 'balance control' program uses a proportional integral derivative (PID)

controller to adjust the position of the AKM motor gantry in order to balance the forces acquired from load cells 1 and 2 on the two sides of the pile.

After reaching the targeted g-level, the 'balance control' program is stopped and a 'cyclic load control' program is initiated. This 'cyclic load control' program operates the AKM motor at a specific speed to apply a certain frequency of loading. The 'cyclic load control' program is also able to control the load ratio of the loading; in other words the specification of maximum and minimum loads applied to the pile. This load ratio control is achieved by adjusting the position of the gantry that houses the AKM motor and circular disc and enables tests including both balanced 2-way loading (equal magnitude maximum forces applied on both sides of the pile), 1-way loading (where the minimum force is zero), and cases with intermediate load biases on each side of the pile. The specifics of test parameters are provided in Table 3.4.

Test	M_1 (kg)	M_2 (kg)	d_2 (mm)
kc01	3.8	1.43	-6
kc02	4	1.53	-3
kc03	4.5	1.99	-2
kc04	4.8	1.43	21
kc05	5.2	1.99	12
kc06	5.2	1.72	20
kc07	5.7	1.99	22
kc08	4.9	1.72	13

Table 3.4: Cyclic test information

3.6 Fibre Bragg Grating

3.6.1 Introduction

Fibre Bragg grating sensors (FBGs) were employed to obtain bending moment profiles along the pile. Eight fibre Bragg cables were installed in the inside surface of the pile at four quadrants. Four fibre Bragg cables have three Braggs and the other four have four Braggs. long opposite sides of the pile, two fibre Bragg cables were installed: one with three and the other with four Braggs. These overlapping fibre Bragg cables lead to seven evenly distributed Braggs along length of the pile at four positions, as shown in the Figure 3.9. Figure 3.10 shows the top view of the pile. Although the four cable positions were not at 90 degrees to each other, it does not affect the results, as explained in the calibration section.

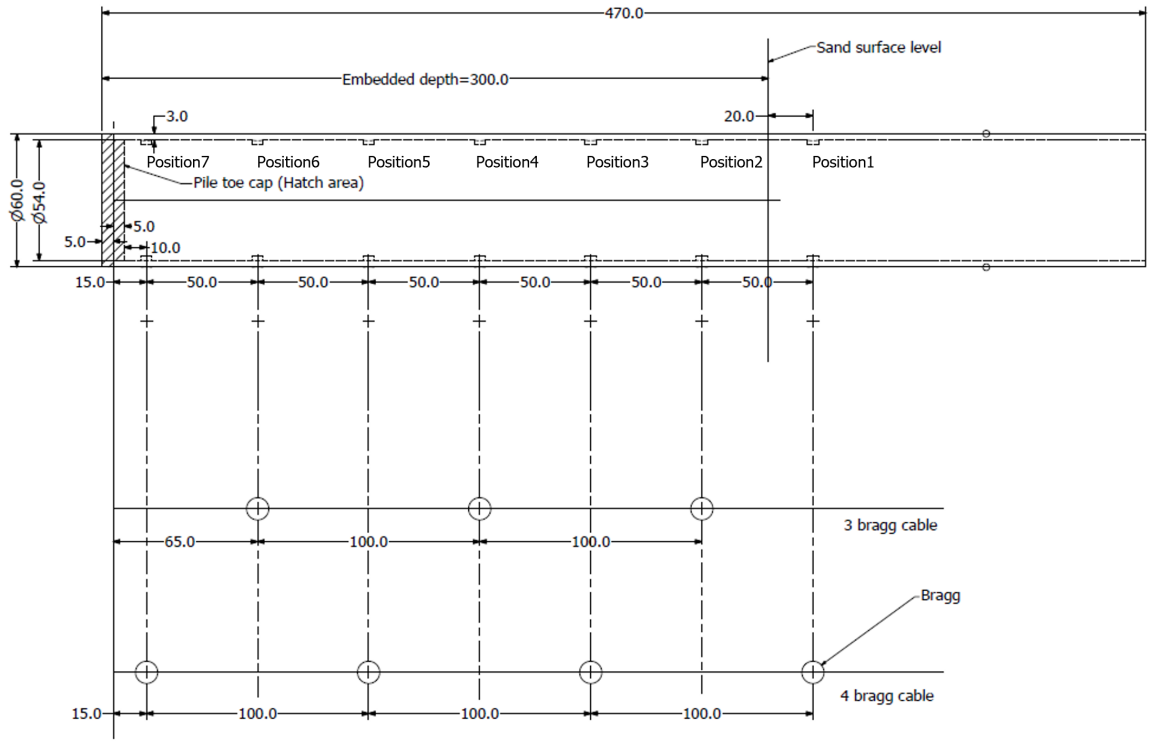
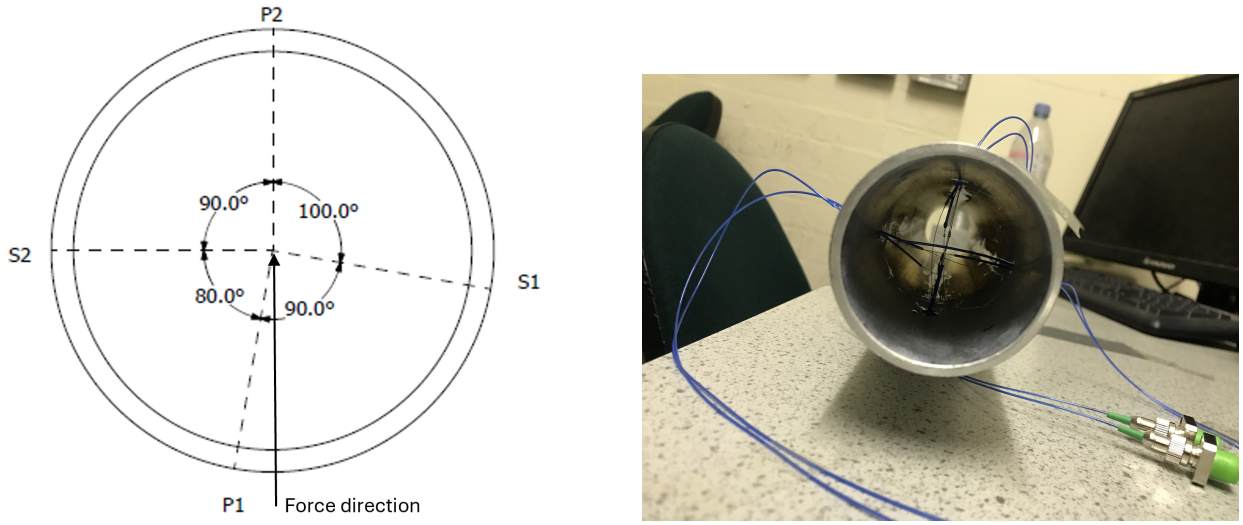


Figure 3.9: Fibre Bragg positions on pile



(a) Sketch for fibre Bragg cable locations

(b) View of fibre Bragg cables installed inside pile

Figure 3.10: Top view for fibre Bragg cables

3.6.2 Installation of FBGs

Fibre Bragg cables were adhered to the surface by applying superglue. First, at one quadrant, a three Braggs cable and a four Braggs cable were cut into correct length and the locations of Braggs were checked. The four Braggs cable was then laid down inside the pile and temporarily fixed at the bottom of the pile using a small drop of superglue. After that, it was lightly stretched along the pile and fixed at the top side. The superglue was then applied over the entire length of the fibre Braggs cable to secure it. After installing the four Braggs cable, three Braggs cable was installed in the same way. Both cables were positioned carefully to ensure seven Braggs were in the right locations. The processes were repeated for the other three quadrants.

3.6.3 Calibration of FBGs

The calibration of the FBGs included two parts: strain calibration and bending calibration. The strain calibration was done to obtain calibration factors that relate fibre reading changes with

strains. After confirming the relation between fibre reading changes with strains, the factors relating fibre reading changes with bending moments were calculated.

3.6.3.1 Strain Calibration of FBGs

Strain calibration was carried out on a load frame in a constant temperature laboratory using the three point bending method. In this calibration, the pile was supported by three flexible straps at the positions shown in Figure 3.11; the straps help reduce stress concentration effects that could occur if rigid loading supports were used. The load is increased from 500 N to 6000 N in steps of 500 N and then back to 500 N. The pile was calibrated at four orientations and the calibration factors then compared. Four orientations correspond to four cases where P1, P2, S1 and S2 (Figure 3.10) are rotated to the top, respectively. At a specific load, the bending moment of the pile at different Bragg positions can be calculated, hence the strains at each Bragg. These strains were then correlated with the change of the fibre readings at different locations to obtain the calibration factors. Equation 3.20 can be used to relate the fibre reading wavelength change $\Delta\lambda$ and the strain ϵ with a linear function with slope (calibration factor) k (temperature effect is neglected as the calibration tests are performed in a constant temperature room). Figure 3.12 shows the correlation between strains and the fibre reading changes for two Braggs for position P1 in the first orientation test. From the figure, a strong linear relationship between strains and the change of the fibre readings are observed for Braggs except at position 7. At position 7, since it is close to the end of the tube, the strain is too small to be measured. The calibration factor k of each Bragg in the four orientation tests are shown in Table 3.5 to 3.8; note that the unit nm is nanometre. For the 1st and 3rd orientation, since the S1 and S2 side fibre readings are small, only P1 and P2 side Bragg calibration factors were considered. Similarly, only S1 and S2 Bragg

calibration factors were calculated for 2nd and 4th orientations.

$$\epsilon = k * \Delta\lambda \tag{3.20}$$

Table 3.5: 1st orientation (P1 at the top)

P1 side Braggs	1	2	3	4	5	6	7
Calibration factors (nm^{-1}) (10^{-4})	8.48	8.38	8.87	8.50	8.94	9.56	-1.93
P2 side Braggs	1	2	3	4	5	6	7
Calibration factors (nm^{-1}) (10^{-4})	8.39	8.88	8.54	8.74	8.57	8.89	9.67

Table 3.6: 2nd orientation (S2 at the top)

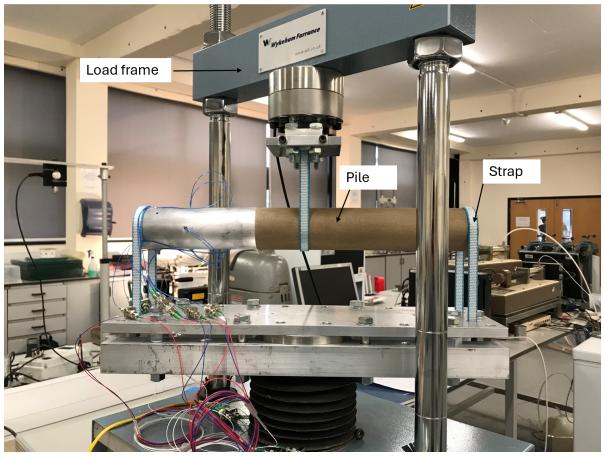
S1 side Braggs	1	2	3	4	5	6	7
Calibration factors (nm^{-1}) (10^{-4})	8.83	8.54	8.76	8.81	8.93	9.18	8.89
S2 side Braggs	1	2	3	4	5	6	7
Calibration factors (nm^{-1}) (10^{-4})	8.11	8.53	8.36	8.22	8.35	8.22	8.73

Table 3.7: 3rd orientation (P2 at the top)

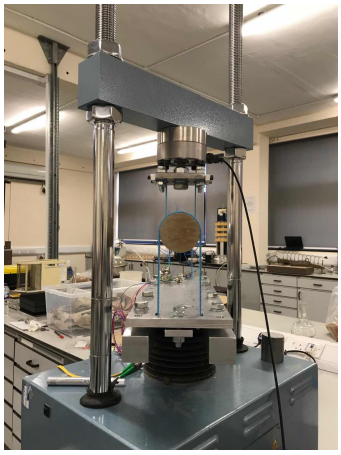
P1 side Braggs	1	2	3	4	5	6	7
Calibration factors (nm^{-1}) (10^{-4})	8.39	8.72	8.71	8.32	8.14	7.71	4.07
P2 side Braggs	1	2	3	4	5	6	7
Calibration factors (nm^{-1}) (10^{-4})	8.42	8.35	8.91	8.69	9.17	9.71	7.86

Table 3.8: 4th orientation (S1 at the top)

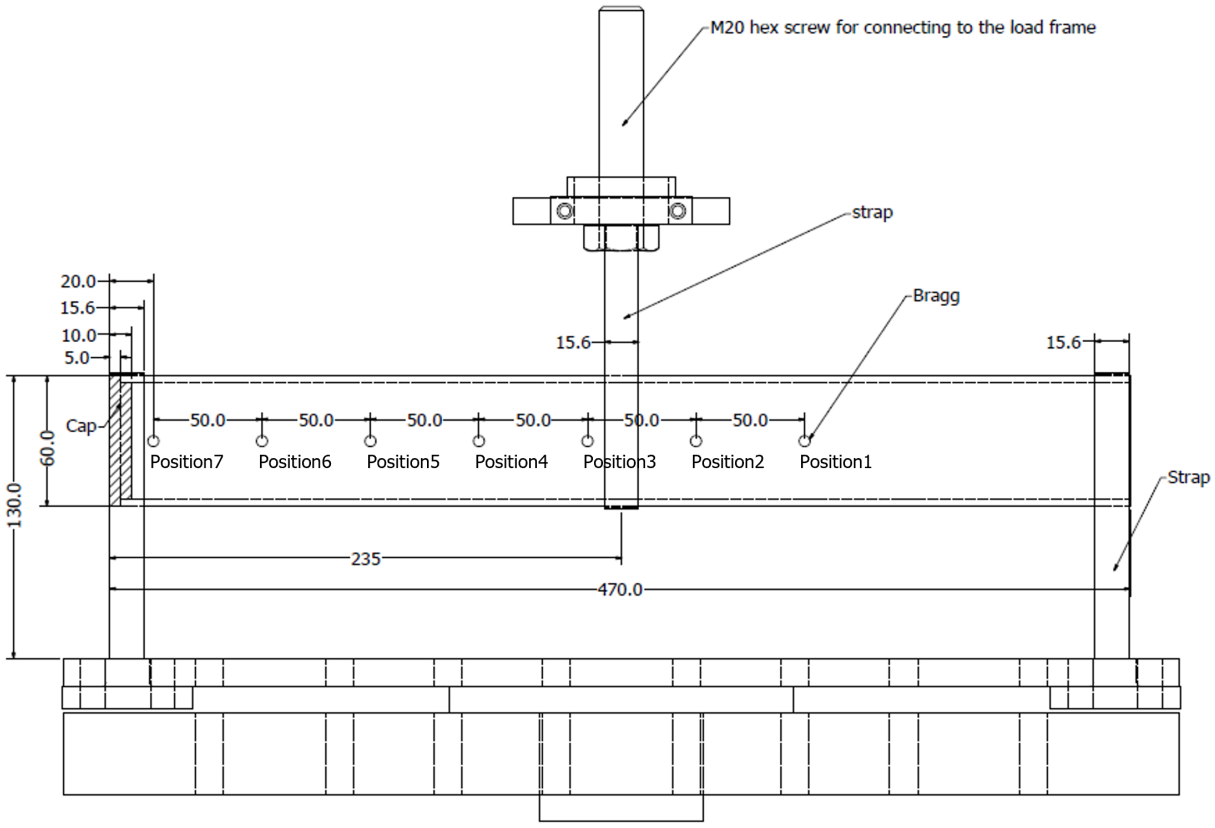
S1 side Braggs	1	2	3	4	5	6	7
Calibration factors (nm^{-1}) (10^{-4})	8.60	8.79	8.88	8.64	8.41	8.41	6.22
S2 side Braggs	1	2	3	4	5	6	7
Calibration factors (nm^{-1}) (10^{-4})	8.33	8.13	8.56	8.30	8.80	8.77	-4.51



(a) Front view



(b) Side view



(c) Sketch of the calibration

Figure 3.11: Bending calibration setup

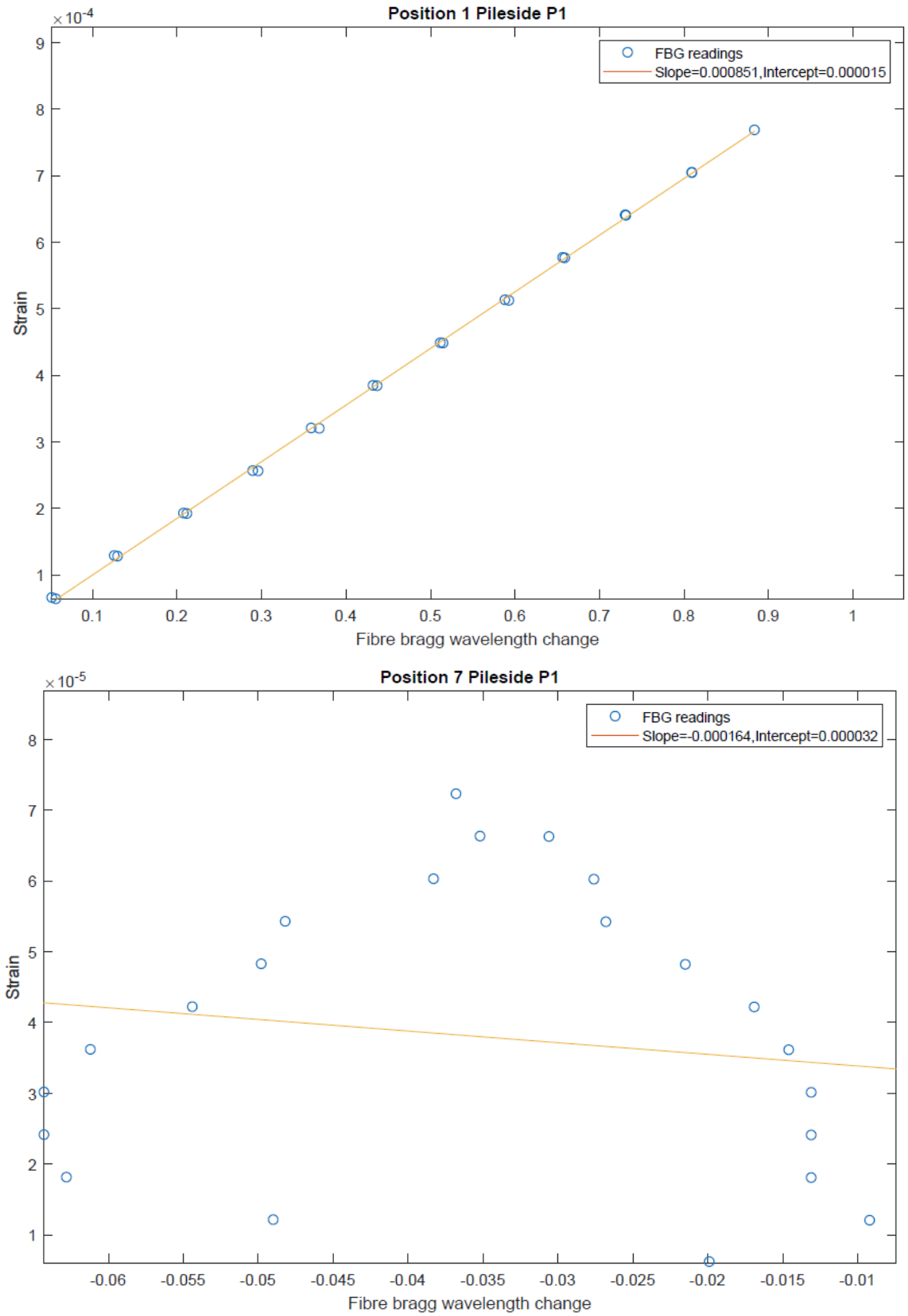


Figure 3.12: Correlation between strains and fibre Bragg wavelength change

Position	1	2	3	4	5	6	7
Calibration factor (Nm/nm)	237.6	242.9	245.2	242.7	246.9	260.2	-50

Table 3.9: Calibration factors for seven positions

In the centrifuge test, since the operation of the centrifuge leads to temperature changes in the centrifuge room, the fibre readings will be influenced by this temperature change. To address this issue, different calibration factors were applied to relate bending moments and the fibre readings directly. Instead of relating the change of fibre readings with strains, the difference between the change of fibre readings at a pile level was related to the bending moment directly at that level. For example, at a given load, measured by the load cell frame, during the 3-point loading test, the bending moment at Position 1, which is the theoretical bending moment based on the loads, is FM_1. The measured fibre reading changes at Position 1 for the Bragg along P2 and P1 (see Figure 3.10a) are $\Delta\lambda_{P2,1}$ and $\Delta\lambda_{P1,1}$, respectively. The difference between $\Delta\lambda_{P1,1}$ and $\Delta\lambda_{P2,1}$ are correlated to FM_1 by the bending moment factor at the Position 1 level, k_1, as shown in Equation 3.21. There are seven positions, thus seven bending moment factors. In doing so, the temperature effect on the fibre readings is cancelled by the deduction of fibre readings at a pile level.

$$FM_i = k_i * (\Delta\lambda_{P1,i} - \Delta\lambda_{P2,i})(i \in (1,7)) \tag{3.21}$$

Table 3.9 shows the calibration factors at the seven positions relating the bending moment and the changes of fibre readings. It should be noted that these factors are averaged bending moment factors across a range of loads (e.g., at 500N, 1000N, 1500N, etc.). It can be seen that the factors are close for the first 6 positions. However, the factor at Position 7 is clearly an outlier. The reason is that both the strain and bending moment at this position is extremely small since this position is near the pile toe. Therefore, the factor at this level is replaced by the average of

Position	1	2	3	4	5	6	7
Calibration factor (Nm/nm)	237.6	242.9	245.2	242.7	246.9	260.2	245.9

Table 3.10: Bending moment factors

the factors at the first 6 positions, as shown in Table 3.10.

During preparation, the pile will be installed such that the load direction is the same as that during calibration. Therefore, the bending moment calibration factors can be directly applied to obtain the bending moment profile along the pile.

3.7 Measurement and instrumentation

The two load cells (load cell 1 and 2 from Figure 3.8 were 5 kN capacity (200 Series In-Line, Richmond Industries). Laser sensors (OADM 20I6460/S14F, Baumer) were used to measure pile displacements. In the application here, where rotation of the pile occurs, traditional displacement sensors which required a connection or contact between the sensor and the measurement target, could cause a problem since the contact point of the displacement transducer does not move only in one direction; this could cause bending of the sensor armature and, affecting readings and potentially damaging the instrument. The laser sensors can be 'trained' to measure over a specific range to improve measurement accuracy. Two lasers were used one side of the pile at different heights above the soil surface to measure the pile head horizontal displacement and derive pile rotation. Another laser was mounted above the pile to measure the vertical displacement of the pile. The logging frequency of all tests was 250Hz.

3.8 Test procedure and summary of tests

Table 3.11 shows the centrifuge tests carried out in this study. Two monotonic tests were performed to identify backbone curves for subsequent use in the analysis of the cyclic lateral loading tests. A total number of 8 cyclic tests were carried out, among which are four one-way cyclic tests (kc01, kc02, kc03, and kc08) and four two-way cyclic tests. The minimum and maximum force are the load difference defined in Equation 3.17. The negative sign of the minimum force suggests that the pile is pulled towards the dead weight direction and the test is a two-way cyclic test. The one-way cyclic tests were conducted under different cyclic maximum load to investigate the effect of cyclic loading magnitude on the pile displacement development. In terms of two-way cyclic tests, two of the tests were symmetric (kc05 and kc05) whereas the others were not symmetric. All cyclic tests were carried out under 2Hz loading frequency. Comparison of results from these tests will examine the effect that different loading characteristics have on the development of pile displacement/rotation with cyclic loading.

Table 3.11: Centrifuge tests

Tests	Type	Diameter (mm)	G-level	Relative density (I_D)	Minimum force (N)	Maximum force (N)	Number of cycles
km00	Monotonic	60	59	90	-	-	-
km01	Monotonic	60	62	92	-	-	-
kc01	Cyclic	60	62	90	0	530	60000
kc02	Cyclic	60	62	91	0	750	25000
kc03	Cyclic	60	62	91	0	1100	40000
kc04	Cyclic	60	62	92	-350	350	40000
kc05	Cyclic	60	62	90	-350	700	50000
kc06	Cyclic	60	62	91	-180	700	40000
kc07	Cyclic	60	62	90	-525	525	35000
kc08	Cyclic	60	62	90	0	890	26000

Chapter 4

Monotonic Test Results

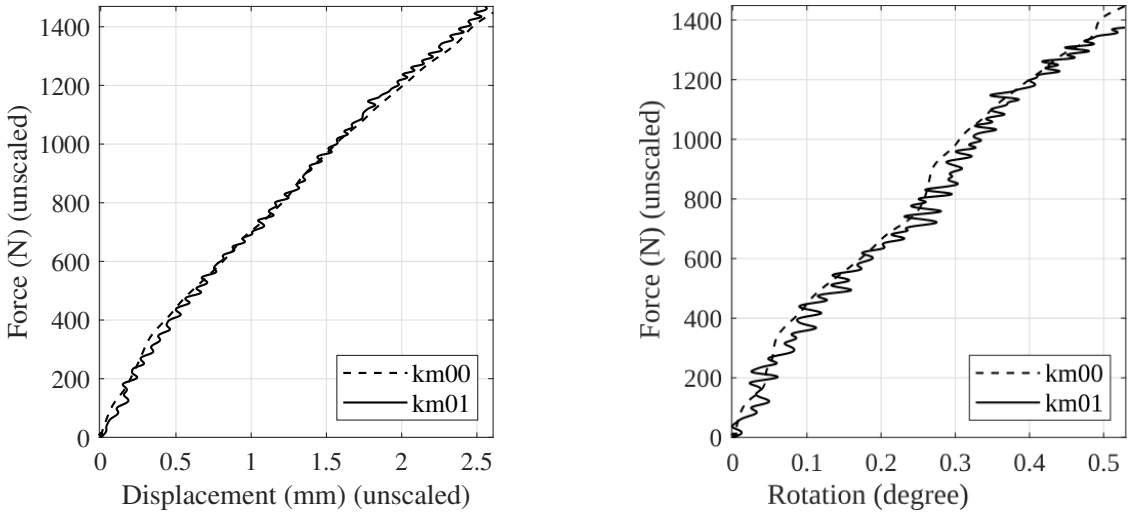
4.1 Introduction

A monotonic lateral loading test of a monopile provides essential information for predictive models related to the cyclic lateral loading of monopiles. Pile lateral displacements plotted against the applied load are generally referred to as a backbone curve. The monotonic backbone curve provides an important reference for comparison with data from cyclic tests. In addition, the bending moments along the pile in monotonic tests can be utilised to derive p-y curves, which is useful when analysing the cyclic p-y curve. It is therefore necessary to carry out monotonic tests with a configuration identical to that of the cyclic tests as a starting point to understand piles under cyclic loads.

Results in this chapter are generally presented in prototype scale (where the scaling factor $N_g = 100$ is used), unless otherwise indicated.

4.2 Backbone curve

Figure 4.1 shows load versus pile head displacement of two monotonic tests, which is the monotonic backbone curve. These two tests show the same pile response under lateral loads, indicating good repeatability of the tests. The data can also be represented as force versus rotation, as shown in Figure 4.1b. In Figure 4.1b, the pile rotation is calculated using the laser displacement sensors, as described in Chapter 3. According to the serviceability limit state, the pile head rotation should not exceed 0.5 degrees (Achmus et al., 2009), therefore, the equivalent force corresponding to 0.5 degrees is selected as a reference force, $H_{ref} = 1400$ N. This value will be used in the cyclic analysis so that the maximum cyclic load applied is less than the reference load and pile head rotation is within the serviceability limit. The backbone curve will be compared with the pile response under cyclic loading.



(a) Force versus displacement

(b) Force versus rotation

Figure 4.1: Monotonic backbone curve

4.3 Bending moment evolution

Figure 4.2 shows the evolution of measured bending moment points by FBGs (Fibre Bragg grating sensors) at an increasing sequence of loads in the monotonic test with one measurement point above the sand surface. Since the bending profile above the sand surface is different from that below the sand surface, as shown in Figure 4.3, the interpolation of bending moments for these two sections was conducted separately. The bending moment profile above the sand surface is linear and thus will be fitted by a linear function. In contrast, the moment profile below the surface is a non-linear function, and it will be interpolated using polynomials to capture the trend of measured moment points.

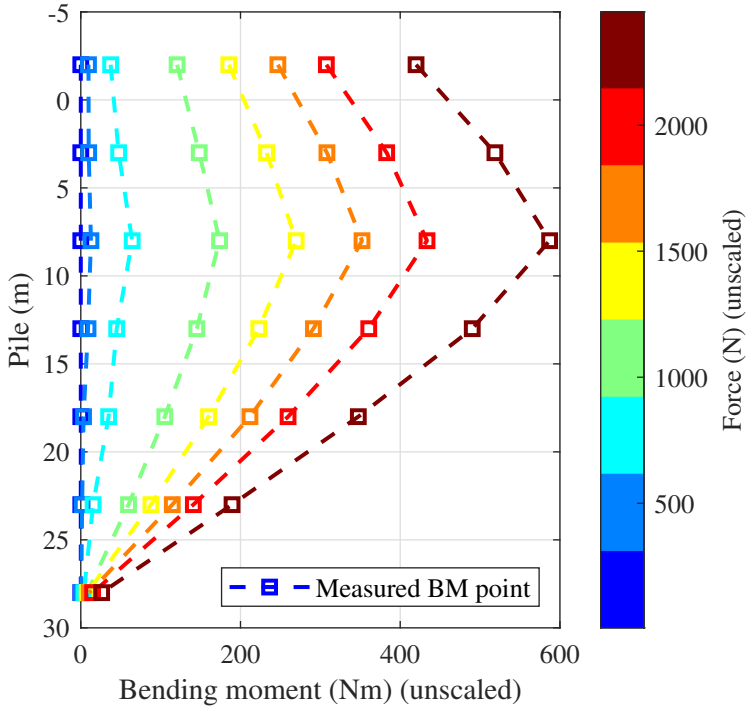


Figure 4.2: Measured bending moments

The bending moment at the sand surface is estimated by a linear fit based on the FBGs above the mudline and zero moments at the pile head. It is then compared with the theoretical mudline moment, i.e., applied force multiplied by load eccentricity. Figure 4.4 shows the fitting line

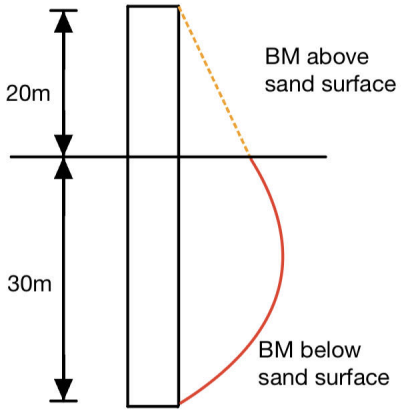


Figure 4.3: Schematic: bending moment along the pile (prototype scale)

of the moment profile above the sand surface based on the zero bending moment at the pile head and a measured bending moment from FBGs. The intersection of the fitting line with the sand surface level (horizontal axis) at every load is the estimated surface moment, which is in agreement with the theoretical moment, indicating that the FBG measurements are reliable. For the clarity of plots, the depth is positive for depth below the sand surface and negative for the depth above sand surface in all figures. In addition, all the bending moments at the sand surface throughout the thesis are estimated bending moments obtained based on the method above.

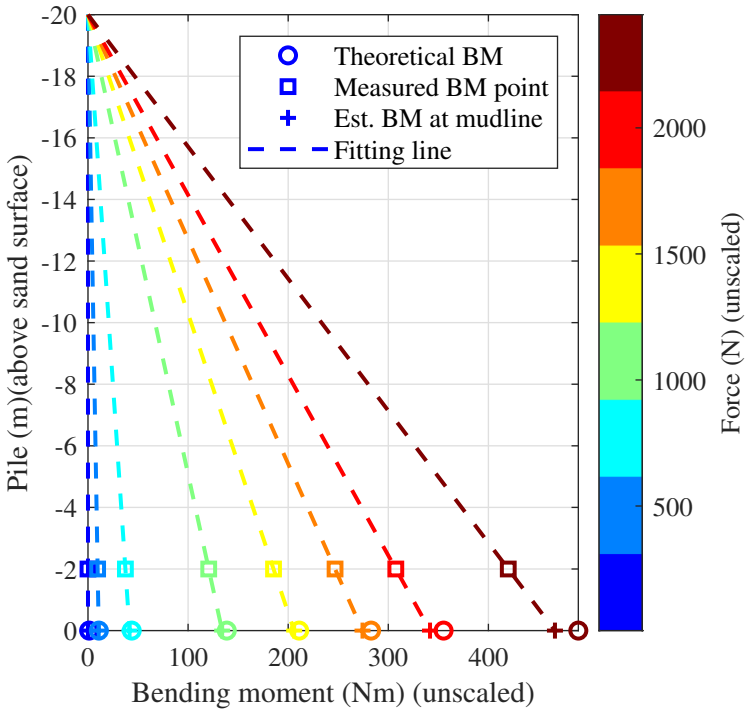


Figure 4.4: Bending moment above sand surface

4.4 Lateral soil reaction and pile deflection

After obtaining the bending moment profile, lateral soil reaction and deflection along the pile can be calculated. For soil reaction, it can be derived by double differentiation of the bending moment profile, see Equation 4.1. It is therefore necessary to fit a continuous function to the discrete measured bending moment points so that the function representing the bending moment profile can be differentiated and integrated to derive soil reaction and displacement along the pile. Several methods have been employed to fit the bending moment profile, including global polynomial function, cubic spline, and piece-wise polynomial (Yang and Liang, 2006). Haiderali and Madabhushi (2016) suggest cubic spline yields the best lateral soil reaction results. However, Kirkwood (2015) points out that cubic splines are also prone to fitting errors and do not produce better results compared to polynomial functions. Hence, a single polynomial function was fitted to all of the data (as opposed to a piece-wise approach). However, it is important to determine the optimum order of polynomial function to adopt, and hence this is investigated here.

$$p = \frac{d^2 M}{dz^2} \tag{4.1}$$

where p is the soil reaction, M is the bending moment function along the pile, and z is the pile depth. Figure 4.5 shows the bending moment BM fitted by 4th, 5th, and 6th order polynomial functions at different loads. The left column of the figure shows the bending moment profile for increasing loads, and the right column of the figure shows the corresponding soil reaction profile derived from the different polynomial curves fitted to the bending moment profile. It can be seen that both 5th and 6th-order polynomial functions provide a reasonable fit for the bend-

ing moment profile. However, the soil reaction obtained by the 5th and 6th-order polynomials shows an oscillatory behaviour. This behaviour was also observed by Kirkwood (2015) whereby the higher order polynomials led to more severe oscillations in the soil reaction profiles. On the other hand, the 4th-order polynomial provides a consistent soil reaction profile across the range of applied head loads (300N, 600N, 900N). It would be expected that the overall shape of the soil reaction profile would not fundamentally change as the head load increases. Therefore, the 4th-order polynomial was selected to fit bending moments in this study. The fitting line for bending moments is shown in Figure 4.6, which provides a good fit for the measured bending moments. The resulting soil reaction obtained by double differentiating the fitting line of bending moments is shown in Figure 4.6. The obtained soil reaction will be used to plot p-y curves for the monotonic test. From this figure it can be seen that across all applied head-loads the 4th-order polynomial does provide a high quality fit to the data.

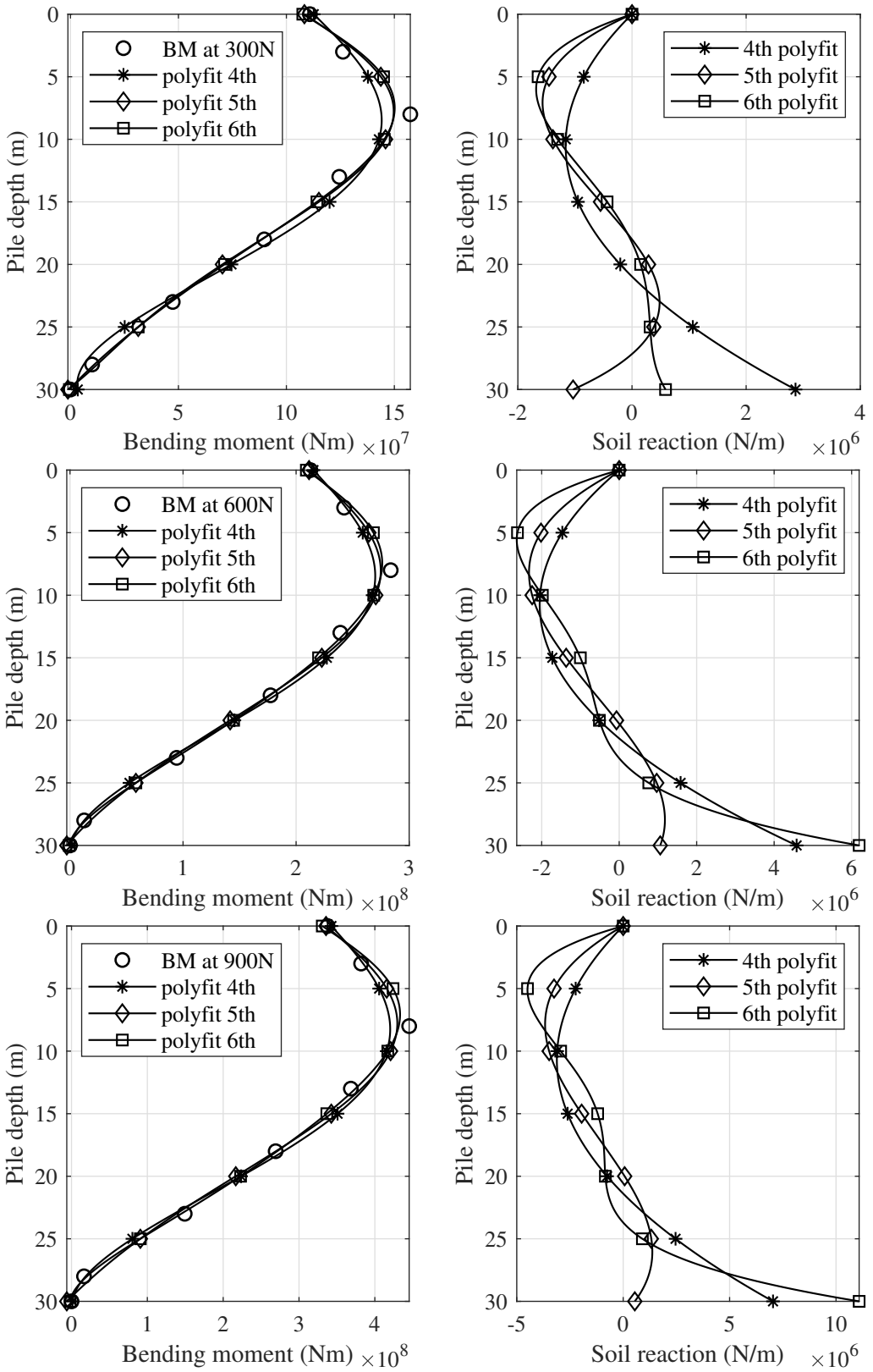


Figure 4.5: Bending moment profile for different head loads with corresponding soil reaction profile derived from polynomial fits

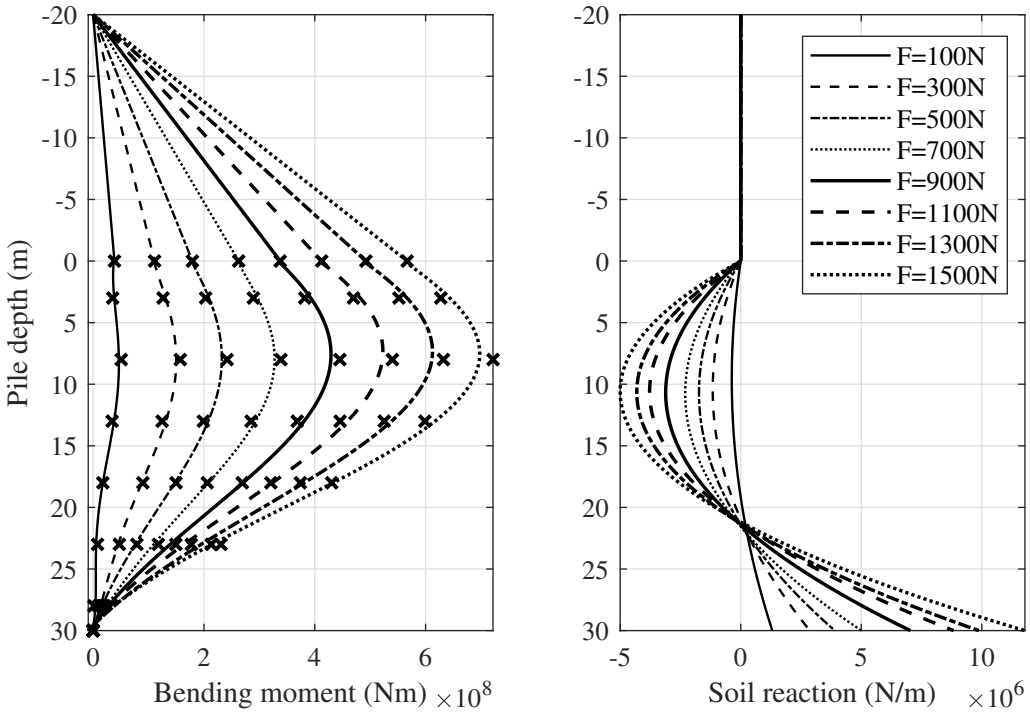


Figure 4.6: Bending moment (a) and soil reaction (b) along the pile

Pile displacement can be calculated by double integration of the bending moment curves using Equation 4.2. Two boundary conditions are required to obtain deflection along the pile. In this study, pile displacements at the two known positions measured by the lasers sensors can be used as the boundary conditions. However, as the fitting lines for bending moments above and below the sand surface are different (see Figure 4.3), it is, therefore, inappropriate to directly apply these conditions to the bending moments below the sand surface. The reason for this is explained later in this section. The logical way to calculate pile deflection above the sand surface is by integrating the bending moment above the sand in combination with laser readings as boundary conditions. The pile deflection and rotation at the sand surface can be obtained, which are then used as boundary conditions for the bending moment below the sand surface. Figure 4.7 (right column) shows pile deflection with depth obtained using this method for three load cases. Similar to the process of deriving soil reactions, three different orders (4th, 5th, & 6th) of polynomial were employed to fit the bending moment profile to subsequently obtain the deflection along the pile. All three polynomials resulted in the same pile deflection. This is because, mathematically, the integration process (as compared to the differentiation process when determining soil reactions) is less sensitive to measurement errors from the FBGs. It is therefore rational to select any of these three fitting methods. In this study, the 4th-order polynomial is selected to fit the bending moments for displacement calculation since it is also used for the derivation of soil reactions. Figure 4.7 shows, in the left column, the measured bending moments and the polynomial fit to the bending moment data along the pile; in the right column, the resulting pile deflection profiles derived from the polynomial curves are shown.

In Figure 4.7, the calculated pile displacement below $\approx$ 15m depth, for the applied head load of 300 N, is not reasonable. Pile displacement is expected to increase monotonically from its

base, with a rotation point (where horizontal displacement is zero) usually assumed to be about two-thirds of the pile depth (Kirkwood, 2015). The displacement profile for the head load of 300 N appears to bend back on itself below a depth of about 15 m, with the toe moving in the same direction as the pile head - this is not a realistic profile given the applied loading regime. There are also reasons to question to obtained displacement profile for the 600 N load. The rotation point, based on the obtained pile deflection curves, is located at a depth of approximately 13 m, i.e. 43% of the pile depth. However, the equivalent rotation point derived from the soil reaction curves indicates it should be located at approximately 70% of the pile depth (21m). The rotation point being located at 70% of the pile depth agrees with results published in literature hence it is believed that the error is with the pile deflections as opposed to the soil reactions (Li et al., 2020; Chortis et al., 2020; Kirkwood, 2015). This error in the fitting of pile displacements is likely due to laser reading errors. These errors may be the result of the package vibration and the inconsistent lighting condition due to the flight of the centrifuge swing cradle. The laser readings acting as boundary conditions have a large effect on the outcome. Measurement errors in the laser readings will result in incorrect pile displacements. To minimise this error, a hybrid method to calculate pile deflection was adopted in this study, which was used in other research (Li et al., 2020; Chortis et al., 2020; Kirkwood, 2015). One boundary condition from the lower laser reading was used, whilst the other boundary condition was taken as the pile rotation, which was assumed as 70% of the pile embedded depth. This assumption is supported by Kirkwood (2015), in which the rotation depth was found to be about 70% of the pile embedded depth. In addition, the rotation point derived from the soil reactions (Figure 4.6) supports this assumption. Figure 4.8 shows the location at which there was zero soil reaction for a range of head loads (extracted from the data presented in Figure 4.6). It shows that the location of

zero lateral soil reaction (also the point of rotation) is at approximately 70% depth. Thus the pile deflection for varying loads can be obtained by double integration of the bending moment data below the sand surface with the two boundary conditions mentioned, with results shown in Figure 4.9. In Figure 4.9, the pile displacement above the lower laser level is calculated by the double integration of the linear bending moment above the sand surface with the two laser readings as boundary conditions. The pile displacement below the lower laser level is based on the same method but using the lower laser reading and the depth of rotation point. From this figure, it can be seen that the gradient of the pile displacement at the lower laser level (pile depth of -6m) is different depending on whether it is calculated from the above surface or below surface data. However, the overall trends of the two sections (above and below the lower laser level) are in agreement and the disparity of the gradient at the laser level is relatively small.

In an ideal situation, all data processing methods would provide the same outcome; unfortunately that was not the case in this study. As a means of progressing, it was felt that the adopted hybrid method was the best available option for obtaining reasonable pile displacements along the pile depth given the issues discussed here.

$$y = \iint \frac{M}{E_p I_p} dz \tag{4.2}$$

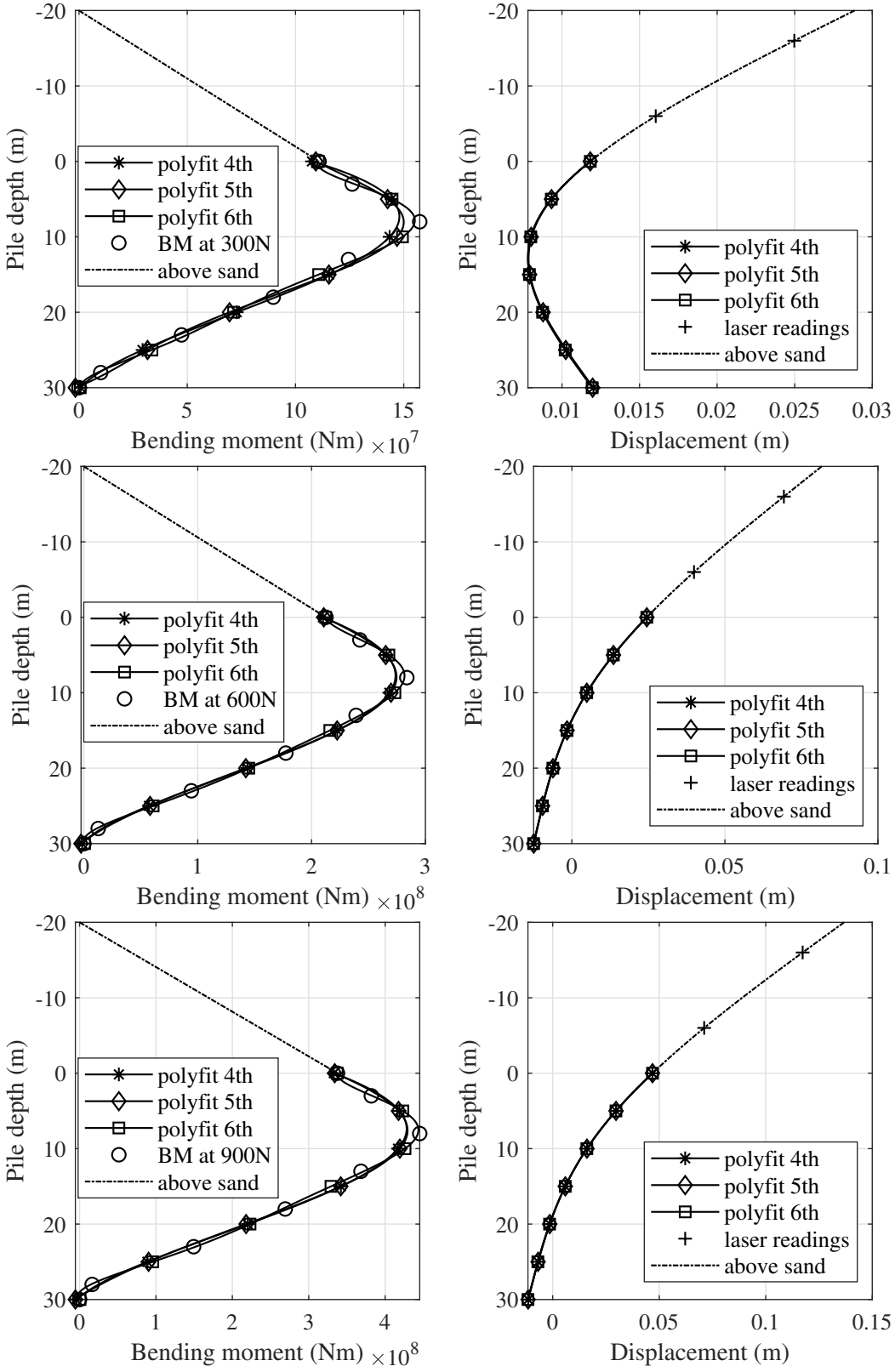


Figure 4.7: Pile displacement profile

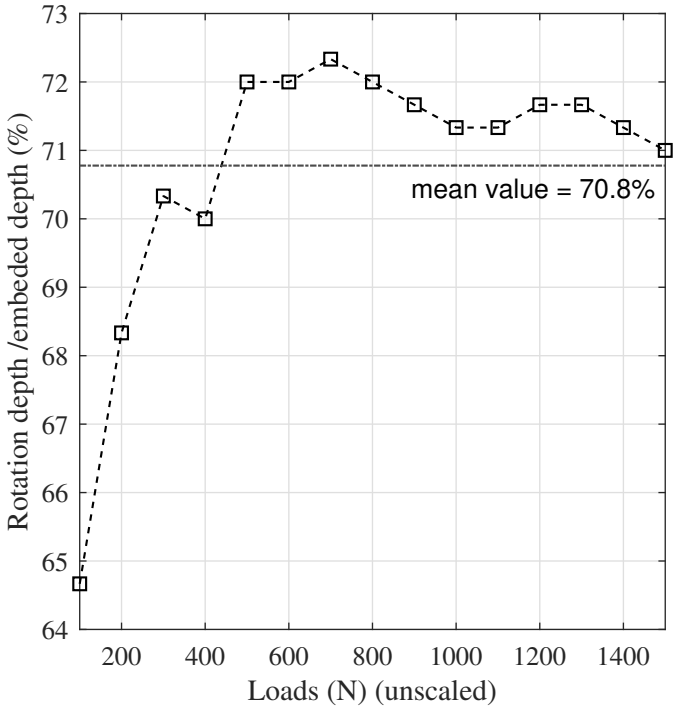


Figure 4.8: Rotation depth ratio for loads

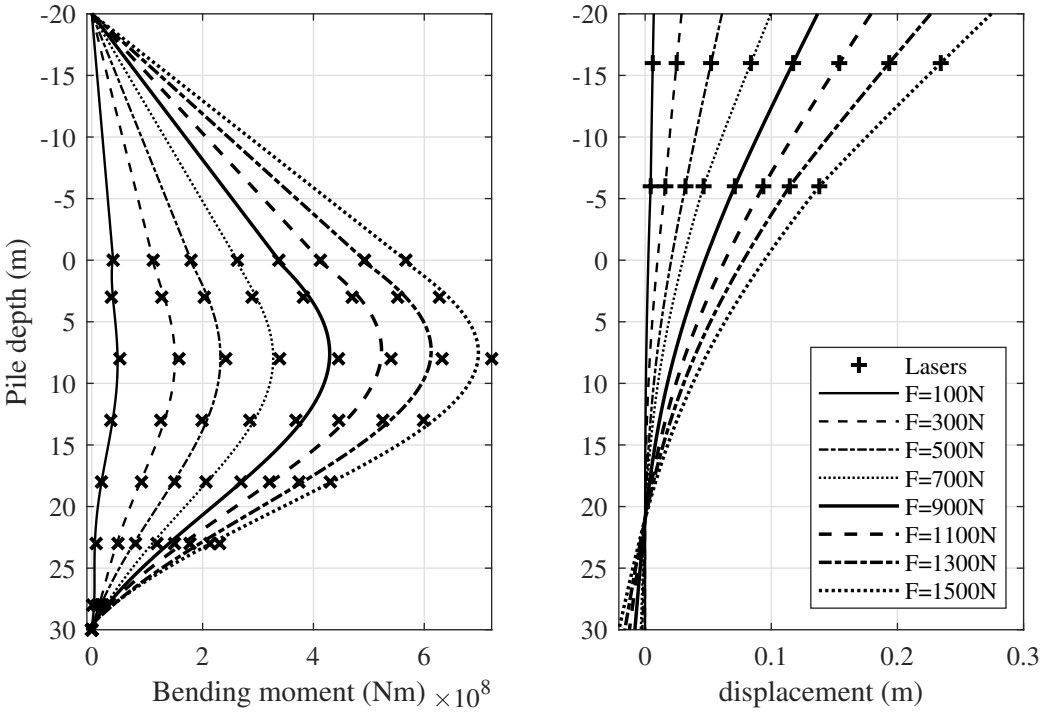


Figure 4.9: Bending moment and pile displacement along the pile

4.5 Derivation of p-y curves

As discussed in detail in Chapter 2, p-y curves are regularly used for the design of monopile foundations. As such, ensuring accurate p-y curves is of paramount importance for safe and efficient design. The soil reaction and displacement data, as presented above, provides an opportunity to obtain high quality p-y curves. The obtained experimental p-y curves will be compared with the curves used in current design standards for monopile foundation design. The p-y curves at different depths were calculated by combining soil reaction and pile displacement at a sequence of loads, see Figure 4.10. Among these lines, depths less than 21m are above the rotation point and those greater than 21m are below the rotation point. The curve for 21m depth, i.e., rotation point, is invisible from the figure, as it has zero displacement and a negligible soil reaction.

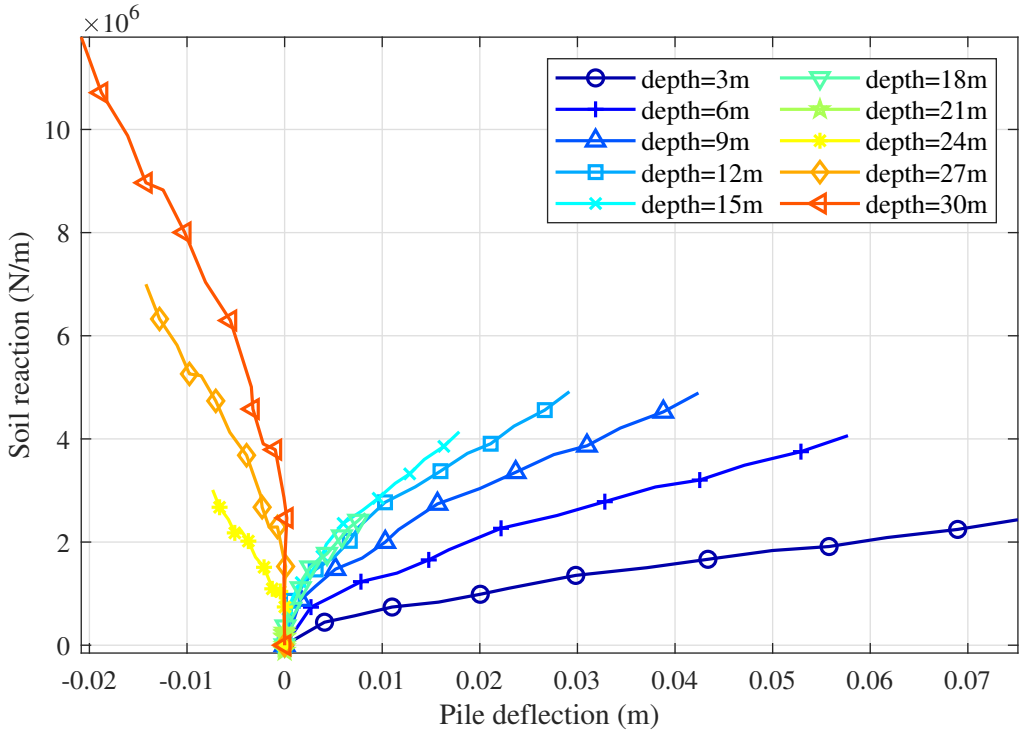


Figure 4.10: p-y curves at different depths

As can be seen from Figure 4.10, soil reaction at a certain depth increases with horizontal pile displacement, and the rate of this increase gradually reduces. This trend applies to curves of all depths. With increasing depths, the initial slope of each curve and the soil reaction at a given pile displacement become greater. However, below the rotation point, the initial slopes of p-y curves are extremely steep. The slopes of these curves are almost vertical with some points passing the $x = 0$ axis, which is physically impossible because the displacement below the rotation point can not have the same direction as the loading direction. This outcome is caused by integration errors during the calculation of pile displacement. At the beginning of each p-y curve, the load is small and the corresponding displacement is also small. Therefore, the integration for calculating pile displacement is sensitive and prone to mathematical error. As a result, the initial slope of p-y curves is discussed with caution.

The experimental p-y curve are compared with the p-y curves recommended by API, which are a commonly used standard for the design of offshore wind turbines, as shown in Figure 4.11 (API, 2011). At shallow depths, for example at 3m and 6m, API p-y curves are in reasonable agreement with the obtained p-y curves. However, the discrepancy between these two sets of p-y curves increases with depth.

The API p-y curves overestimate the soil resistance at greater depths (deeper than 6m). This overestimation of the soil resistance was also observed in other studies (Kirkwood (2015), Chortis et al. (2020), and Sørensen (2012)). There are two notable differences between the API curves and those obtained experimentally across most depths - the initial slope of the API curves is higher, and the ultimate soil reaction is higher. In the API method, the initial slope is given by a constant which is a function of depth, and is also related to the soil's relative density. From Figure 4.11, the initial slope of the API p-y curves are larger than those of the experimental p-

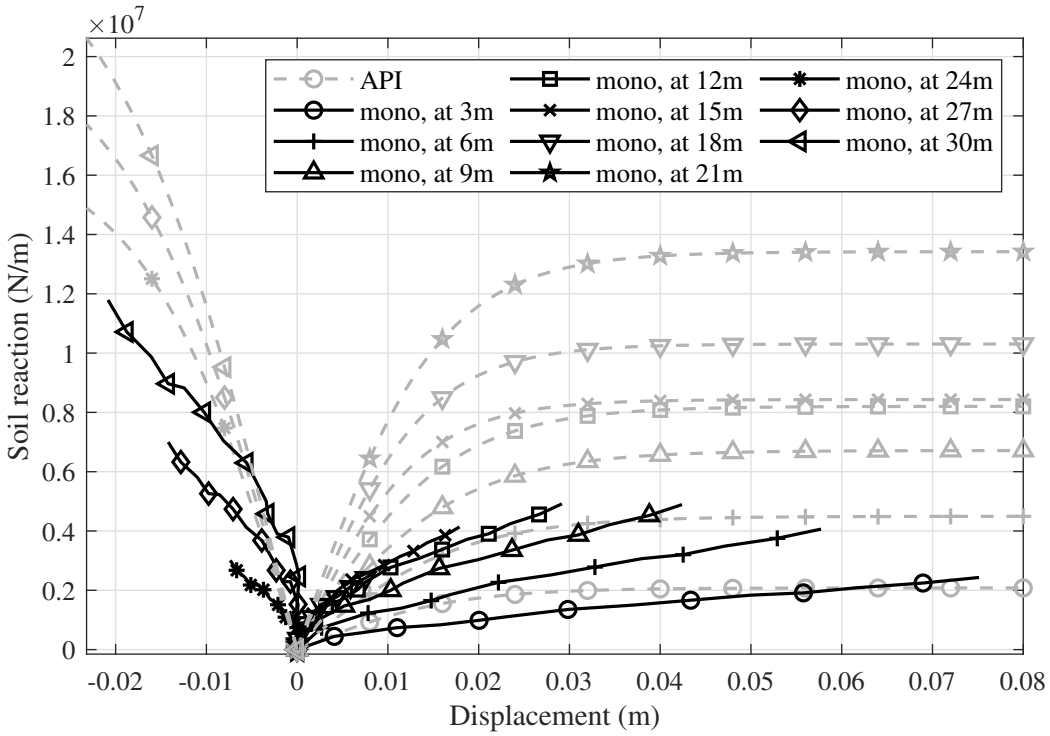


Figure 4.11: P-y curves from API and the experiment

y curves at depths larger than 3m, apart from 27m and 30m whose initial slopes are prone to mathematical errors as discussed in Section 4.4. In terms of ultimate soil resistance, the API p-y curves show similar ultimate soil resistance compared to experimental p-y curves at 3m and 6m depths. For deeper locations, although the experimental p-y curves did not reach the ultimate soil resistance, The API p-y curves overestimate ultimate soil resistance.

The difference between the API method and experimental p-y curves is likely due to the applicability of the API method. API p-y curves were initially developed for oil extraction platforms supported by flexible piles with a relatively small diameter; the API method was later adopted for offshore wind turbine foundations which are usually rigid piles with large diameters. Therefore, the API p-y curves are not suitable for the design of monopile foundations. Previous researchers (Kirkwood (2015), and Sørensen (2012)) have attempted to modify the API method such that it can provide a more accurate prediction of monopile p-y response. However, the modifications

have been based on empirical approaches as opposed to fundamental theory. In addition, their research depends highly on the value of the soil stiffness which is not available in this study. As such, the modified approaches have been fitted to specific datasets and do not provide a generic model for p-y response.

4.6 Summary

In this chapter, the method of obtaining soil reaction, pile displacement, and p-y curves has been explained and experimental p-y curves presented. Comparisons between the experimental p-y curves and the API method were made and showed that the API p-y curves overestimate the soil resistance. The trend is more pronounced at greater depths, which leads to an unconservative design of rigid piles. Adopting the API method has the potential to overestimate the horizontal capacity of the pile, thus risk the possibility that the pile will experience larger than predicted displacements in practice. As such, offshore wind turbines risk reaching the serviceability limit earlier than expected. Therefore, there is a need to modify the API formulation to better capture p-y behaviour. In order to modify the API method is a general form, it is necessary to have datasets covering a range of test parameters. However, it must be noted, that the above discussion is for monotonic response. The cyclic nature of loading on monopiles further complicates the analysis and changes in the p-y response is expected over the lifetime of the monopile. As such, the following chapter will examine the cyclic response of the monopile.

Chapter 5

Cyclic Test Results

5.1 Introduction

Eight tests were carried out to examine the effect of different loading scenarios on the pile behaviour, as shown in Table 5.1. All eight tests used the same configuration including the same sand, relative density, and pile location and installation. Four tests applied one-way loading with different loading magnitudes. The other four tests imposed two-way cyclic loading with different minimum and maximum loads, resulting in symmetric and asymmetric two-way loading. Among these two-way loading tests, the symmetric two-way loading tests have two different loading magnitudes, and the asymmetric loading varied in terms of the degree of asymmetry. The loading magnitude and the degree of asymmetry can be represented by two parameters, known as the cyclic magnitude ratio (or magnitude ratio), ζ_b, and the cyclic loading ratio (or cyclic ratio), ζ_c, which are defined by equations 2.40 and 2.41. The experimental control system was programmed to maintain a certain cyclic magnitude ratio and cyclic loading ratio throughout the test.

$$\zeta_b = \frac{H_{\max}}{H_{\text{ref}}} \tag{2.40}$$

$$\zeta_c = \frac{H_{\min}}{H_{\max}} \tag{2.41}$$

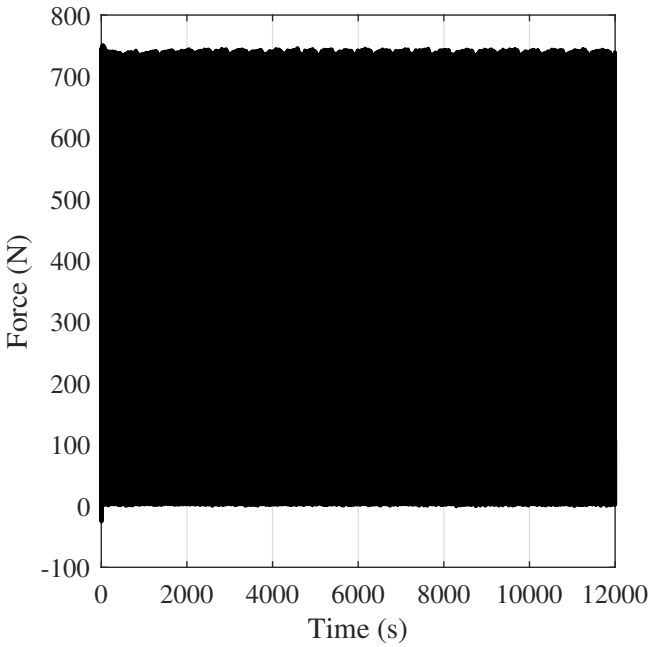
where H_{ref} is the reference horizontal load capacity of the pile (1400N in this study, from 4.2), and $H_{\max}$ and $H_{\min}$ are the maximum and minimum load of the cyclic loading, respectively. For one-way cyclic loading, ζ_c is equal to 0. For two-way cyclic loading, ζ_c is less than 0. Notably, $\zeta_c = -1$ represents symmetrical two-way cyclic loading. A smaller ζ_c value between 0 and -1 means a more symmetric loading scenario and a larger ζ_c value means the load tend to be more biased (similar to one-way load). The analysis was only conducted up to 20,000 cycles since it was the minimum number of cycles completed.

Table 5.1: Cyclic tests

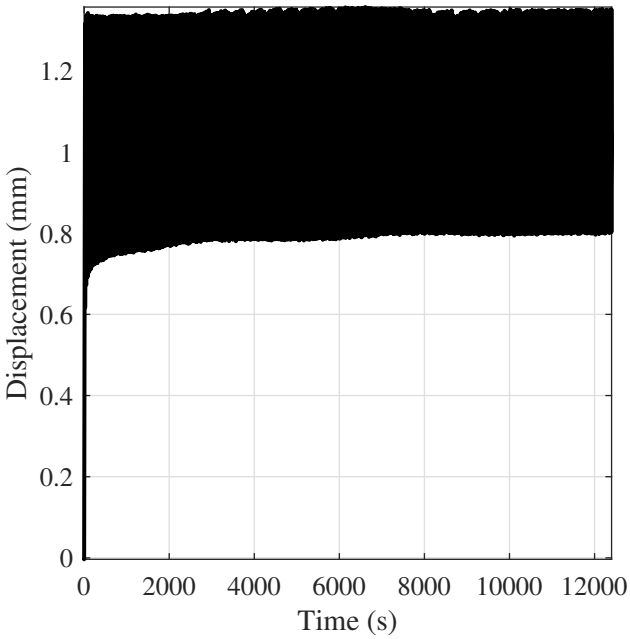
Tests	g-level	Relative density (I_D)	Minimum force (N)	Maximum force (N)	ζ_b	ζ_c	Number of cycles
kc01	62	90	0	530	0.39	0	60000
kc02	62	91	0	750	0.54	0	25000
kc03	62	91	0	1100	0.81	0	40000
kc04	62	92	-350	350	0.26	-1	40000
kc05	62	90	-350	700	0.52	-0.5	50000
kc06	62	91	-180	700	0.52	-0.26	40000
kc07	62	90	-525	525	0.39	-1	35000
kc08	62	90	0	890	0.66	0	26000

5.2 Pile head displacement

Figure 5.1 shows the force and head displacement for test kc02 over the duration of the centrifuge test. The plots for the remainder of the tests are provided in Appendix A,Figure A.1 and Figure A.3. To improve readability, force against pile head displacement for key cycles (n= 1, 10, 100, 1000, 10000, and 20000) is plotted for all the tests, as shown in Figure 5.2 and 5.3.



(a) Force in kc02

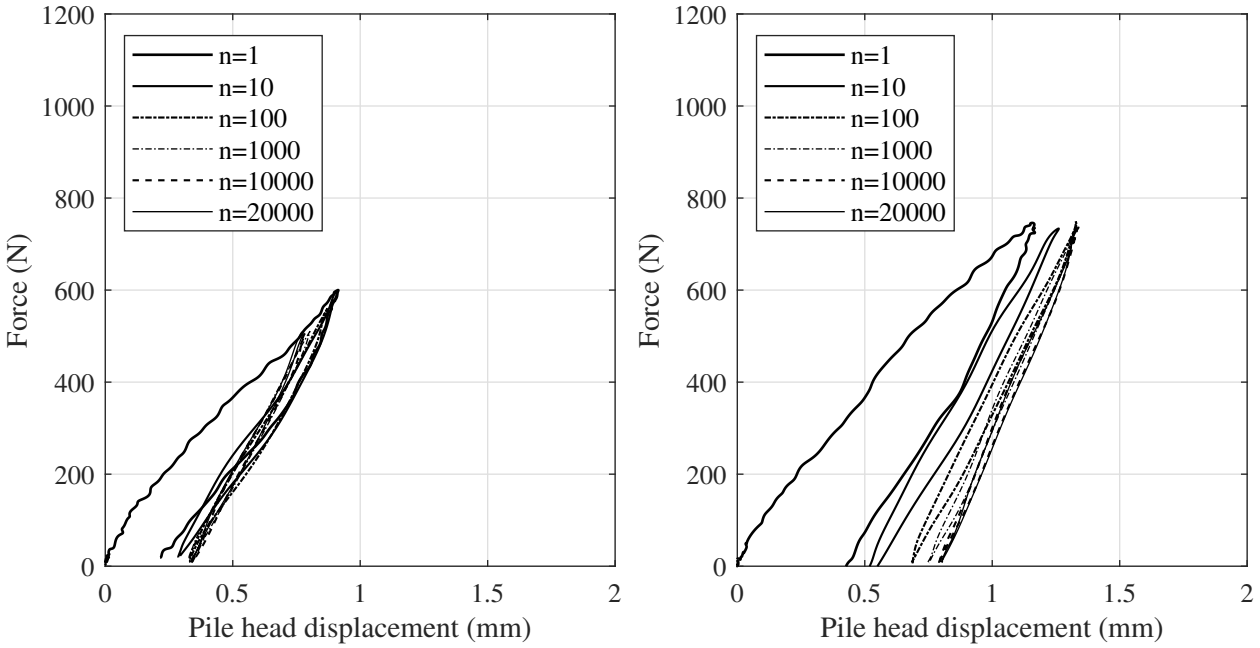


(b) Displacement in kc02

Figure 5.1: Force and pile head displacement for kc02

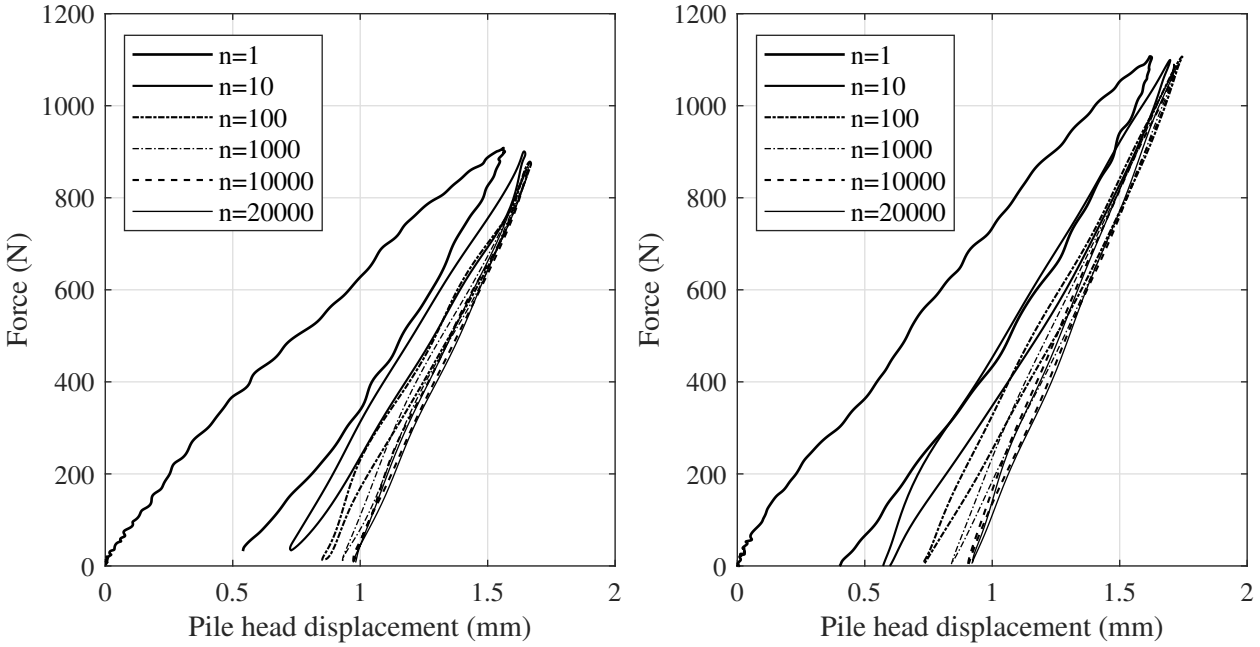
In general, the force-displacement curve for one-way tests (kc01, kc02, kc03, and kc08) is shifting to the right and the overall slope is increasing, indicating that the head displacement is accumulating and the soil-pile response is becoming stiffer with increasing cycle number. In terms of two-way tests (kc04, kc05, kc06, and kc07), the force-displacement curve is relatively symmetrical with reference to the origin for symmetric two-way loading (tests kc04 and kc07) and the slope is growing over the number of cycles. For biased two-way loading tests (kc05 and kc06), the overall response is similar to that of one-way loading, except the maximum pile head

displacement is decreasing in this case in contrast to accumulation for one-way loading tests. This reduction of pile head displacement is also observed in symmetrical two-way loading tests. Regardless of loading characteristics, all tests demonstrate an increase in the overall slope of the force-displacement curve, in other words, the pile-soil interaction is stiffer over time for all loading scenarios. This phenomenon agrees with Klinkvort (2012) and LeBlanc et al. (2010a). In addition, a common trend occurs for all the tests that the force-displacement curve tends to stabilise after 10000 cycles; the curve at cycle 20000 resembles that at cycle 10000 cycles.



(a) kc01, $\zeta_b = 0.39, \zeta_c = 0$

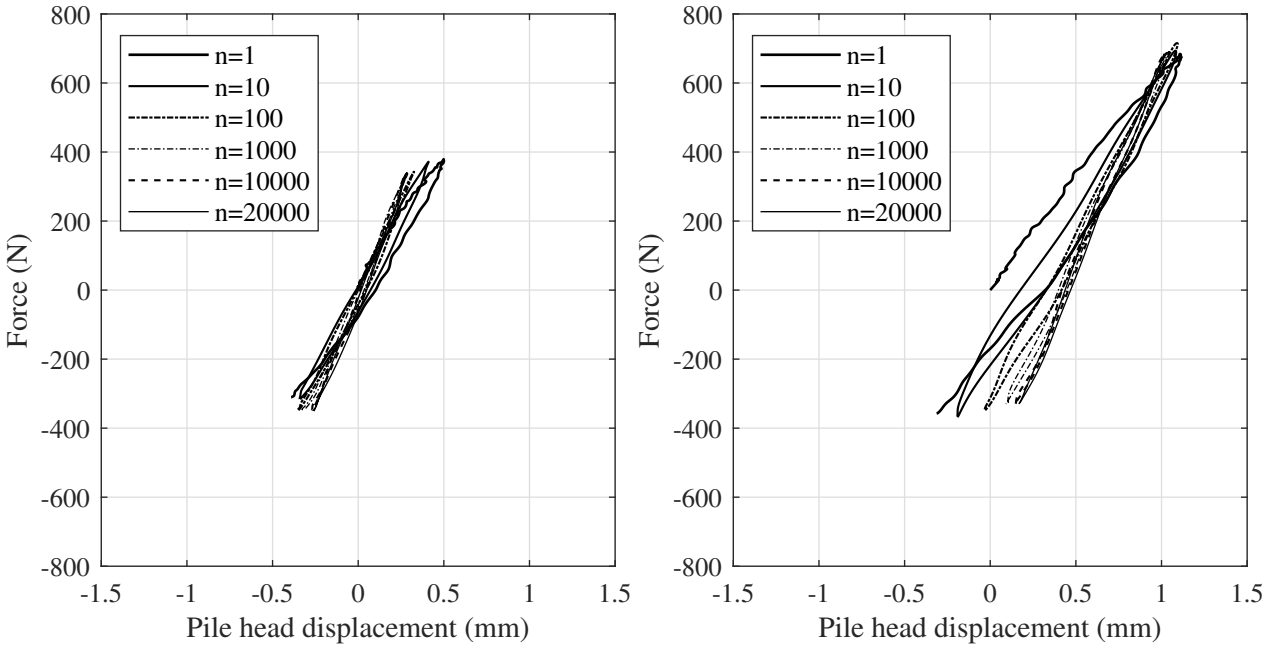
(b) kc02, $\zeta_b = 0.54, \zeta_c = 0$



(c) kc08, $\zeta_b = 0.66, \zeta_c = 0$

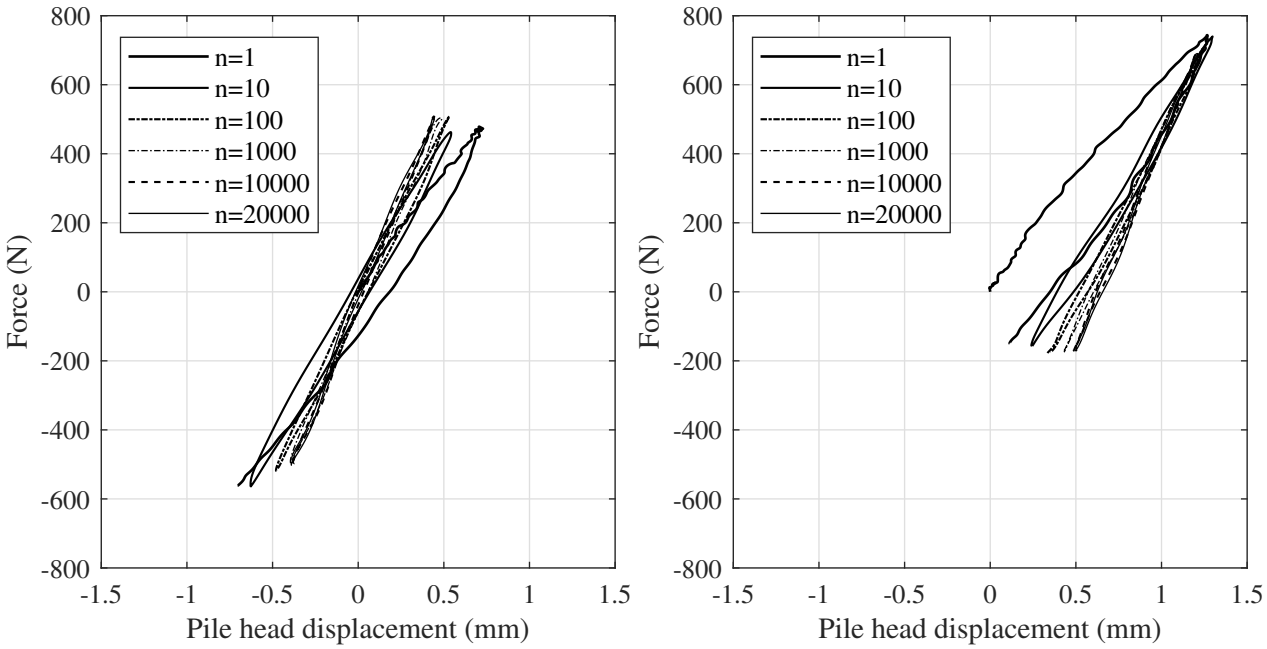
(d) kc03, $\zeta_b = 0.81, \zeta_c = 0$

Figure 5.2: Force against head displacement for the nth cycle



(a) kc04, $\zeta_b = 0.26, \zeta_c = -1$

(b) kc05, $\zeta_b = 0.52, \zeta_c = -0.5$



(c) kc07, $\zeta_b = 0.39, \zeta_c = -1$

(d) kc06, $\zeta_b = 0.52, \zeta_c = -0.26$

Figure 5.3: Force against head displacement for the nth cycle (continued)

A close comparison of the force-displacement curve at the first cycle between tests was made, see Figure 5.4 and 5.5. It can be seen that the load-displacement path of the first cycle generally follows the monotonic backbone curve. During unloading in the one-way loading tests, the displacement reduces, however it does not return to zero, at zero load. This offset in displacement at zero load is referred to as the 'residual displacement' and discussed in detail later.

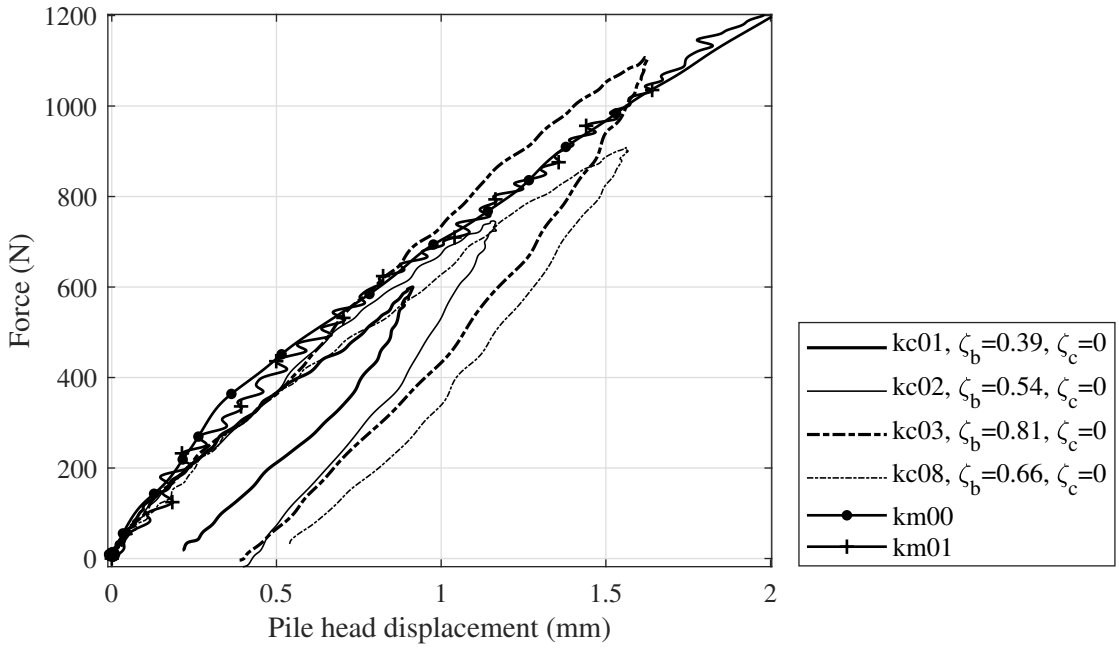


Figure 5.4: One-way 1st cycles

In terms of two-way loading tests, it is useful to consider the magnitude of the displacement reached during the forward loading and reverse loading phases of the cycle. The difference between these displacement values naturally depends on the load magnitude applied in the forward and reversal directions. For symmetric loading (i.e. where the load magnitude in the forward direction was intended to equal the load magnitude in the reversal direction – tests kc04, kc07), the displacement magnitude obtained on reversal is similar to that obtained during the forward loading. However, the magnitudes are not identical – for example, in kc04, a dis-

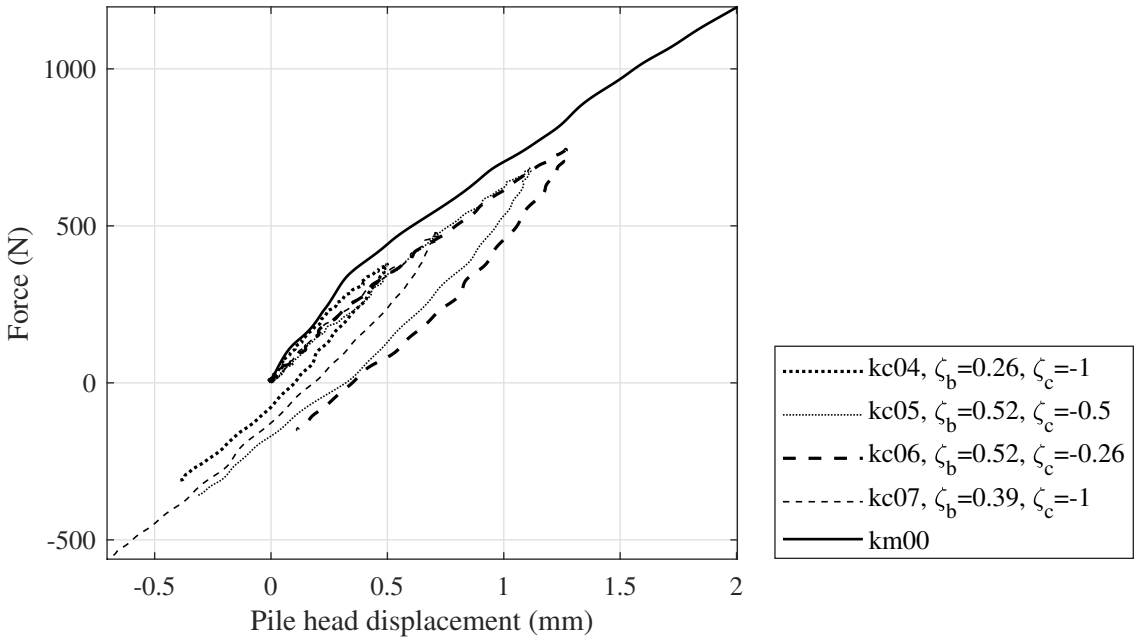


Figure 5.5: Two-way 1st cycles

placement of 0.5mm was obtained in the forward direction, whereas a displacement of -0.4mm was obtained in the reversal direction. This can be partly attributed to the bias caused by the initial loading direction, but it should also be noted that perfect symmetric loading was not achieved whereby in kc04 the reversal load magnitude was lower than that of the forward direction. In test kc07 the reversal load magnitude was marginally larger than the forward load magnitude and this resulted in the displacement magnitude in the reversal direction equalling the displacement magnitude in the forward direction. As such, it may be concluded that in perfect symmetric loading cases, the reversal displacement magnitude would not be the same as the forward displacement magnitude. For biased two-way loading, it is interesting to note that the magnitude of the bias for test kc06 ($\xi_c = -0.26$) was insufficient to cause the pile head displacement to move past (in the negative direction) the zero displacement point - i.e. the displacement of the pile remained on the 'forward' direction despite negative load being applied to the pile. However, the increased bias loading deployed in test kc05 ($\xi_c = -0.5$) was sufficient

to cause the pile-head to move into the negative displacement zone.

The maximum and minimum pile head displacement was extracted from every cycle and plotted in Figure 5.6 and Figure 5.7, respectively. On the one hand, the maximum pile head displacement is noted to accumulate for one-way tests, except for kc01 in which the load was overshot and then returned to the target load. In addition, it is evident that the maximum head displacement is positively connected to the magnitude of loading. These observations are in agreement with Klinkvort (2012). On the other hand, decreasing head displacement was observed for two-way tests, with the exception of kc06 where the cyclic loading ratio is the highest among two-way tests leading to a one-way-like response. Comparing kc05 and kc06, it is reasonable to suggest that there is a positive correlation between the cyclic ratio and maximum pile head displacement. In other words, increasing the cyclic ratio or the scale of bias of the one-direction force of the two-way loading leads to a higher pile head displacement. This leads to a conclusion that one-way loading is more critical than two-way loading. This is supported by the comparison between kc01 and kc07 as well as kc05, kc06, and kc02. Although maximum pile head displacement for kc06 was higher than kc02 at a low number of cycles (less than 10 cycles), which is likely due to the sand's relative density, kc02 quickly overtook kc06 by the time 20 cycles were imposed. Therefore, it can be concluded that one-way loading is a worse scenario compared to two-way loading. This finding agrees with Klinkvort (2012) but contradicts LeBlanc et al. (2010a), where two-way tests were found to be more damaging (in terms of accumulated pile head displacement). It can also be observed that for tests in which the cyclic ratio remained constant but where the absolute load magnitude increased (kc04 vs kc07), in line with expectations, the corresponding pile head displacement also increased.

With respect to long-term behaviour, the pile head displacement tends to level off after a

certain number of cycles regardless of loading characteristics. Although it took a different number of cycles to reach a stable value for different tests, they were almost stable after 10^4 cycles. This disagrees with LeBlanc et al. (2010a), where exponential functions were applied to model the maximum pile head displacement suggesting an on-going increase in head displacement at large numbers of cycles. Since LeBlanc et al. (2010a) conducted tests at 1-g level, the results from this study should be more reliable. From the results presented in Figure 5.6, it can be observed that there is a complex relationship between displacement and cyclic ratio. As such, it is not possible to develop a model to represent this behaviour. However, based on the experimental data, it is apparent that pile head displacement does not increase indefinitely and it is necessary to further investigate the long-term response of piles under cyclic loading.

In terms of minimum pile head displacement, as shown in Figure 5.7, the overall trend is consistent for all tests that minimum pile head displacement increases with cycle number and intimately reaches a plateau. The one-way tests clearly experience higher pile head displacement compared to the two-way tests, as the opposing forces in two-way tests reduced the pile head displacement – agreeing with the observations made from the maximum pile head displacement results.

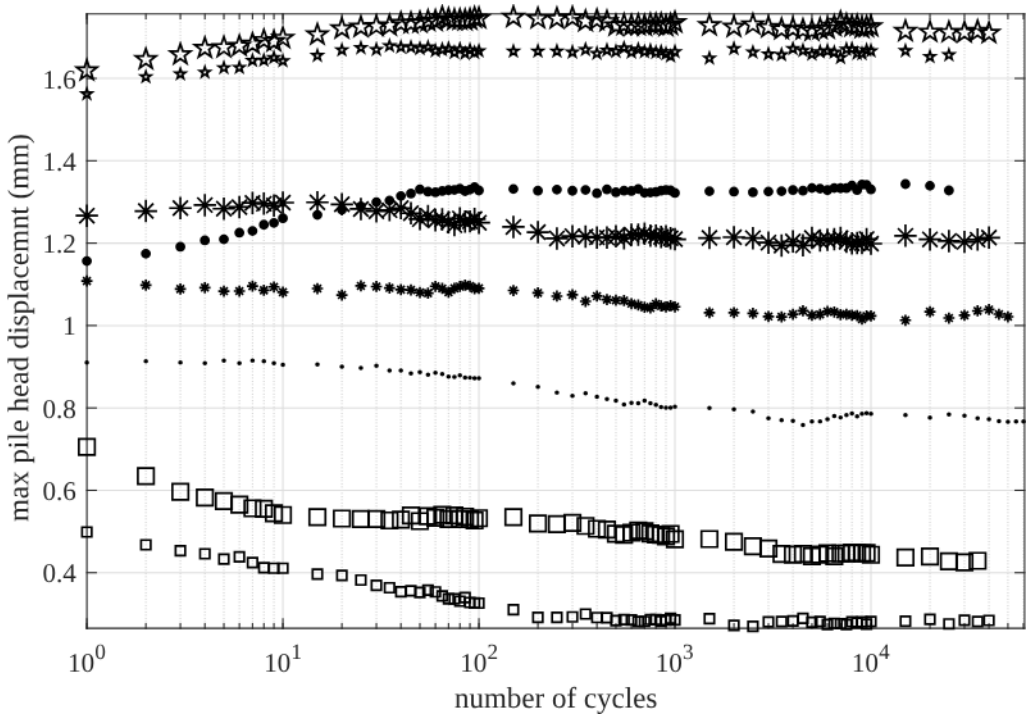


Figure 5.6: Maximum displacement

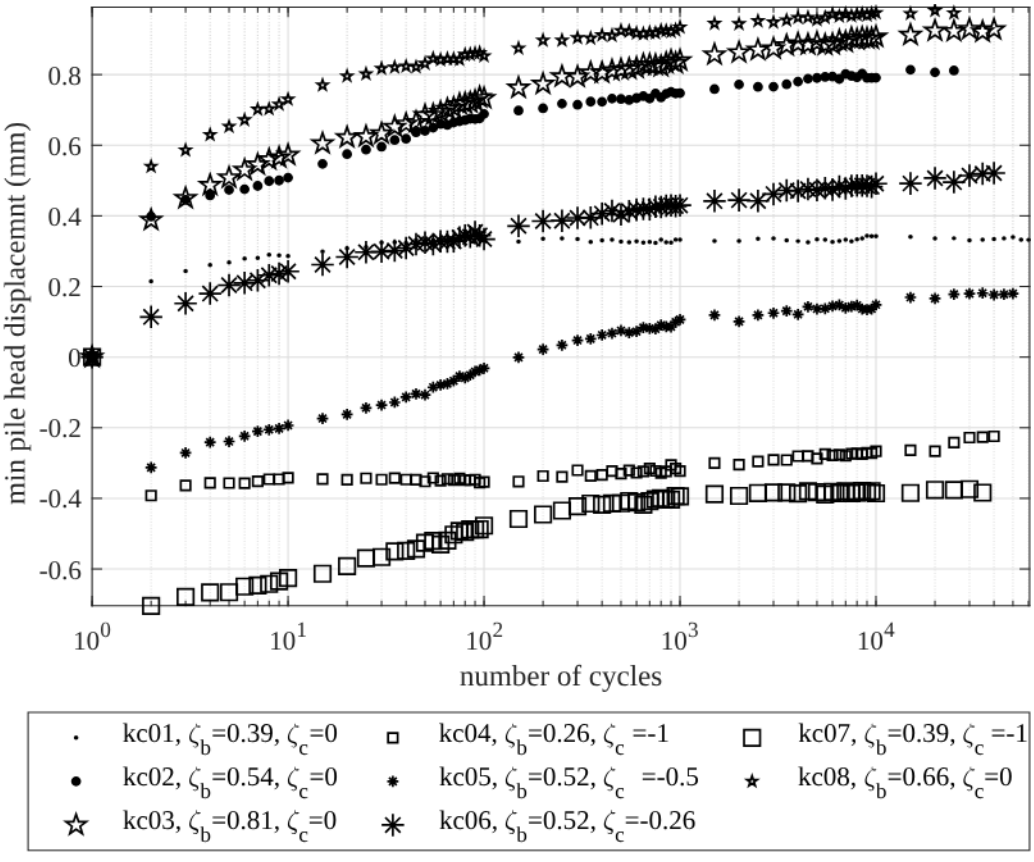


Figure 5.7: Minimum displacement

5.3 Pile secant stiffness

As shown in Figure 5.8, the pile secant stiffness is defined by the slope between the maximum load point and the minimum load point at a cycle and is calculated by Equation 5.1. The definition of the secant stiffness is consistent with Klinkvort (2012).

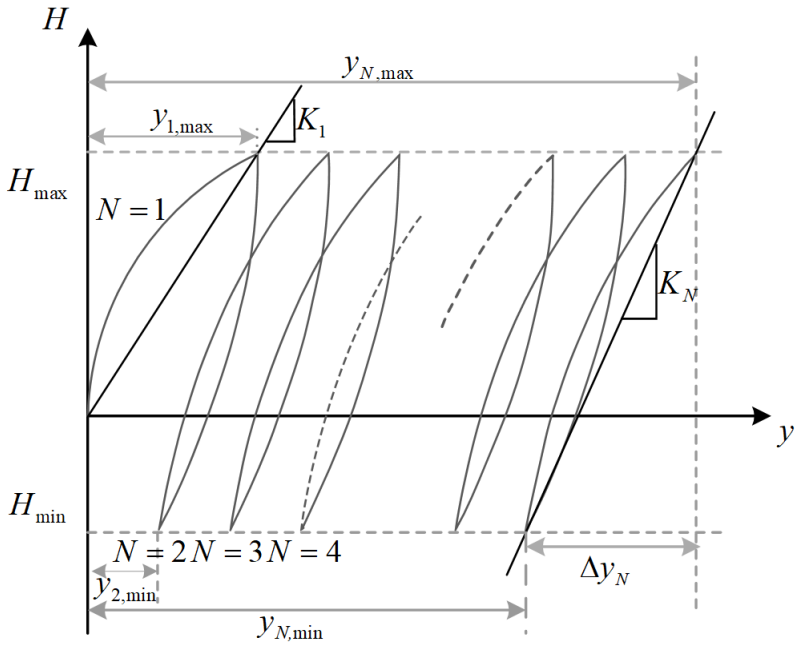


Figure 5.8: Pile secant stiffness definition

$$K_N = \frac{H_{N,\max} - H_{N,\min}}{y_{N,\max} - y_{N,\min}} \tag{5.1}$$

where $H_{N,\max}$ and $H_{N,\min}$ are the maximum and minimum load at the N^{th} cycle, respectively. $y_{N,\max}$ and $y_{N,\min}$ are the maximum and minimum displacement at the N^{th} cycle respectively, as also shown in Figure 5.8.

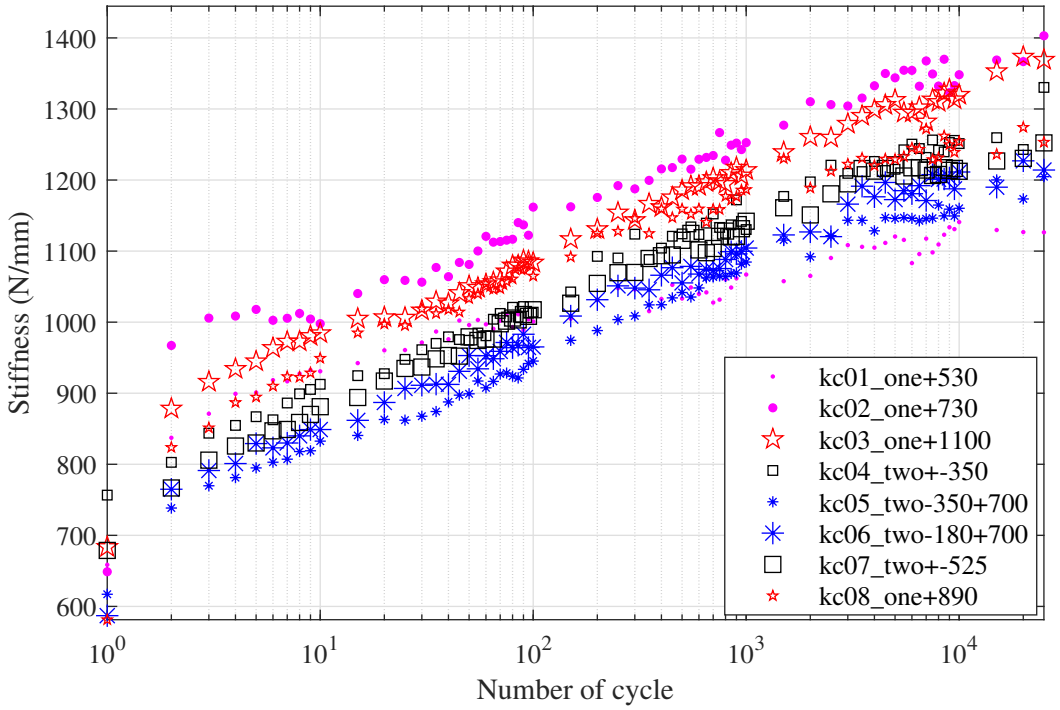


Figure 5.9: The secant stiffness against cycles

Figure 5.9 shows the secant stiffness K_N against cycle number. Overall, the stiffness increases with the number of cycles regardless of loading characteristics. This is in agreement with the finding from LeBlanc et al. (2010a) and Klinkvort (2012). Two mechanisms are behind this increase in stiffness. The first one regarding the soil at shallow depth is proposed by Cuéllar (2011). It is suggested that the pile pushes the sand upwards while loading and the sand falls into the gap in front of the pile formed during unloading. When the pile is loaded again, the front sand is compacted leading to a stiffer behaviour. The other explanation is concerned with soil at greater depth. Kirkwood (2015) points out that dense sand around the pile, even at depth where the confining stresses are higher, still tends to dilate and thus cause a stiffer soil-pile interaction. As the pile moves forward during loading, the volume of dilating soil keeps increasing and applies stress to the pile, which leads the stiffness to increase. However, the volume of the rearranged soil eventually reaches a peak after a certain number of cycles and the stiffness starts

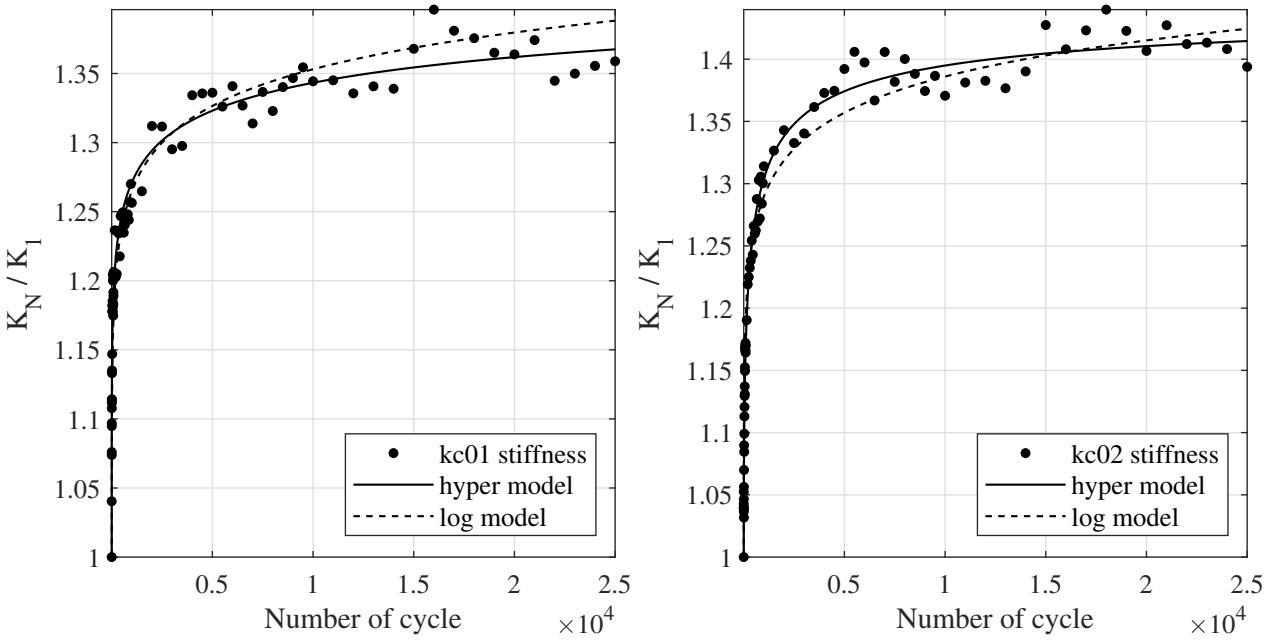
to stabilise, which also explains the levelling off trend of maximum pile head displacement. It is apparent that stiffness for kc05 and kc08 show a plateau after 10^4 cycles, which is also observed in Cuéllar (2011). The rest of the tests show a sign of stabilisation and are expected to level off after more cycles.

An empirical method using the logarithm function, see Equation 5.2, to predict stiffness was proposed by Klinkvort (2012). While the model shows a relatively plausible fit to the stiffness development, it does not account for the fact that the stiffness is expected to level off after a certain number of cycles. Therefore, a hyperbolic model is proposed here to fit the stiffness. The model is given by Equation 5.3, which involves three parameters a,b, and c. This type of asymptotic relationship has also been adopted for cyclic response of sands (Cha et al., 2023). Comparison between these two models is demonstrated in Figure 5.10 and Figure 5.11, where the secant stiffness is normalised with respect to the secant stiffness at the first cycle, K_1. As shown in Figure 5.10 and Figure 5.11, both models yield reasonable fits to the normalised stiffness for all tests for the given cycles, especially for test kc03 (one-way test, 1100 N). However, the discrepancy between them becomes pronounced for test kc08 (one-way test, 890 N), in which the normalised stiffness levels off after about 10^4 cycles. This discrepancy between the normalised stiffness and the logarithm model is expected to appear for the other tests after a certain number of cycles. Although the logarithm model resembles the hyperbolic model for the cycle range, it is clear that the difference is going to grow with the number of cycles. In this study, the total number of cycles is 20000, which is substantially less than the total cycles of an offshore wind turbine during its life cycle. Therefore, the logarithm model will overestimate the stiffness in the long term

and the newly proposed hyperbolic model is recommended to predict stiffness development.

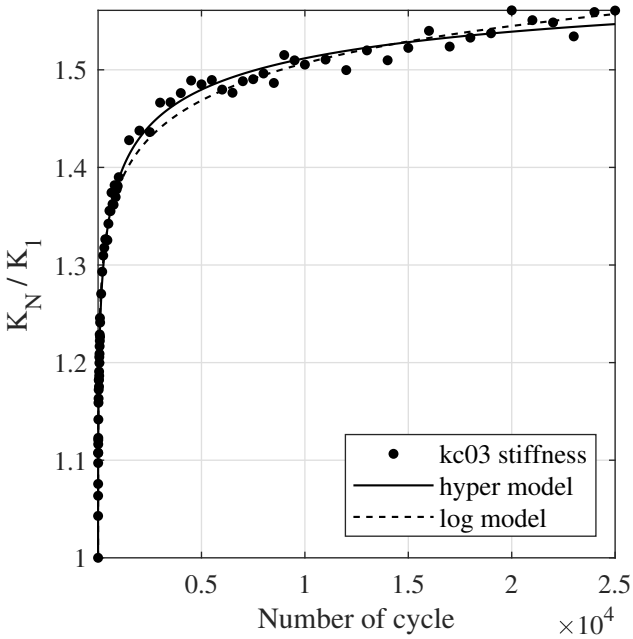
$$\frac{K_N}{K_1} = 1 + \kappa \ln(N) \tag{5.2}$$

$$\frac{K_N}{K_1} = \frac{a}{1 + \exp\left[-b(\ln(N-1) - c)\right]} + 1 \tag{5.3}$$

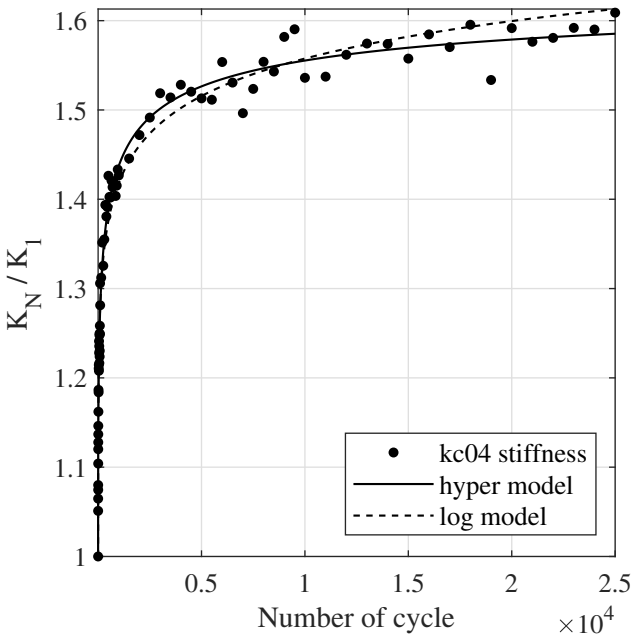


(a) kc01

(b) kc02

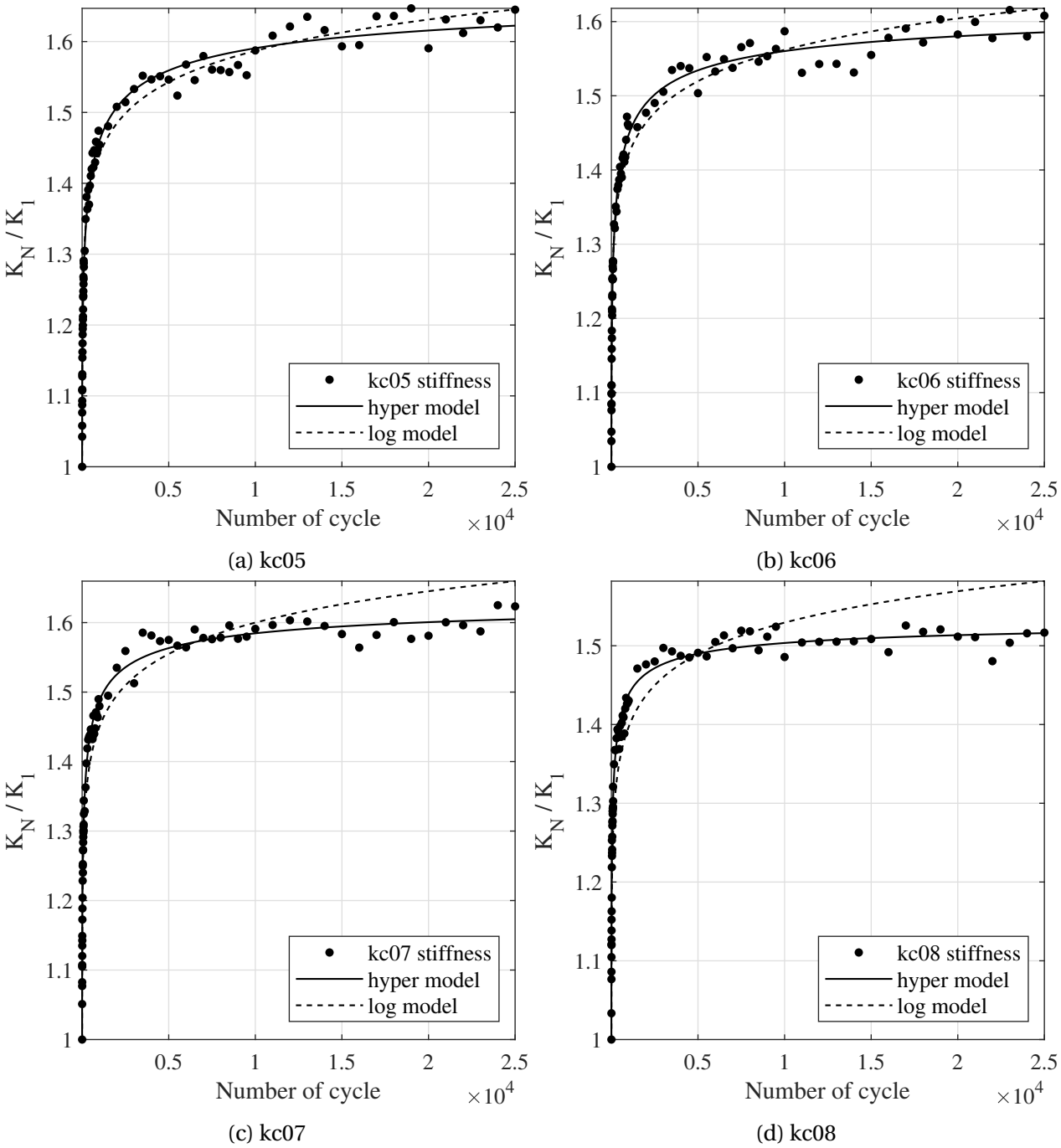


(c) kc03



(d) kc04

Figure 5.10: Normalised stiffness against the cycle number



(a) kc05

(b) kc06

(c) kc07

(d) kc08

Figure 5.11: Normalised stiffness against the cycle number (continued)

Figure 5.12 shows the secant stiffness normalised by the first cycle stiffness against cycle number for all tests in a log scale. With respect to one-way tests, the normalised stiffness is greater for higher loading magnitude, except kc03 whose normalised stiffness is less than kc02 and kc08. This exception is likely due to its first-cycle load versus displacement curve being higher than the monotonic backbone, leading to a higher stiffness at the first cycle, whereas other tests present a lower or similar load versus displacement curve compared to the monotonic test for the first cycle. In terms of two-way tests, the increasing load magnitude also corresponds to higher normalised stiffness, as the magnitude of normalised stiffness of kc05, kc07, and kc04 (or kc06, kc07, and kc04) are in declining order.

A close look at the parameter a in the hyperbolic model (Equation 5.3), which controls the maximum value of the normalised stiffness, shows a strong positive correlation with the cyclic magnitude ratio – see Figure 5.13. Therefore, normalised stiffness is positively related to load magnitude, which was also found to be the case in LeBlanc et al. (2010a) and Klinkvort (2012). Comparing kc05, kc06, and kc02, the normalised stiffness increases with cyclic ratios, as shown in Figure 5.13. In other words, one-way loading leads to higher normalised stiffness in relation to two-way loading provided the maximum load is the same for both cases. Referring again to Figure 5.12, it is observed that kc01 shows lower normalised stiffness relative to kc07 after 300 cycles, which is a result of the applied force overshooting the target load during kc01. The force increased to 600 N and then back to 530 N, causing increased densification and as such an increase in the stiffness recorded. Therefore, the rate of increase is reduced and the plateau was reached earlier. Had the force been controlled properly, it would have supported the positive relation between normalised stiffness and cyclic ratio. However, this finding contradicts Klinkvort (2012), in which the normalised stiffness is negatively affected by the cyclic ratio, but

agrees with LeBlanc et al. (2010a), where there is a positive correlation between the normalised stiffness and the cyclic ratio. That said, the results from LeBlanc et al. (2010a) could perhaps be considered not as reliable as those from this testing and the testing of Klinkvort (2012), as LeBlanc et al. (2010a) carried out the testing at 1-g. The challenge with testing at 1-g is that the prototype stresses are not accurately replicated within the model. The dilatant behaviour of soil depends on both relative density and the effective confining stress – with an increase in effective confining stress or a reduction in relative density resulting in a less dilatant behaviour. As such, in order to better replicate the dilatant behaviour of the prototype scenario, LeBlanc et al. (2010a) used soil bodies with a low relative density to counter the impact of the low effective confining stresses experienced at 1-g. However, quantitatively this 'correction' to address the issues around dilation will be absolute and as such some error in the stiffness behaviour of the soil body is still to be expected. It is more informative to consider the contradiction in the results obtained in this recent testing to the resulted obtained by Klinkvort (2012). In the tests conducted as part of this thesis, the sand around the pile may have been looser compared to the distant sand because of the method of preparing the model (the supports for the pile during sand pouring will have impacted the pouring of the sand adjacent to the pile) (See section 3.3.3). In addition, the force applied in this study is smaller relative to Klinkvort (2012). The combination of the lower relative density around the pile and the reduced head loads would contribute to the lower stiffness observed in this study.

It has been discussed above how the parameter a from the hyperbolic model, which dictates the projected maximum stiffness that will be obtained, can be correlated to cyclic loading ratio and cyclic magnitude ratio. There are two further parameters which form the hyperbolic model: b and c. Together, parameters b and c control the rate of change of normalised stiffness with

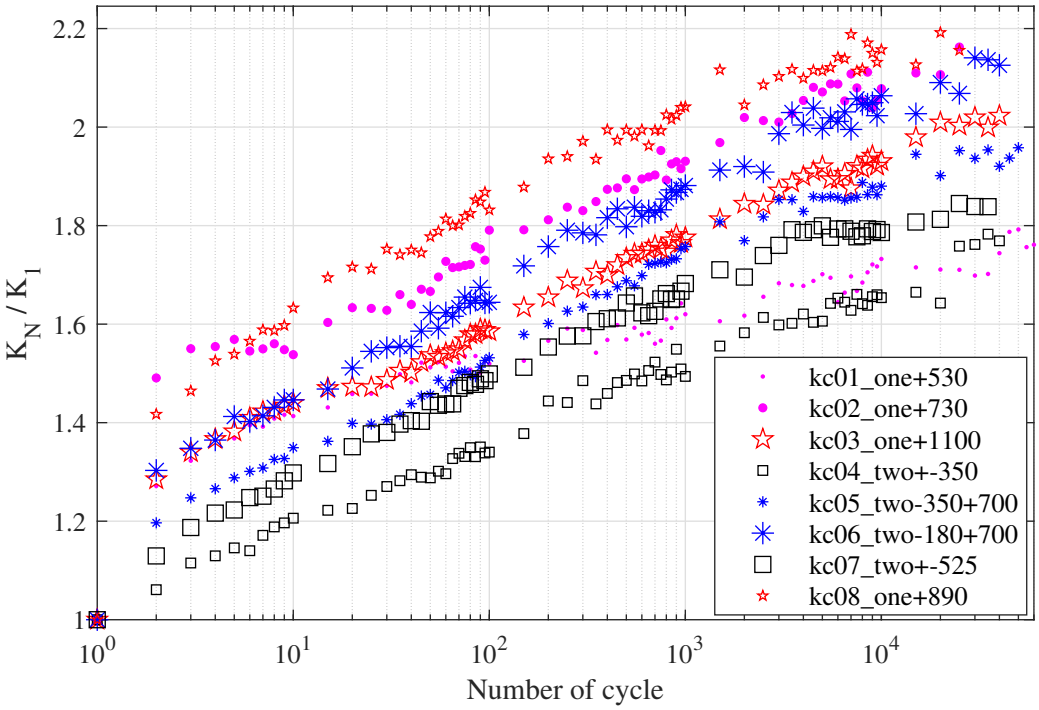
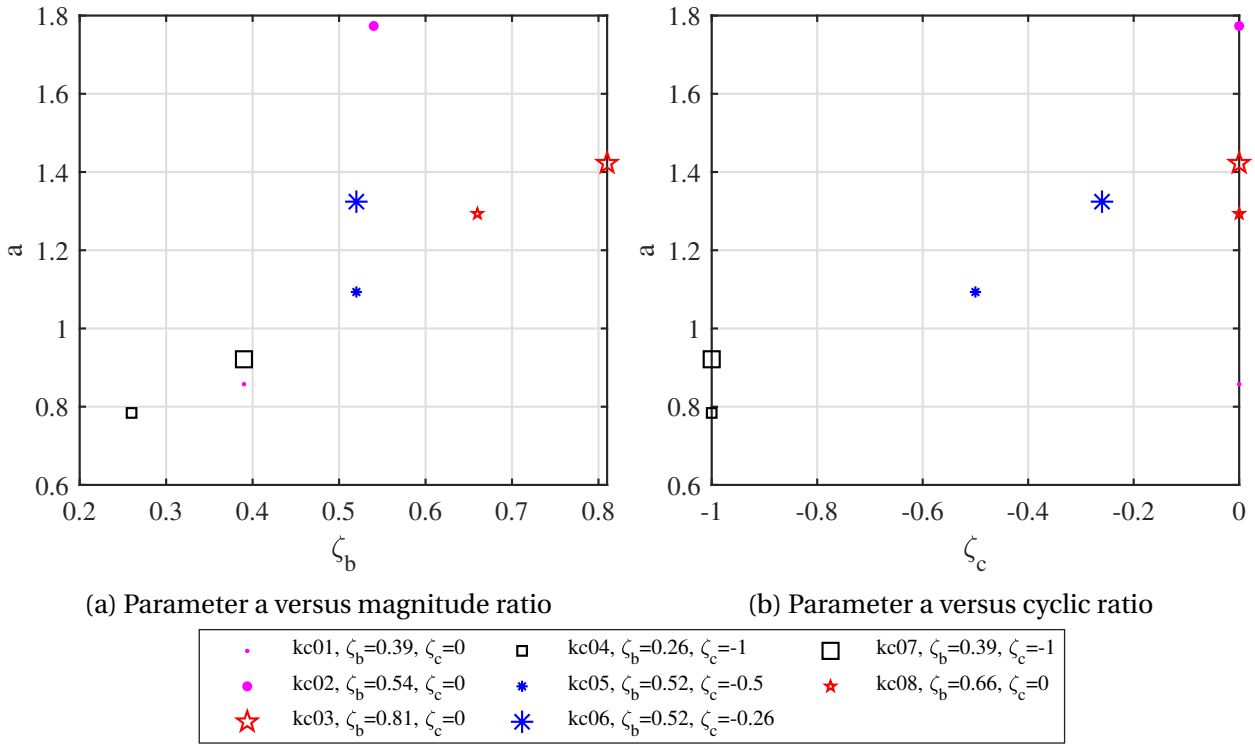


Figure 5.12: Normalised stiffness

cycle number. The relationship between b and c with the cyclic loading ratio and cyclic magnitude ratio are given in Figure 5.14. As can be observed in the plots, there is no clearly discernible relationship, though there could be some argument made that parameter b is negatively correlated with cyclic loading ratio and cyclic magnitude ratio. It is informative to consider the relative impact of parameters b and c on the rate of change. The part of the denominator of the hyperbolic function which involves these two parameters is: $b(\ln(N-1)-c)$. If we consider the value at 5000 cycles (i.e. $N = 5000$), and a typical $b = 0.6$, over the range of $1 < c < 2.8$, then the factor varies from 4.5 to 3.4 (25% change). Whereas, if we again consider the value at 5000 cycles (i.e. $N = 5000$), and a typical $c = 2$, over the range of $0.4 < b < 0.9$, then the factor varies from 2.5 to 5.7 (225% change). As such, it can been observed, that over the range of values obtained, the rate of change of normalised stiffness is more sensitive to parameter b than parameter c. As such, it follows that a stronger correlation, if indeed one exists, would be expected between



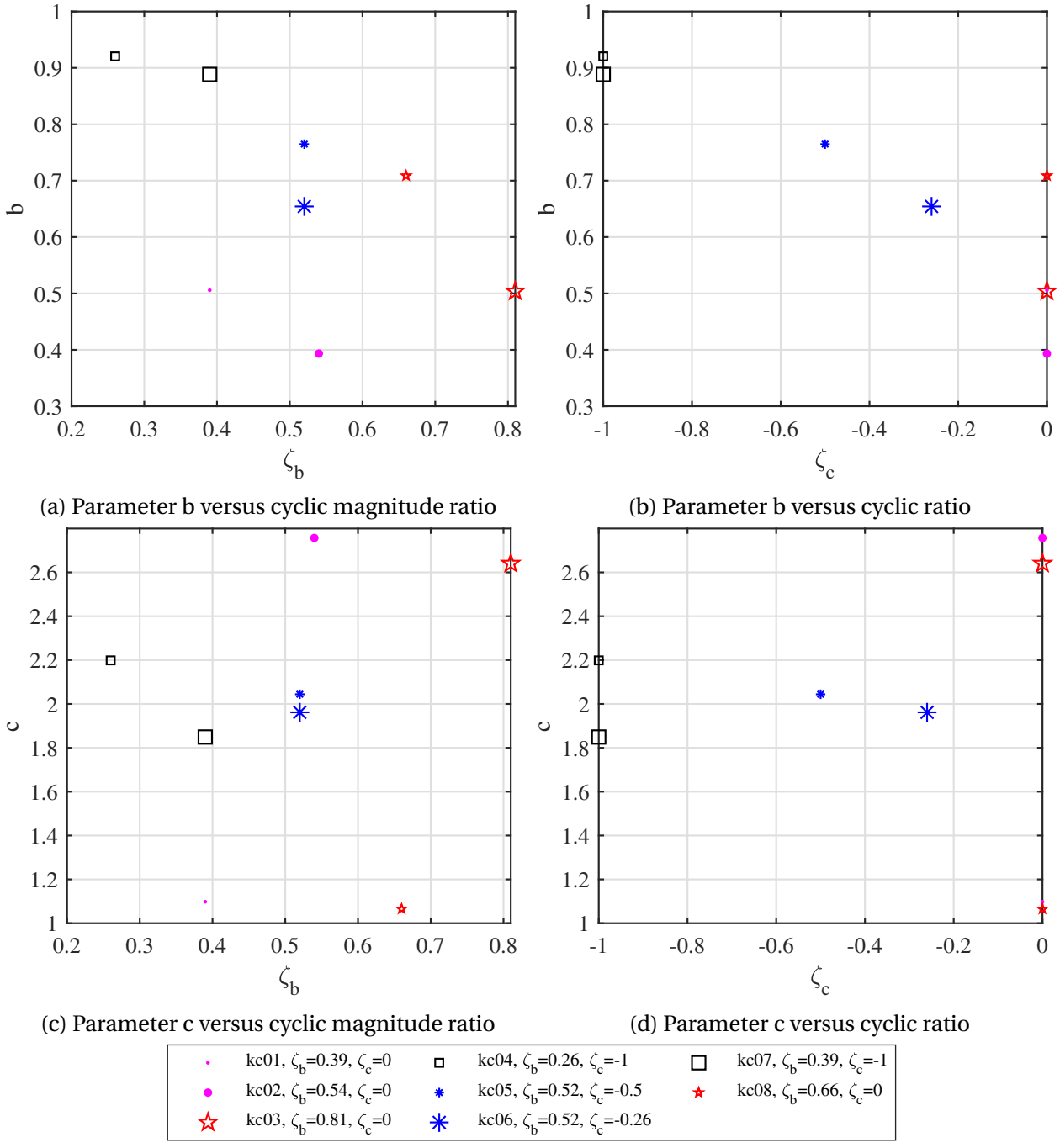
(a) Parameter a versus magnitude ratio

(b) Parameter a versus cyclic ratio

Figure 5.13: Coefficients with cyclic magnitude ratio and cyclic loading ratio

parameter *b* and the cyclic loading ratio and cyclic magnitude ratio.

However, ultimately, engineers are interested in the initial and final stiffness values and hence the actual rate of change over cycles does not prove to be that useful in practice. Therefore the strong correlations observed between parameter *a* and the cyclic loading ratio and cyclic magnitude ratio are far more informative and provide a significant insight from this new research.



(a) Parameter b versus cyclic magnitude ratio

(b) Parameter b versus cyclic ratio

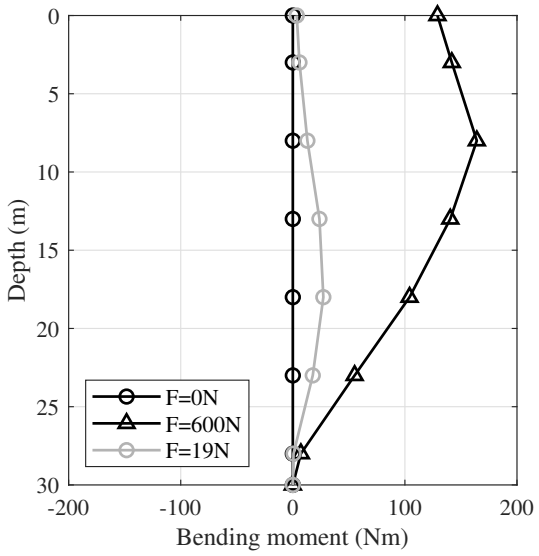
(c) Parameter c versus cyclic magnitude ratio

(d) Parameter c versus cyclic ratio

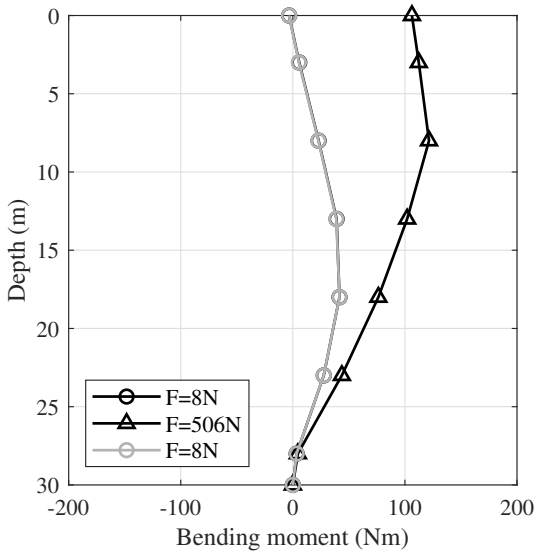
Figure 5.14: Coefficients with cyclic magnitude ratio and cyclic loading ratio

5.4 Bending moments

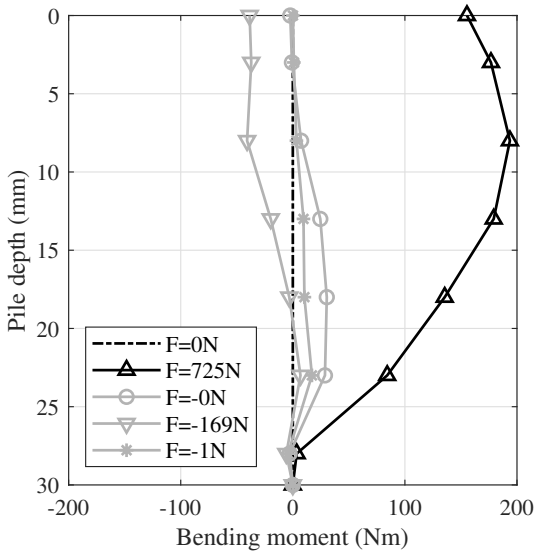
Bending moments along the pile can be evaluated using the strain data collected from the FBGs. Examination of how the bending moment develops over successive cycles is informative. To illustrate the development, bending moments from two representative cycles (1 and 10000) are selected, as shown by example in Figure 5.15. For one-way tests, bending moments at all depths increased with increasing force until reaching a maximum value and then decreased as the force reduced within a cycle. However, the bending moment did not dissipate to zero when the load reduced to zero except at the sand surface and at the pile toe, leaving a residual bending moment along the pile, which is often referred to as a 'locked-in' bending moment. In contrast, the general profile of bending moment development for two-way tests differs greatly and is heavily dependent on the loading symmetry. For symmetric loading, e.g. kc04 and kc07, the bending moment is highly symmetric and only a small amount of locked-in bending moment is present along the pile after the first cycle. With respect to biased loading, e.g. kc05 and kc06, the bending moment profile lies in between one-way tests and symmetric two-way tests: with a higher loading bias, i.e. kc06, the profile tends to resemble the one-way loading scenario. With a higher loading symmetry, i.e. kc05, the profile tends to become symmetric.



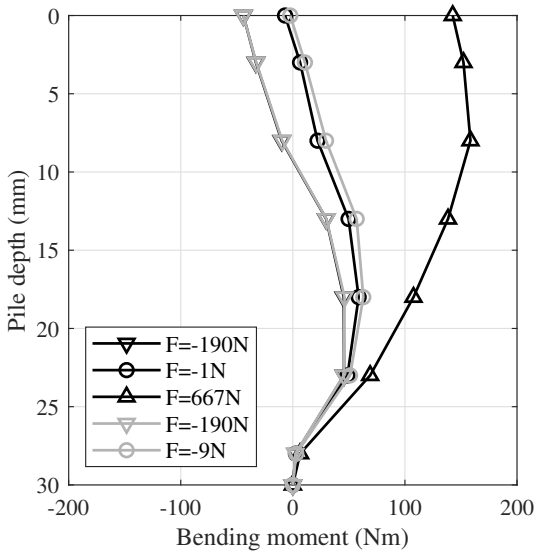
(a) kc01_one+530 N=1



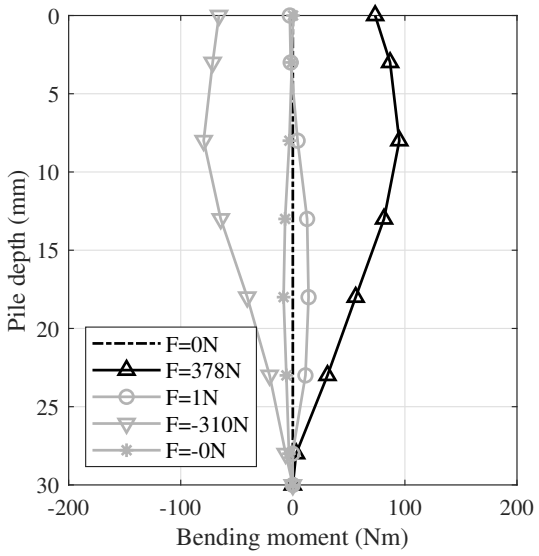
(b) kc01_one+530 N=10000



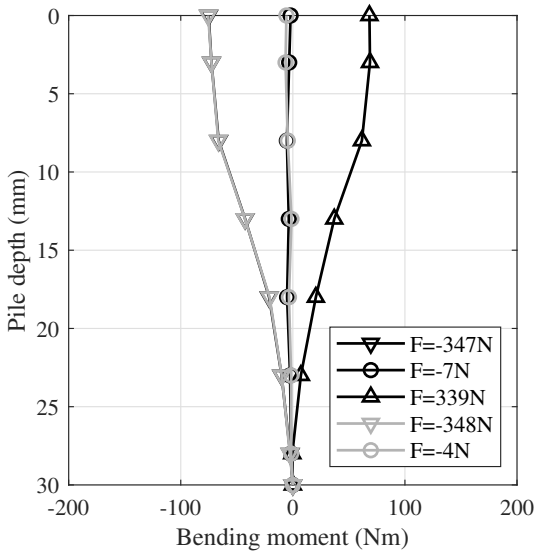
(c) kc06_two-180+700 N=1



(d) kc06_two-180+700 N=10000



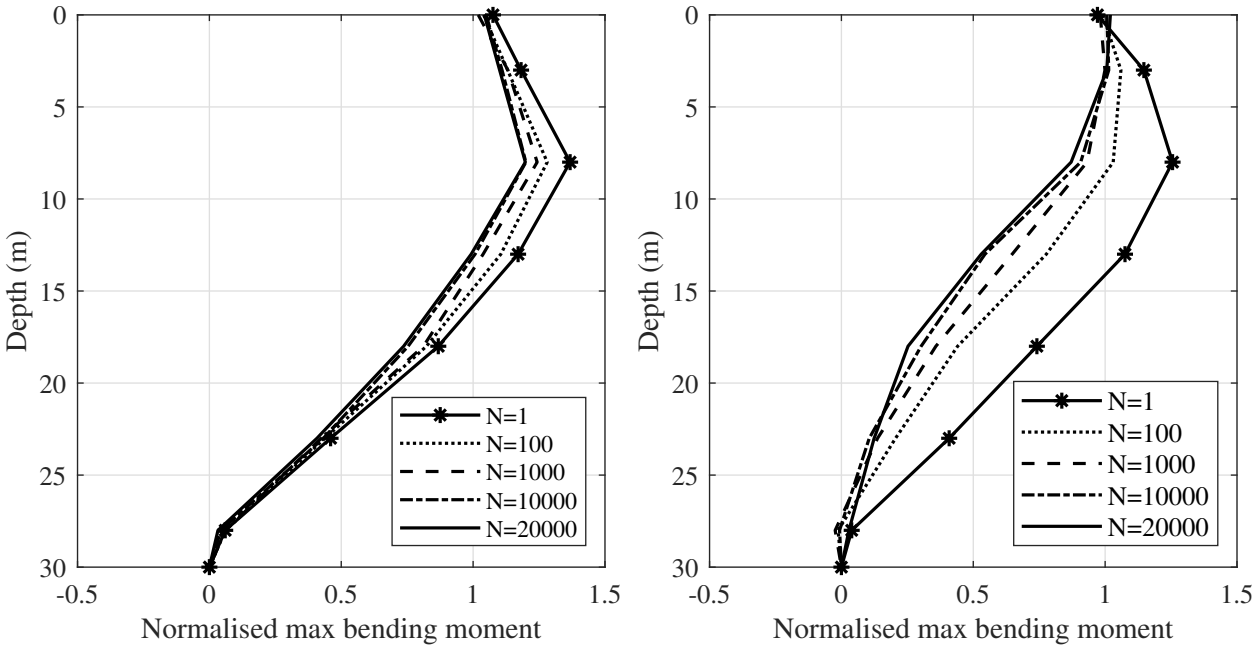
(e) kc04_two+-350 N=1



(f) kc04_two+-350 N=10000

Figure 5.15: BM development for cycle 1 and 10000

Due to the method of loading the pile, the loads obtained (both the maximum and minimum) are not entirely consistent between cycles. In order to permit better comparisons between cycles and between tests, the bending moments will be discussed in the context of normalised bending moment profiles. This normalisation process involved taking the bending moment profile during any particular cycle and dividing it by the theoretical *absolute* maximum bending moment at the mud-line during that cycle (i.e. the force applied multiplied by the offset to the mud-line). For sake of clarity, this means, when the load applied is positive, the bending moments are divided by the positive maximum bending moment during that cycle, whereas when the load applied is negative, the bending moments are divided by the negative maximum (i.e. overall minimum) bending moment during that cycle. It should be noted that this theoretical bending moment at the mud-line may not match the bending moment at the mud-line from the bending moment profiles – this deviation is due to errors in the bending moment computation from the FBGs as discussed in Section 4.3. A such, the normalised bending moment at the mud-line may not always be equal to one, but should be very close.



(a) kc01_one+530

(b) kc04_two+-350

(c) kc05_two-350+700

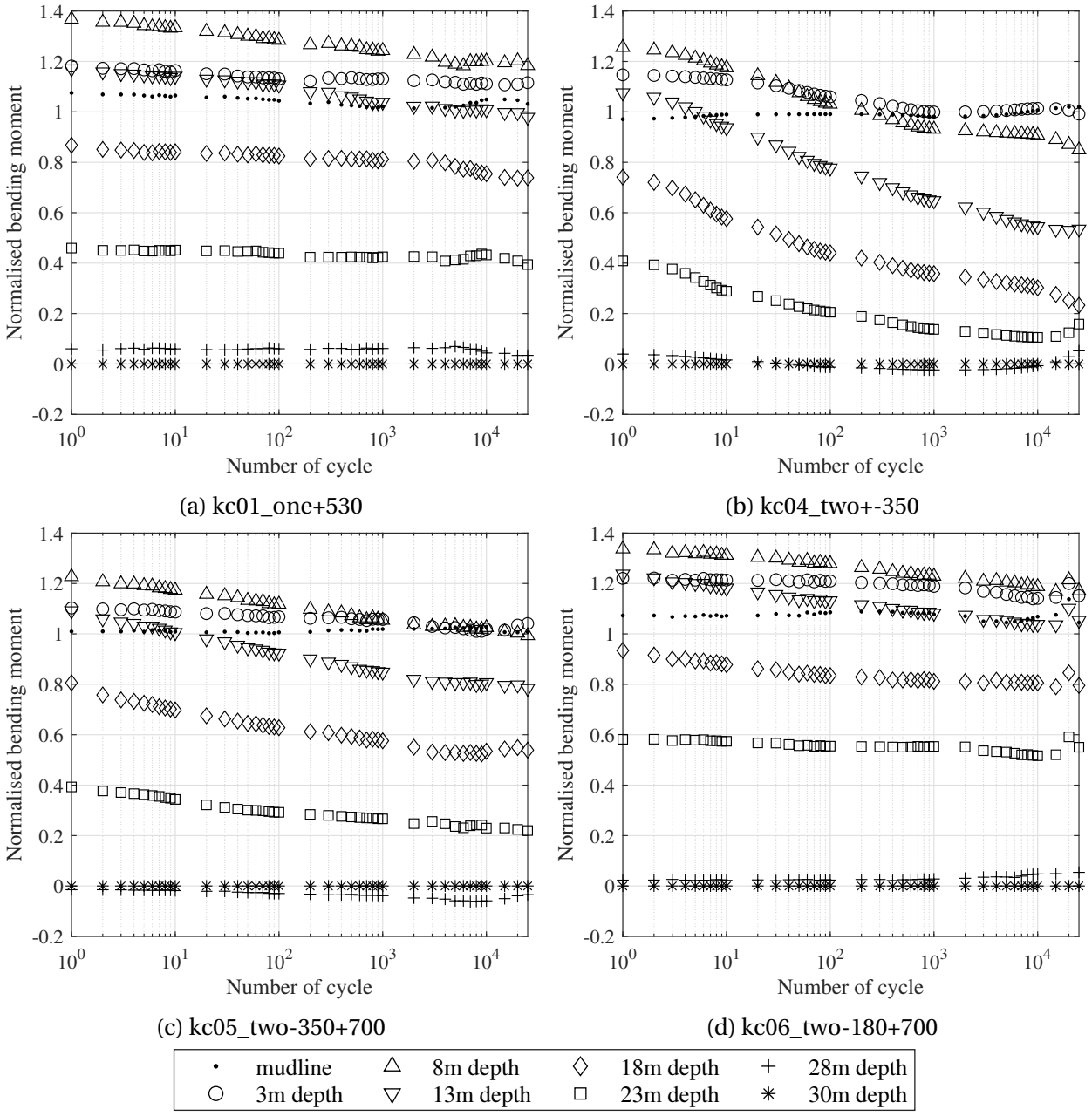
(d) kc06_two-180+700

Figure 5.16: Max normalised BM against cycles

For one-way tests, there was only a small variation of the normalised maximum bending moment profile over 20000 cycles at all depths. This can be seen from Figure 5.16a, where the normalised bending moment profile along the pile for different cycle number is shown and Fig-

ure 5.17a, where normalised maximum bending moment against the cycle number at different depths is plotted. The normalised bending moment at all depths decreased by less than 0.2 for kc01 (see Figure 5.17a). Similarly, the normalised maximum bending moments of two-way tests also follow a decreasing trend but with a larger magnitude of reduction, as can be seen from Figure 5.17b. Over 20000 cycles, the moments at 13m depth, where the largest moment change occurs, for kc04 decreased from 1.1 to 0.5. The bending moments at the same depth for kc05 and kc06 reduced by 0.3 and 0.2 respectively (see Figure 5.17c and 5.17d).

The bending moment at zero force is commonly referred to as the 'locked-in' bending moment. This locked-in moment gradually increases with cycle number at all depths for one-way tests, see Figure 5.18a. The largest increase in the moment was 0.44 for kc01, 0.56 for kc02, 0.45 for kc03 and 0.52 for kc08, respectively, and occurred at 18m depth for all four one-way tests. For the highly biased two-way test (kc06), this locked-in moment also has a growing trend, as shown in Figure 5.18d. For symmetric two-way tests (kc04 and kc07), the locked-in moment emerged in the first cycle and then dissipated to less than 0.1 at higher cycle numbers, see Figure 5.18b. In terms of kc05 (low bias, two-way loading), the locked-in moments remain relatively stable with cycles, see Figure 5.18c. This suggests that there is a transition stage from a growing locked-in moment to a dissipating locked-in moment, which is dependent on the cyclic ratio.



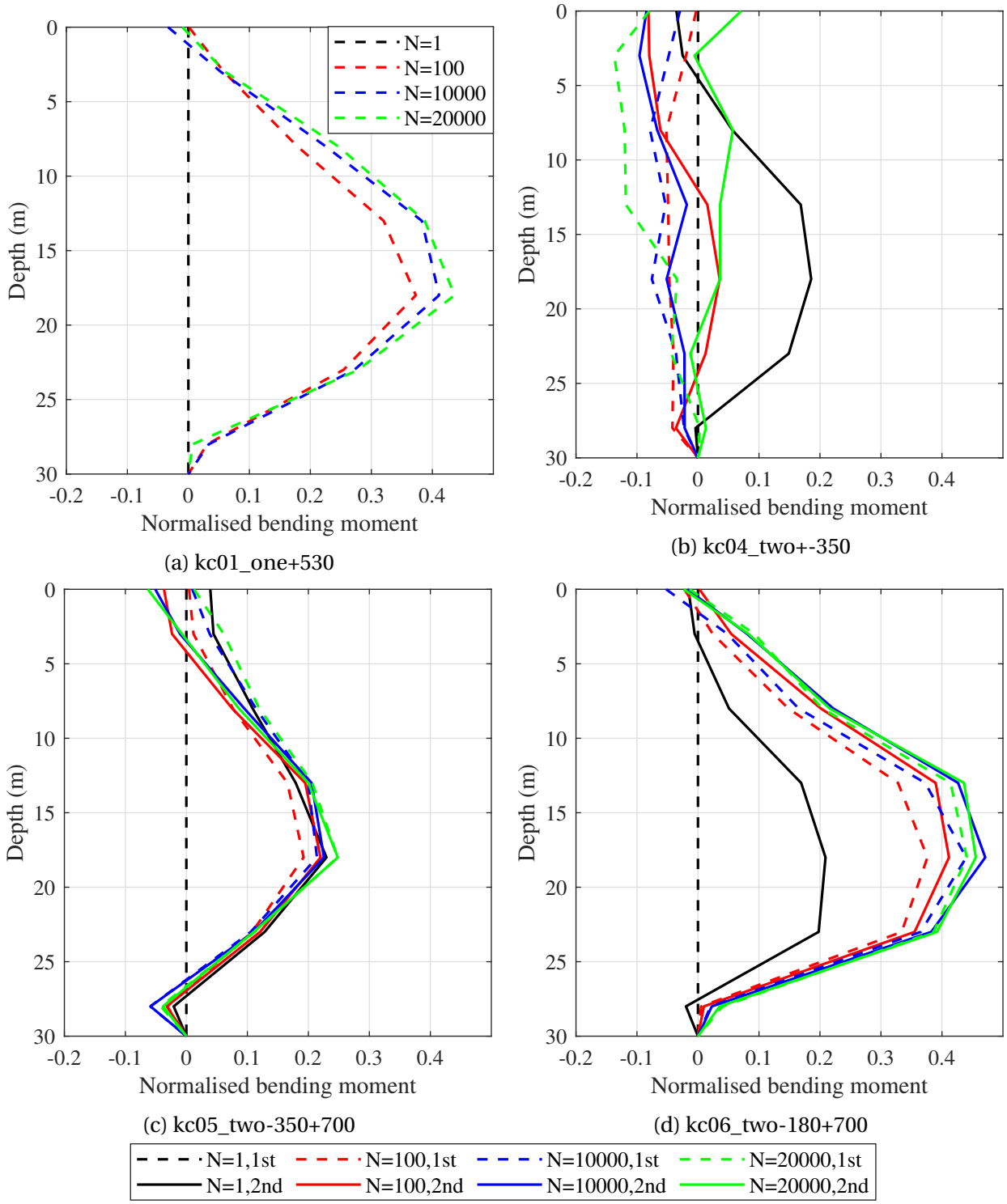
(a) kc01_one+530

(b) kc04_two+-350

(c) kc05_two-350+700

(d) kc06_two-180+700

Figure 5.17: Normalised max BM against cycles



(a) kc01_one+530

(b) kc04_two+-350

(c) kc05_two-350+700

(d) kc06_two-180+700

(e) legend for kc04, kc05, and kc06

Figure 5.18: Zero load BM against cycles

Figure 5.19 shows the normalised maximum bending moment versus the number of cycles at 8m depth. A depth of 8m has been chosen at that is where the largest moment developed for all tests. To provide a better understanding of the impact of cyclic loading ratio and cyclic magnitude ratio on the reduction in normalised maximum bending moment, the slope of the reduction can be extracted (as shown with the best-fit lines). These slopes can then be plotted against the cyclic loading ratio (ζ_c) and cyclic magnitude ratio (ζ_b), as shown in Figure 5.20, where the size of the marker circle denotes the slope of the bending moment decrease - i.e. a larger marker circle indicates a higher rate of reduction of bending moment with cycle number. It is evident that the moment changes for one-way tests (high ζ_c) is less than that for two-way tests (low ζ_c). Moreover, the change in bending moment is negatively related to the cyclic ratio, in which a lower cyclic ratio (ζ_c) leads to a larger reduction in the normalised bending moment. This correlation is evident from the four two-way tests. However, test kc06 with $\zeta_c = -0.26$ is similar to one-way tests with $\zeta_c = 0$ in terms of the moment reduction, as shown in Figure 5.19. It seems that two-way tests with a larger cyclic ratio tend to behave like one-way tests and have a smaller reduction in the maximum bending moment (see Figure 5.20) as well as a gradual accumulation of locked-in bending moment at zero force (see Figure 5.18). On the other hand, a higher cyclic loading ratio causes a smaller reduction rate (compare kc04 and kc07). However, this is not true for one-way tests (kc02, kc03 and kc08). There is however no discernible trend between the cyclic loading ratio and rate of change in bending moment.

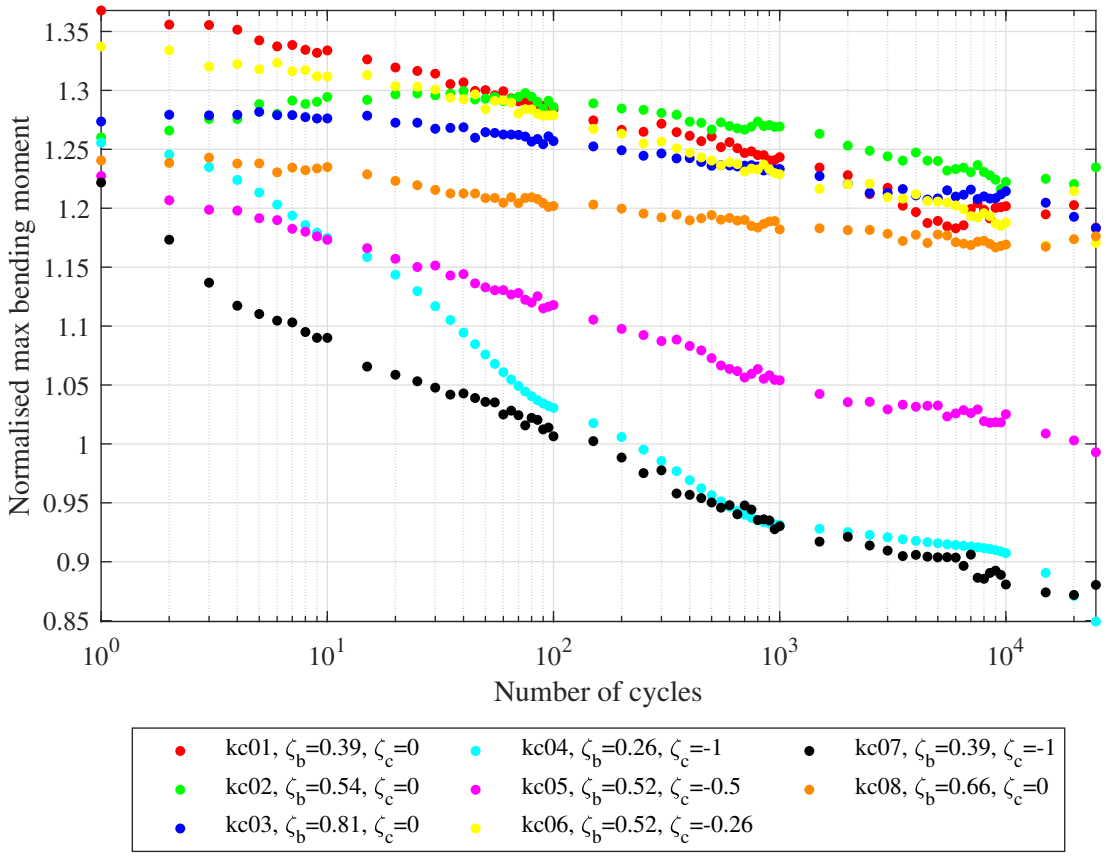


Figure 5.19: Maximum bending moment at 8m depth

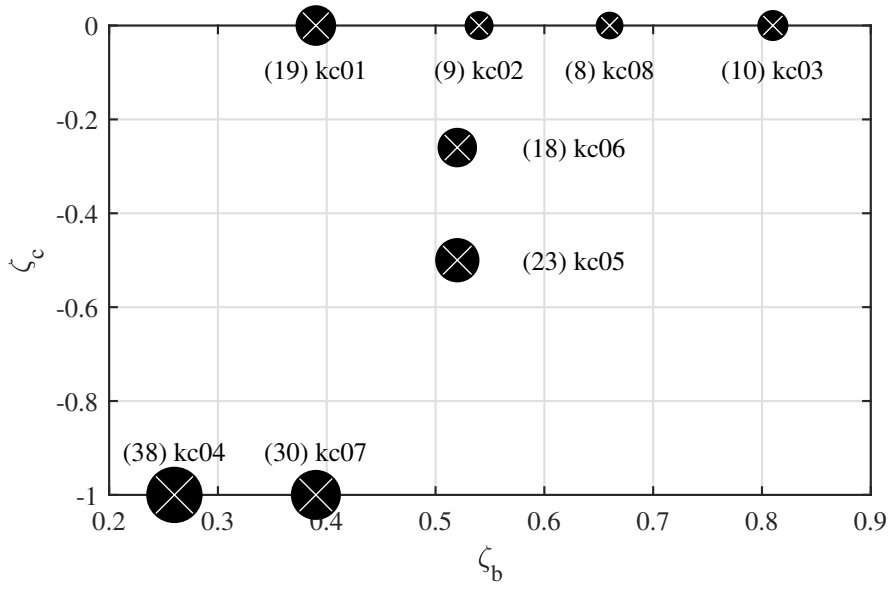


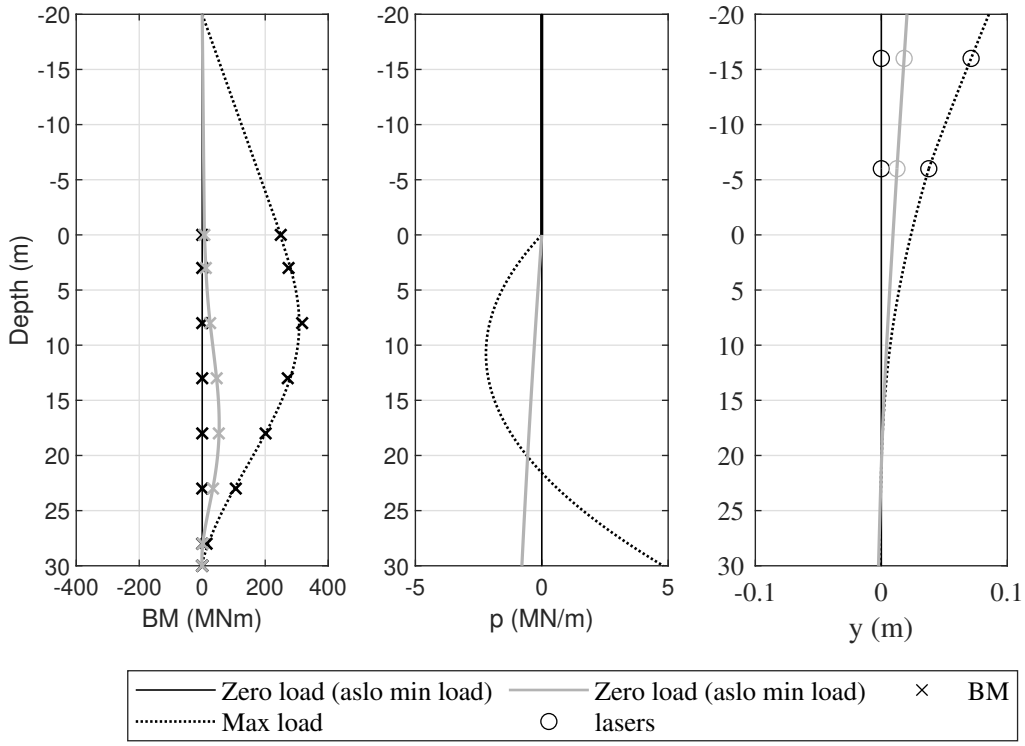
Figure 5.20: Maximum bending moment slope at 8m depth (slope shown in brackets)

5.5 Soil behaviour and pile displacement during cyclic tests

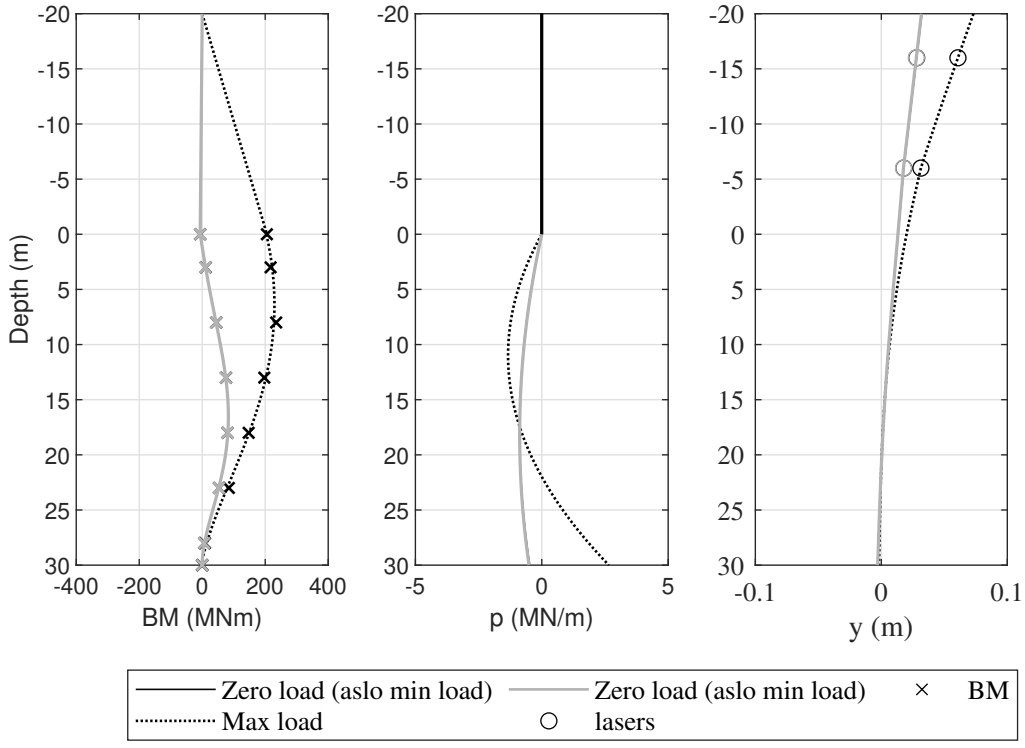
Soil reactions and pile displacements along the pile for cyclic tests are derived from the bending moment profile. The method used is identical to that in the monotonic test, where bending moments are first fitted with a fourth-order polynomial function, from which double differentiation gives soil reactions and double integration gives pile displacement profile. The obtained soil reactions (p) and pile displacements (y) as well as the fitted line of bending moments (BM) for three tests at two representative cycles (N=1 and 10000) are presented in Figure 5.21, 5.22 and 5.23 (Dark lines indicating loading and grey lines indicating unloading).

For the first cycle of kc01, as can be seen from Figure 5.21a, the bending moment fitted lines provide a reasonable fit to the bending moment profile. The fitting lines for other tests at different cycles are also sensible in the following figures. In terms of soil reaction, the soil reaction developed from zero during loading, and then dissipates as unloading along the pile. The soil reaction did not fully dissipate as the force dropped to zero (also minimum load), leaving a 'locked-in' stress along the pile. Although the actual value of this locked-in stress is unknown, its existence is supported by the presence of the locked-in bending moment at near zero force. This stress is also found in other literature and is believed to have a positive effect on soil-pile system stability (Suzuki et al., 2018). The zero soil reaction depth for the first cycle is varying between 20m and 24m, which is a reasonable depth range for the rotation point (Chortis et al., 2020). With respect to pile displacement, the pile curved to the loading direction and then returned partially to a position with a residual displacement at the end of the first cycle. In terms of the other one-way tests, identical patterns were found for kc02, kc03, and kc08 as kc01, both at the first and the other cycles.

For the first cycle of symmetric two-way loading tests, kc07 displays a highly symmetric development of soil reaction and pile displacement for all the cycles, as shown in Figure 5.23. On the other hand, for test kc06 which has a load bias, the soil reaction and pile displacement development with cycles is not symmetric (see Figure 5.22). Although the soil reaction at the end of the first cycle and the 10000th cycle (grey line, min load) may not be entirely accurate due to the differentiation process, there is a build-up of soil reaction in the reverse loading direction for both kc06 (see Figure 5.22) and kc07 (see Figure 5.23). In addition, a 'locked-in' stress along the pile was observed at zero load (unloading, grey lines) for kc06 at the first and 10,000th cycle. In contrast, the 'locked-in' stress dissipated at unloading zero load for kc07 at 10,000th cycle (see Figure 5.23b), in corresponding to bending moments at zero load (unloading, see Figure 5.18b). For displacement, similar to one-way tests, kc06 moved only in the dominant force direction (see Figure 5.22).

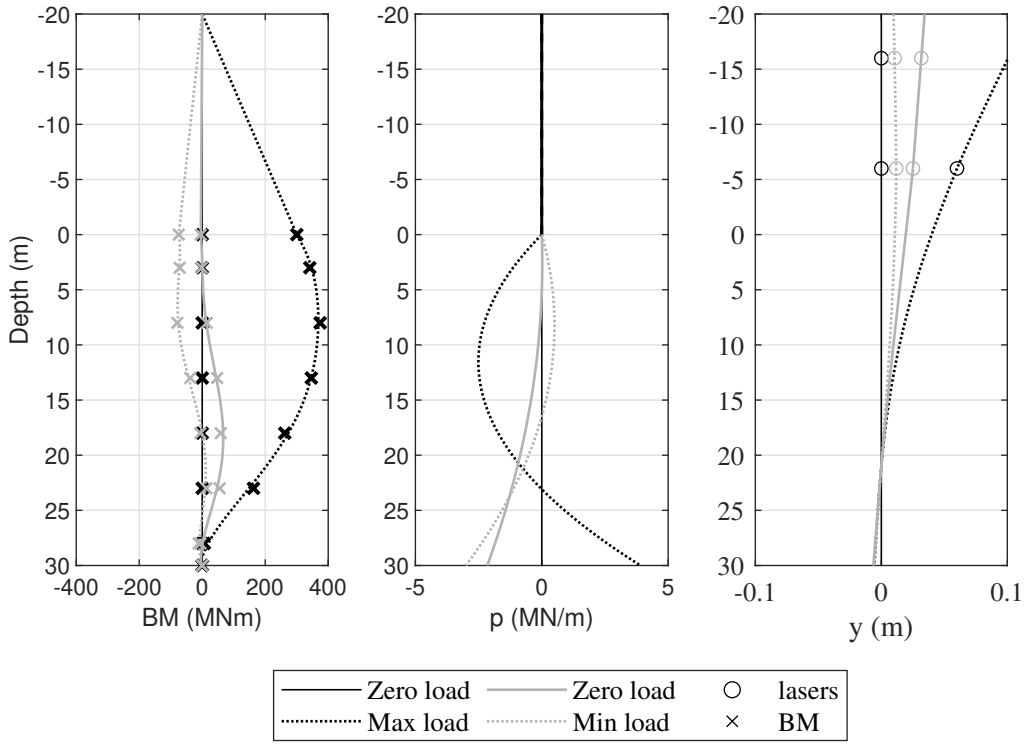


(a) N=1

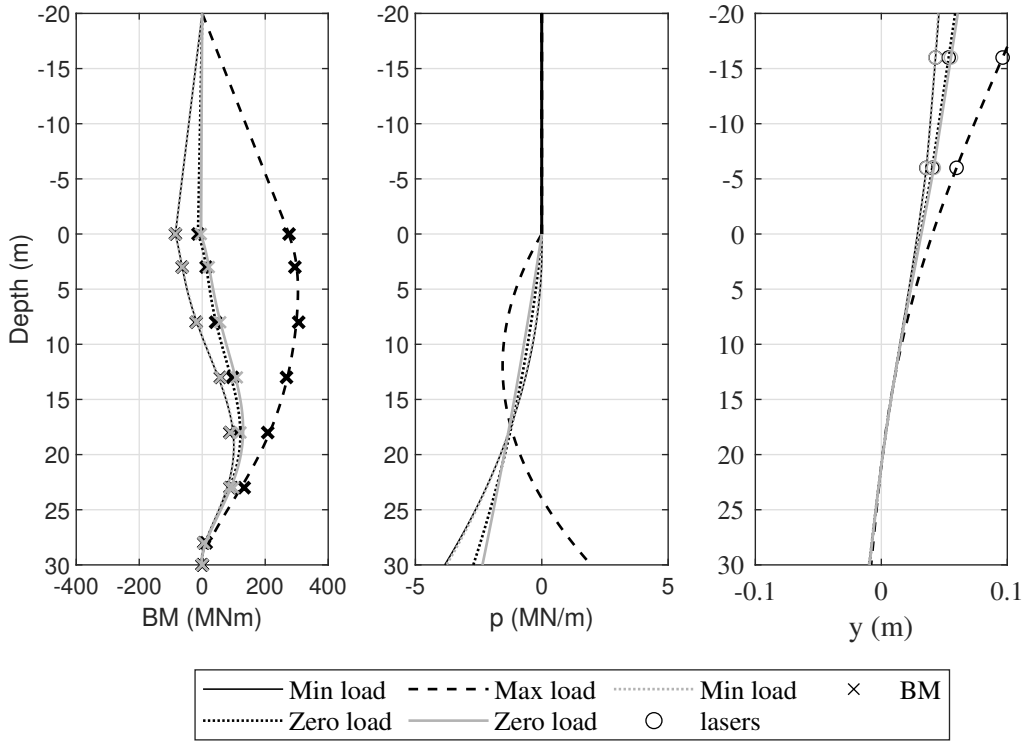


(b) N=10000

Figure 5.21: Soil reaction and pile displacement: kc01_one+530 ($H_{\min} = 0, H_{\max} = 530$N)

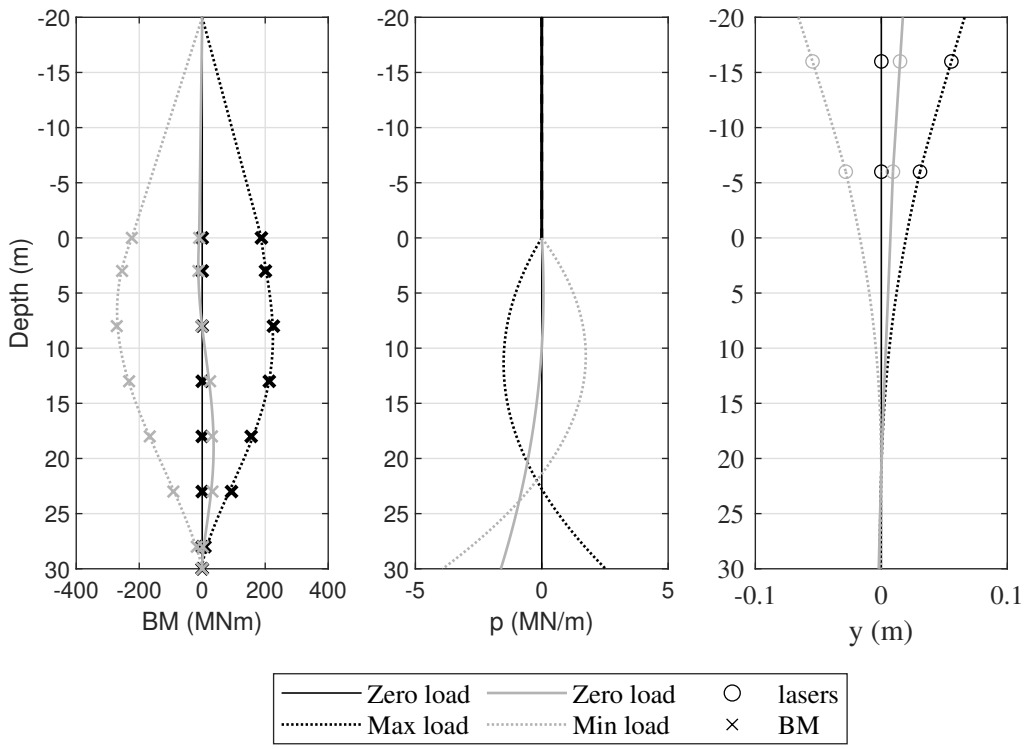


(a) N=1

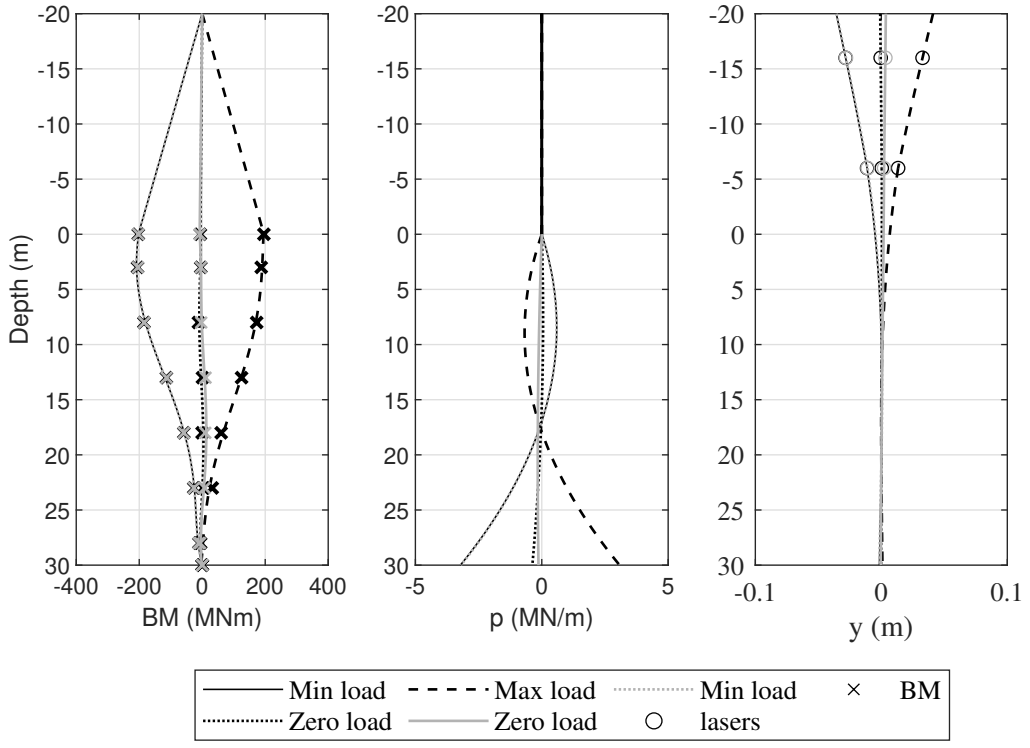


(b) N=10000

Figure 5.22: Soil reaction and pile displacement: kc06_two-180+700 ($H_{\min} = -180$N, $H_{\max} = 700$N)



(a) N=1



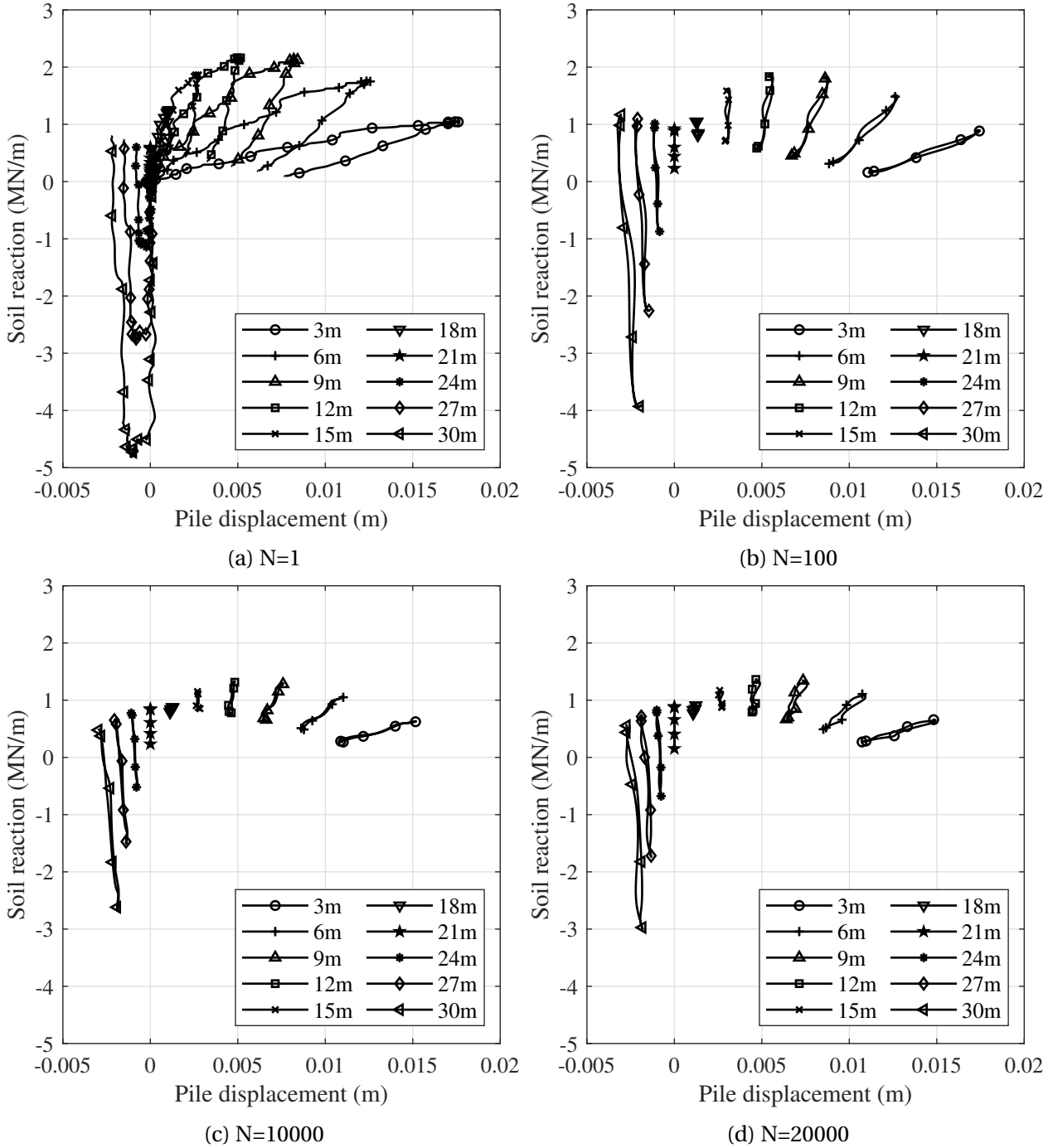
(b) N=10000

Figure 5.23: Soil reaction and pile displacement: kc07_two+-525 ($H_{\min} = -525$N, $H_{\max} = 525$N)

5.6 Cyclic p-y curve

Cyclic p-y curves for tests can be plotted based on the calculated soil reaction and pile displacement. Given the issues with accuracy of the calculated soil reactions and pile displacements, the p-y curves herein, in terms of quantitative evaluation, are discussed with a level of caution; more focus is placed on the observed trends of cyclic p-y curves in terms of large cycles and across different tests.

Figure 5.24 shows the cyclic p-y curves of different depths at four cycles (1, 100, 10000, and 20000) for kc01. It can be seen that the curves are reasonable compared to the monotonic p-y curve (see Figure 4.10) at shallow depths (less than 15m) at the first cycle. At greater depth, the curve became extremely steep at all four cycles, indicating a stiffer soil response. While it is true that p-y curves become steeper at deeper depths, such steep curves in Figure 5.24 are likely caused by the inaccurate soil reaction and pile displacement as a small variation of these values can significantly affect the p-y curves. As a result, p-y curves at deep depths are not discussed in this study, and curves at a shallow depth (9m) are selected to understand the effects of cycles and loading characteristics.



(a) N=1

(b) N=100

(c) N=10000

(d) N=20000

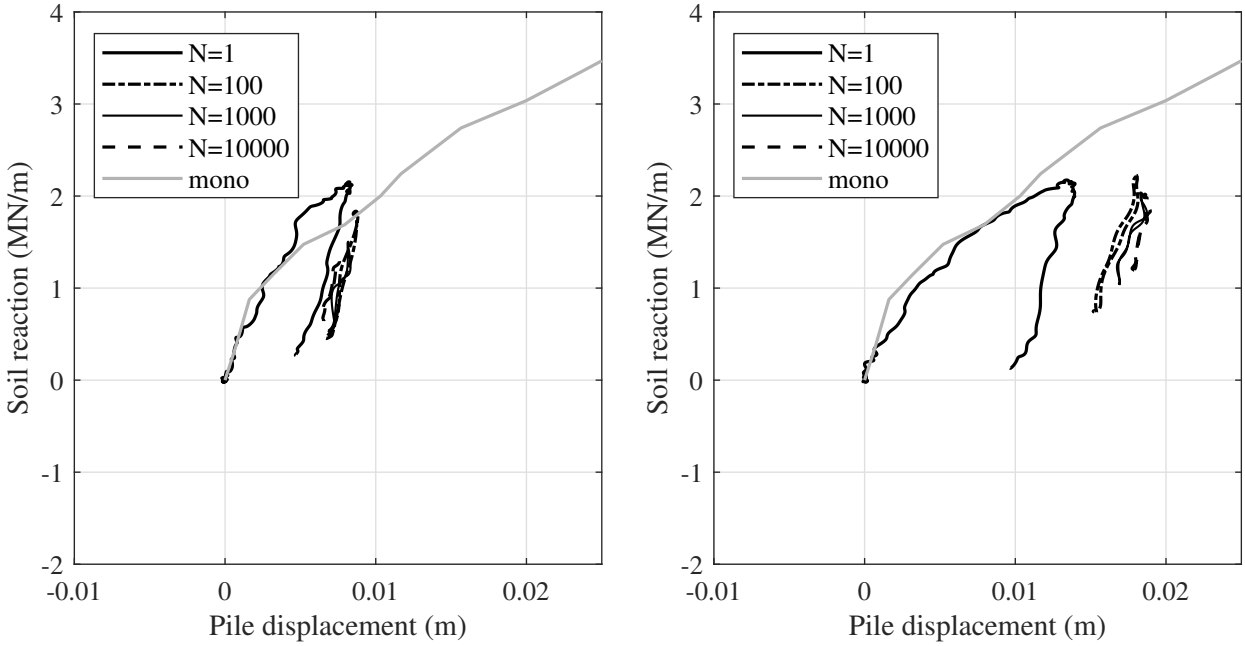
Figure 5.24: p-y cyclic curve: kc01_one+530 ($H_{\min} = 0, H_{\max} = 530$N)

To demonstrate the effects of cycles and loading characteristics on the p-y curves, p-y curves for each test at 9m depth are presented separately in Figure 5.25 and 5.26. In addition, the monotonic p-y curve is added to these figures to provide a reference. From these figures, the most striking variation of the p-y curves for all tests is the reduction of the areas enclosed by the loading and unloading curve, indicating a transition from a system dominated by plastic soil response to one characterised by elastic behaviour. Moreover, the slope of the curves increased with cycle number, indicating the stiffness of the soil-pile system increased, resulting in the increasing secant stiffness previously observed (see Figure 5.9).

For one-way tests, the p-y curves at the first cycle are reasonably close to the monotonic p-y curve given the errors associated with the mathematical operations. It can be seen that at the end of the first cycle, the p-y curve does not return to zero, and locked-in stresses and displacements are observed, corresponding to Figure 5.21a. The soil reaction and displacement at end of each cycle accumulate with cycle number for kc02, kc03 and kc08, whereas for kc01 they increased until the 1000th cycle and then dropped at the 10000th cycle. This reduction of soil reaction and displacement in the kc01 test is due to the loading change, as the force applied on the pile reached 600N and decreased to 500N at the 1000th cycle. The reduced loads on the pile cause the locked-in stress and displacement to dissipate. The locked-in displacement is related to the minimum displacement, thus explaining why the minimum pile head displacement for kc01 reached a relatively lower plateau after 1000 cycles compared to other one-way tests (see Figure 5.7). In terms of the top point of the p-y curve at each cycle, the pile displacement accumulated and then levelled off in all tests except kc01 (for the same reason mentioned above), which is in-line with the observation of maximum pile head displacement (see Figure 5.6). In contrast, the soil reaction of the top point decreased with cycle number; this declining soil re-

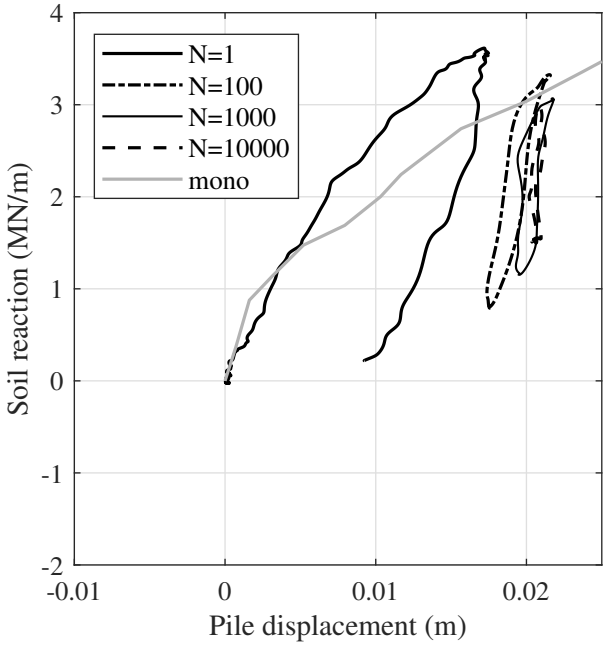
action means a smaller mobilised soil reaction, which is the result of a stiffer pile-soil system with a constant applied load. The stiffening pile-soil system is caused by soil densification with load cycles, which is also in agreement with the increasing secant stiffness (see Section 5.3). The soil-pile system became stiffer with cycle number, as the slope of p-y curves increases, while the force on the pile was constant; the mobilised soil reaction therefore decreases. This phenomenon is pronounced for kc01, as the force in this test reduced to a relatively large extent and the reduction in soil reaction is also large.

For two-way tests, p-y curves of biased two-way tests (kc05 and kc06) are similar to one-way tests with an accumulating pile displacement of the endpoint and increasing slope, which are corresponding to their pile head displacement and secant stiffness developments (see Figure 5.7 and 5.9). The soil reaction of the top points in these p-y curves also declined over cycle number, similar to the one-way tests. However, the pile displacement of these points shows a different trend, where in test kc05 there is a slightly decreasing trend and for kc06, the pile displacement at the top point fluctuated and then levelled off. These trends correspond to the maximum pile head displacement development, as shown in Figure 5.6. For the symmetric two-way test (kc04 and kc07), the pile displacement of the top points in kc07 decreased by a relatively large amount with cycle number, as illustrated by the maximum pile head displacement in Figure 5.6. It is noticed that the p-y curves of kc04 are significantly different from that of kc07. The errors for test kc04 is caused by the incorrect pile displacement profiles along the pile depth. Because of the low magnitude of cyclic load, the pile displacement is relatively small. As a result, the integration process did not generate reasonable pile displacements along the pile, leading to incorrect p-y curves. Therefore, p-y curves of kc04 are not discussed further.

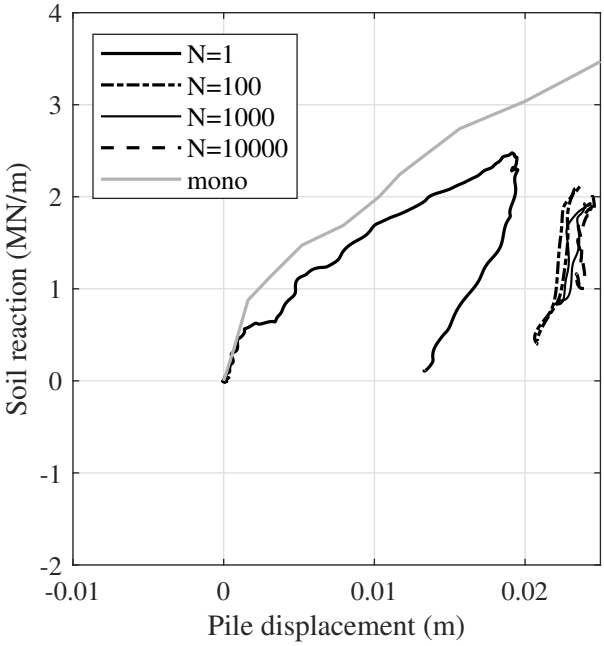


(a) kc01_one+530

(b) kc02_one+730

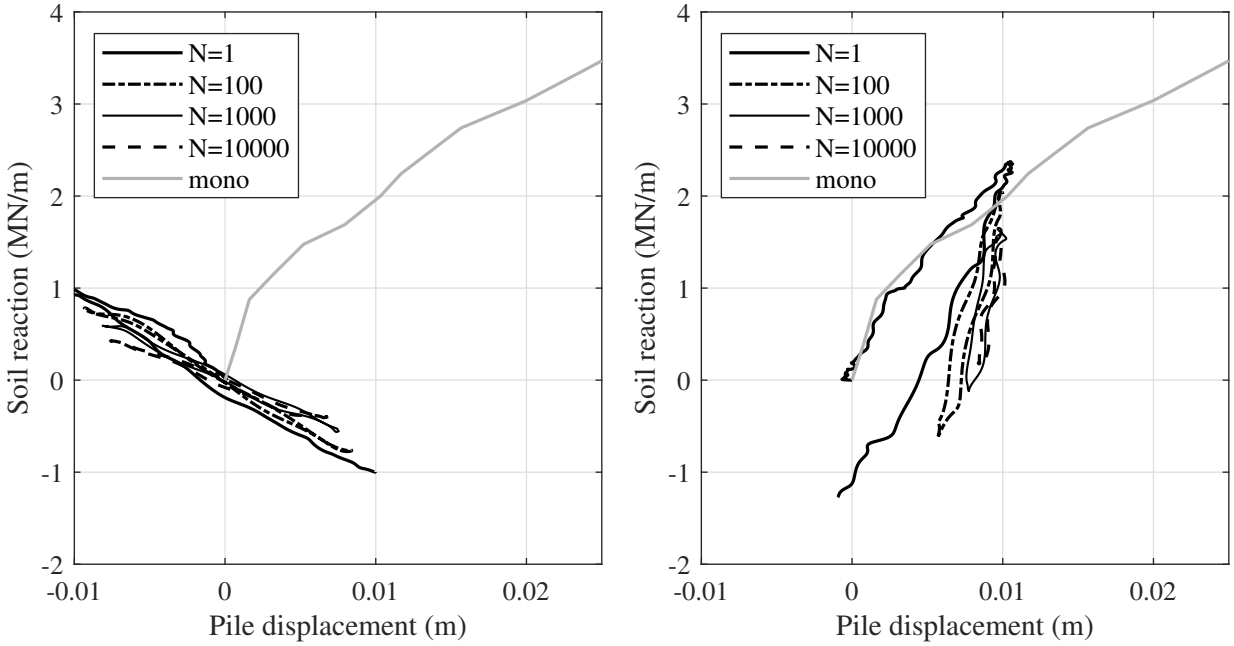


(c) kc03_one+1100



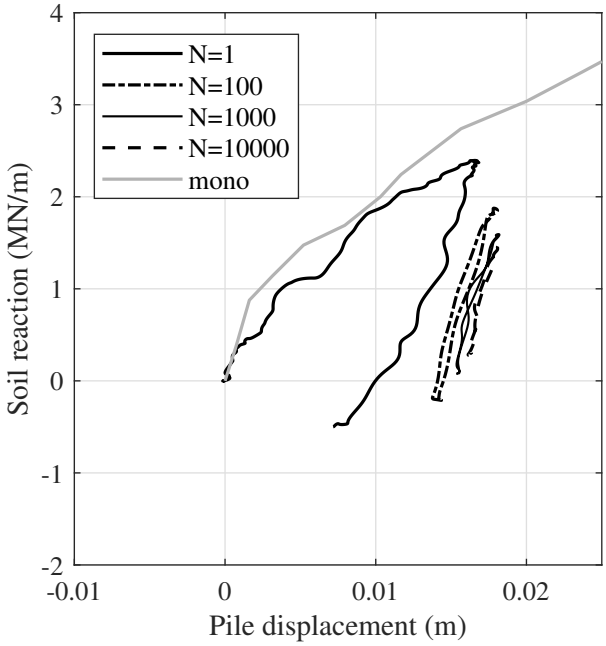
(d) kc08_one+890

Figure 5.25: p-y curves at 9m depth

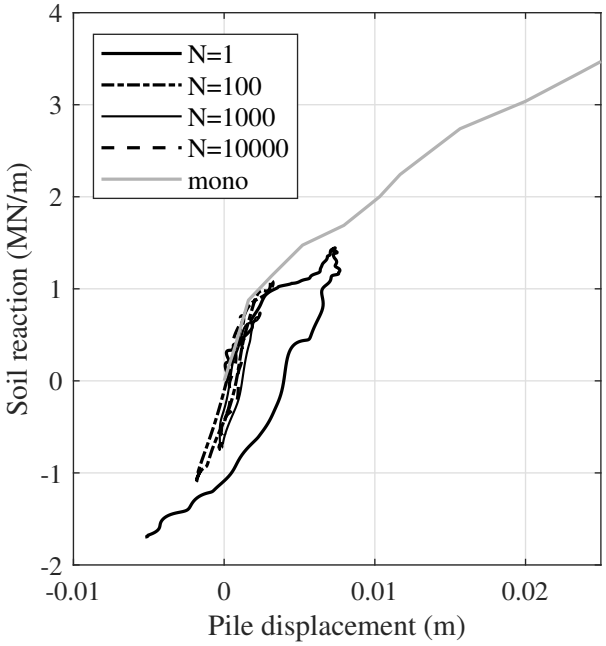


(a) kc04_two+-350

(b) kc05_two-350+700



(c) kc06_two-180+700



(d) kc07_two+-525

Figure 5.26: p-y curves at 9m depth (continued)

5.7 Summary

In this chapter, eight cyclic tests were investigated to demonstrate the long-term behaviour of piles under cyclic loading including pile head displacement, secant stiffness, soil reaction, pile displacement along the pile depth, and cyclic p-y curves as well as the effects of loading characteristics on them.

The pile displacement was found to increase with cycle number and then stabilise after around 10^4 cycles in this study. Maximum pile head displacement for each cycle is positively related to both cyclic magnitude ratio and cyclic ratio (see equations 2.40 and 2.41), i.e., a larger load on the pile causes a greater displacement, and loading characteristics inclined to a one-way loading scenario lead to increased displacement.

Similar to pile head displacement, secant stiffness for tests also increased with cycle number and then eventually levelled off. A new empirical equation was proposed to capture the trend of secant stiffness with cycle number. It was also found that the cyclic magnitude ratio and cyclic ratio have a positive effect on secant stiffness.

The maximum bending moments of tests were observed to decrease with cycle number. In addition, the cyclic loading ratio negatively affects the magnitude of this reduction. The maximum bending moment of the reversed direction in two-way tests also shows a decreasing trend. The bending moments at zero force of one-way tests during cycles were not zero; in other words, there was a locked-in moment. It was seen that the locked-in moments accumulated for one-way tests and biased two-way tests, but dissipated for symmetric two-way tests.

In terms of soil reactions and pile displacements along the pile depth, locked-in soil reactions and pile displacements were observed after each cycle. Cyclic p-y curves were obtained

based on the calculated soil reactions and pile displacements. The overall slope of p-y curves increased with cycles, suggesting a stiffening response. In addition, the area enclosed by a p-y curve shrank with cycle number, indicating a shift from soil behaviour dominated by plastic response towards a more elastic response.

Chapter 6

Practical implications

6.1 Implications for the design

The design and performance of pile foundations in offshore wind turbines (OWTs) are critically influenced by several factors, including pile head displacement, rotation, bending moment, and stiffness of the pile-soil system. These factors directly affect the structural integrity, safety, and long-term stability of OWT foundations under dynamic offshore conditions. The findings of this study regarding pile head displacement, bending moment and the stiffness of pile-soil system offers practical insights that can be adopted to facilitate the design of OWT foundations.

6.2 Pile head displacement

Pile head displacement and rotation are important considerations in the design of offshore wind turbines. The serviceability limit state suggests that the maximum pile head rotation should be less than 0.5 degree during the lifespan of the OWTs. Figure 6.1 shows the maximum pile rota-

tion against number of cycles for all cyclic tests, which is calculated by the inverse tangent of the maximum pile head displacement divided by the load eccentricity (200mm). As with pile head displacement, the pile rotation of one-way tests proved to be larger than that of two-way tests. This demonstrates that the one-way loading is the critical scenario that requires more attention during the design of foundations. Engineers should pay attention to one-way loading and prepare foundations for extreme one-way loading conditions. Regarding long-term behaviour, the pile rotation increases with cycles at the beginning and then reaches a plateau after about 10,000 cycles irrespective of loading characteristics. This finding is significant. The OWTs have to undergo 10^7 cycles during their lifespan, while it is challenging to apply such a large number of cycles for both experimental and numerical tests. The observation that pile head displacement and rotation stabilize after 10,000 cycles provides a practical method for predicting their maximum values. The tendency of pile head displacement and rotation makes it possible to work out the ultimate pile head displacement and rotation, either by experimental tests or numerical simulation applying 10,000 cycles. This will greatly simplify the design of offshore wind turbine foundations while ensuring compliance with with serviceability limit state.

6.3 Bending moment

Bending moment is another crucial factor in the safety of pile foundations. In this study, the bending moment decreased with the number of cycles for both one-way and two-way cyclic tests, suggesting that the maximum bending moment occurs at the onset of cyclic loading. Designers must ensure that the maximum bending moment remains within a safe range to maintain structural integrity. Additionally, the reduction in bending moments is more significant for

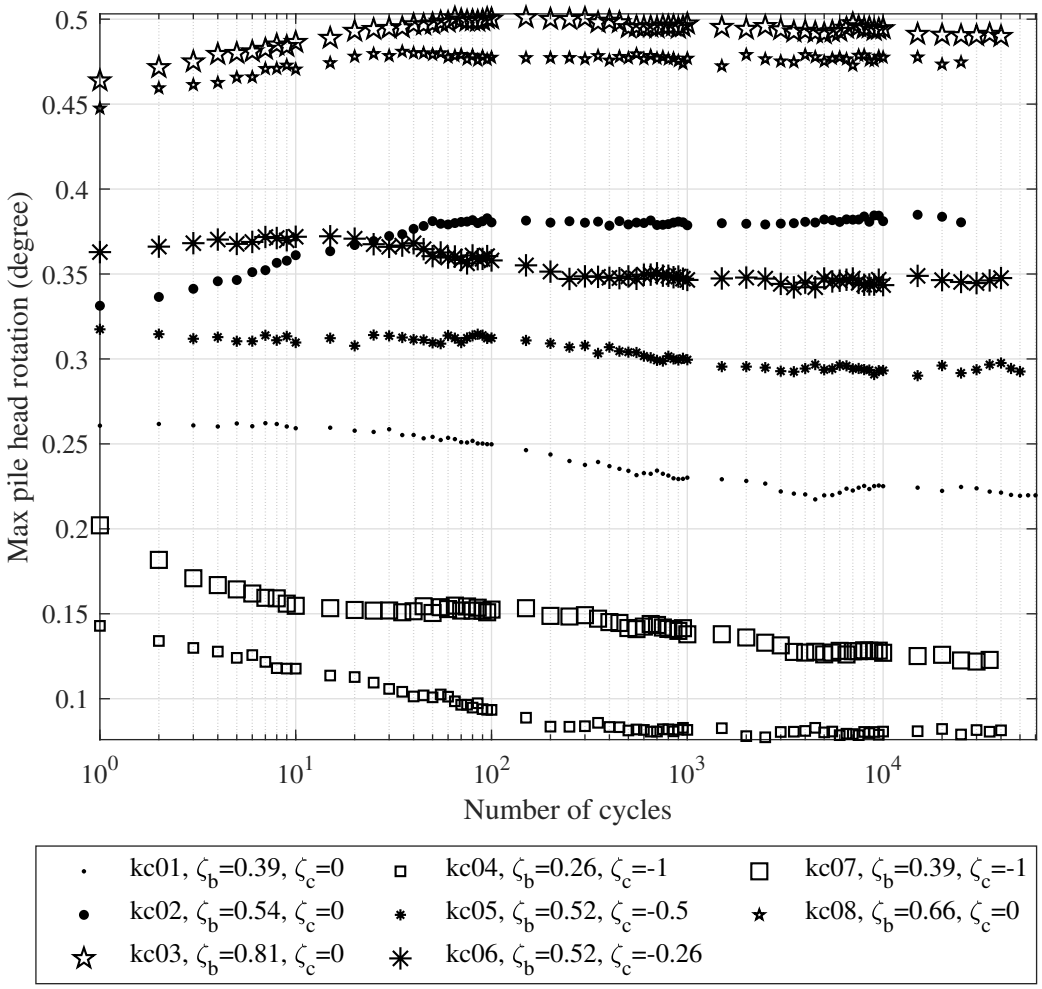


Figure 6.1: Pile head rotation

two-way tests than for one-way tests, as shown in Figure 5.20. This indicates that one-way tests are more critical when considering bending moment effects.

6.4 Stiffness of the pile-soil system

The stiffness of the pile-soil system is directly linked to its natural frequency, which plays a crucial role in the structural performance of offshore wind turbines (OWTs). Ensuring that the natural frequency remains within the soft-stiff range is essential to avoid resonance and potential structural failures. However, the stiffness of the pile-soil system is not static; it evolves over time

due to cyclic loading. Therefore, understanding how stiffness changes throughout the lifespan of OWTs is critical for designing foundations that maintain long-term stability.

This study found that the stiffness initially increased with the number of loading cycles, regardless of the specific loading characteristics. This increase was primarily attributed to the densification of soil around the pile as cyclic loading progressed. As the soil particles rearranged and compacted under repeated loading, the pile-soil interaction strengthened, leading to a stiffer response. This behaviour was further supported by the observation of progressively stiffer p-y curves over successive cycles. After approximately 10,000 cycles, the stiffness reached a plateau, suggesting that the densification process had stabilized and further changes in stiffness became minimal. Additionally, the final stiffness was found to be positively correlated with the cyclic magnitude ratio, meaning that higher cyclic loads resulted in greater overall stiffness. This implies that different loading scenarios lead to varying final stiffness values, which must be accounted for in design considerations.

These findings provide valuable data of stiffness evolution over cycles. Based on the trend of stiffness evolution, designers can estimate the final stiffness based on the stiffness after 10,000 cycles, which can be obtained by experimental or numerical tests. The loading characteristics of cyclic loads, particularly cyclic magnitude ratio, have an impact on the the development of stiffness. Designers have to understand the loading conditions to better predict final stiffness, hence ensuring that the natural frequency remains within a safe range.

Chapter 7

Conclusions

7.1 Introduction

Monopile foundations, which are widely adopted to support offshore wind turbines, are subjected to a large number of cyclic loads originating from the effects of wind and waves. To ensure the safety of such structures, it is necessary to understand the behaviour of monopiles under cyclic loading, especially after large numbers of cycles. While there have been a number of studies on this topic, the number of loading cycles are typically limited to the low thousands. In this study, centrifuge tests were carried out to apply cyclic loading with at least 20,000 cycles to investigate the long-term behaviour of piles. In addition, cyclic loading with varying characteristics, i.e. different loading ratios and different loading magnitudes, were applied to examine their effect. Loading ratio relates to offset of the cyclic loading in terms of how much load is applied in the positive direction compared to the negative direction. An extreme case of loading ratio is that of one-way cyclic loading, where the force is applied in one direction only. More commonly loading is two-way in which the cyclic force acts both in the forwards and reserve di-

rections during each cycle. In reality, monopiles are subjected to a range of cyclic loading ratios and hence the important of investigating the impact of this parameter on the response of the compile. To apply cyclic loading, a novel loading system has been developed and was utilised in the centrifuge tests. During the centrifuge tests, the development of pile head displacement was recorded via lasers and the loading was logged through load cells. Furthermore, the pile had a prototype diameter of 6m, representing a typical pile required for a 5MW offshore wind turbine foundation. The pile was instrumented with Fibre Bragg sensors to obtain the bending moment profile, from which the soil reaction and pile displacement below sand surface can be derived. The examination of bending moment change was carried out, which can benefit the design of such foundations. This has also allowed the calculation and examination of cyclic p-y curves (which are used in the design of such foundations) with cycle number.

Prior to cyclic tests, monotonic tests were performed to obtain the load-displacement curve, also referred to as the backbone curve, and static p-y curve, both of which have provided a useful reference for cyclic tests. In addition, the static p-y curve has been compared with the API p-y curves, which is a widely adopted design guidance for offshore wind turbine foundations. The findings are summarised as follows.

7.2 Monotonic loading

Experimental p-y curves, extracted from a pushover test conducted in the centrifuge, were compared with API p-y curves. The comparison shows that API p-y curves over-predict the soil resistance, which is also supported by Kirkwood (2015) and Sørensen (2012). The reason for this discrepancy is mainly attributed to the fact that API p-y curves are derived for flexible piles with

a relative small diameter, whereas the majority of offshore wind turbine foundations have a large diameter and behave like rigid piles. As a result, API p-y curves should not be applied for the design of offshore wind turbine foundations.

7.3 Cyclic lateral loading

A programme of cyclic tests was carried out to investigate the long-term behaviour of a monopile under a range of cyclic loading, with a focus on the pile head displacement, pile secant stiffness, bending moment profile along the pile, and soil reaction.

Pile head displacement was observed to accumulate and then level off for one-way tests and to decrease and then stabilise for two-way tests in this study. This indicates the one-way loading scenario is more critical compared to two-way loading cases, which is in agreement with Klinkvort (2012). In terms of pile secant stiffness, it was found to increase and then stabilise for both one-way and two-way tests. In this study, at least 20,000 cycles were applied. The stiffness in the first 10,000 cycles indeed increased, but then showed signs of stabilisation. Thus, a hyperbolic model was proposed to capture the trend of pile stiffness development and proved to be a better fit. A close examination of the model suggests that the maximum stiffness is positively related to the cyclic magnitude ratio as well as the cyclic loading ratio. In other words, one-way tests will have a larger secant stiffness compared to two-way tests. Bending moments at different depths were observed to reduce over cycles by a small amount (less than 20%) for one-way tests. The change is comparatively larger for two-way tests, with a 50% reduction. It is concluded that the bending moment reduction is negatively associated with the cyclic loading ratio. In other words, symmetric two-way tests have a larger reduction in bending moments

than those in asymmetric two-way tests and one-way tests. Regarding soil response, cyclic p-y curves for different cycles were derived from experiments. The energy dissipated from the cyclic loading of the soils (as calculated from the enclosed area within the p-y curves) saw a reducing trend over cycles, suggesting a transformation from plastic behaviour to elastic behaviour. In addition, the slope of these p-y curves increased with cycles, indicating a stiffening of the soil-pile system.

7.4 Implication for design

The pile displacement of one-way tests proved to be larger than that of two-way tests, which gives engineers information to consider the one-way loading case to be the critical one. The tests were conducted under at least 20,000 cycles and the pile head displacement was shown to stabilise after approximately 10,000 cycles. This finding allows engineers to predict pile head displacement of offshore wind turbine throughout its lifespan based on pile head displacement after 10,000 cycles. Furthermore, a greater bending moment reduction compared to one-way tests was observed for two-way tests, which also suggests one-way tests is more critical in terms of bending moment consideration. In addition, the stiffness model provided in this study provide useful information for designers as there is a link between the stiffness and the natural frequency of the system. The stiffness model suggests the stiffness increases and reaches a plateau after about 10,000 cycles and the loading characteristics play a role on the final stiffness value. Designers can use this finding to predict the final stiffness based on the loading conditions. The understanding of stiffness development can help to ensure that the natural frequency of the system lies in safe zone, hence benefiting the long-term stability of OWT foundations in dy-

namic offshore conditions. For soil response, the p-y curves from API cannot predict the real p-y curves, as observed by a number of researchers. Although there is no proposed model for p-y curves in this study, the tests conducted provide valuable data concerning p-y curves for both monotonic and cyclic tests. These data can be used to develop a better model.

7.5 Recommendation for future research

This study has provided valuable information about long-term behaviour of monopiles under cyclic loading, with a focus on pile head displacement, pile secant stiffness and bending moment development over a large number of cycles. However, there are some limitations to this study and further research is needed.

1. As many research, this research applied the load in a uni-direction manner. Whereas, real offshore foundations are subjected to loads from varying directions. The effect of changing loading directions is an important aspect to be investigated in future research.

2. The tests conducted in this study were based on a specific dimension of pile. It is necessary to investigate the response of piles with varying dimensions. The relative density of the soil is likely to have an impact on the pile behaviour. Further tests of piles in soils with different relative densities can be beneficial for the understanding of this topic.

3. This study has applied at least 20000 cycles, more than many other similar research. However, the number of cycles that a typical offshore wind turbine foundation experiences during its lifespan is estimated to be more than 10^7 cycles. Since the applied load cycle is still extremely smaller than it, there is a possibility that the behaviour can change after a

large number of cycles (e.g. 10^6 cycles). It is therefore worthy of effort to further increase the number of applied load cycles to observe the long-term trend of pile head displacement development.

4. The original aim of this study included a development of an empirical p-y curve evolution model with load cycles. However, this aim was aborted during the study. This is because the calculation of cyclic p-y curves are susceptible to the error of calculated soil reaction and pile displacements. In this study, the limited number of FBGs can not produce sufficiently precise soil reaction to accurately represent cyclic p-y curves. It may be beneficial to install more FBGs to enhance the accuracy of soil reaction profile. Hence, cyclic p-y curves over cycles can be generated and analysed quantitatively.

References

Achmus, M. and Abdel-Rahman, K. (2005). Finite element modelling of horizontally loaded monopile foundations for offshore wind energy converters in Germany. *International symposium on frontiers in Offshore Geotechnics*, pages 391–396.

Achmus, M., Kuo, Y. S., and Abdel-Rahman, K. (2009). Behavior of monopile foundations under cyclic lateral load. *Computers and Geotechnics*, 36(5):725–735.

API (2011). Recommended Practice for Planning , Designing and Constructing Fixed Offshore Platforms — Working Stress Design. *Api Recommended Practice*, 24-WSD(2011):242.

Arshad, M. and O'Kelly, B. (2013). Offshore wind-turbine structures : a review. 166:139–152.

Bhattacharya, S., Cox, J. A., Lombardi, D., and Muir Wood, D. (2013). Dynamics of offshore wind turbines supported on two foundations. *Proceedings of the Institution of Civil Engineers - Geotechnical Engineering*, 166(2):159–169.

Broms, B. (1964). Lateral resistance of piles in cohesionless soils. *Journal of Soil Mechanics and Foundations Division*, 90(3):123–156.

Burd, H. J., Taborda, D. M. G., Zdravković, L., Abadie, C. N., Byrne, B. W., Houlsby, G. T., Gavin, K. G., Igoe, D. J. P., Jardine, R. J., Martin, C. M., McAdam, R. A., Pedro, A. M. G., and Potts, D. M.

(2020). Pisa design model for monopiles for offshore wind turbines: application to a marine sand. *Géotechnique*, 70(11):1048–1066.

Cha, W., Park, J., and Santamarina, J. (2023). Long-term response of sand subjected to repetitive simple shear loading: Shakedown, ratcheting and terminal void ratio. *Journal of Geotechnical and Geoenvironmental Engineering*, 149:04023028.

Chortis, G., Askarinejad, A., Prendergast, L. J., Li, Q., and Gavin, K. (2020). Influence of scour depth and type on p–y curves for monopiles in sand under monotonic lateral loading in a geotechnical centrifuge. *Ocean Engineering*, 197.

Cox, W., Reese, L., and Grubbs, B. R. (1974). Field Testing of Laterally Loaded Piles In Sand. *Proc. Offshore Technology Conference*, pages 459–472.

Craig, W. H. (1985). Installation studies for model piles. *Proc. Application of centrifuge modelling to geotechnical design*, pages 441–456.

Cuéllar, P. (2011). Pile Foundations for Offshore Wind Turbines : Numerical and Experimental Investigations on the Behaviour under Short- Term and Long-Term Cyclic Loading. page 257.

DNV (2016). DNVGL-ST-0126 : Support structures for wind turbines. *Dnv Gl As*.

DNV GL (2016). DNVGL-ST-0437 Loads and site conditions for wind turbines.

Doherty, P. and Gavin, K. (2012). Laterally loaded monopile design for offshore wind farms. *Proceedings of the Institution of Civil Engineers - Energy*, 165(1):7–17.

Ellis, E., Cox, C., Yu, H., Ainsworth, A., and Baker, N. (2006). A new geotechnical centrifuge

at the university of nottingham, uk. *6th International Conference of Physical Modelling in Geotechnics*, 6:129–133.

Elvis, J. E. (2018). *Centrifuge and analytical modelling of offshore wind turbine monopile foundation*. PhD thesis, The University of Nottingham.

EWEA (2014). The European offshore wind industry - key trends and statistics 2013. *A report by the European Wind Energy Association*.

Haiderali, A. E. and Madabhushi, G. (2016). Evaluation of curve fitting techniques in deriving p–y curves for laterally loaded piles. *Geotechnical and Geological Engineering*, 34:1453–1473.

Hansen, J. B. (1961). *The ultimate resistance of rigid piles against transversal forces*. Akademiet for de tekniske Videnskaber. Geoteknisk Institut. Bulletin.

Hetényi, M. (1946). *Beams on elastic foundation: theory with applications in the fields of civil and mechanical engineering*. University of Michigan studies: Scientific series. University of Michigan Press.

Ibsen, L. B., Hansen, M., Hjort, T., and Thaarup, M. (2009). MC-Parameter Calibration of sand No.15. *DCE Technical report No. 62*. Aalborg University.

Journée, J. M. J. and Massie, W. W. (2001). *Offshore Hydromechanics*. 1 edition. Delft University of Technology.

Katsanos, E. I., Sanz, A. A., Georgakis, C. T., and Thöns, S. (2017). Multi-hazard response analysis of a 5MW offshore wind turbine. *Procedia Engineering*, 199:3206–3211.

Kirkwood, P. B. (2015). *Cyclic lateral loading of monopile foundations in sand*. PhD thesis, University of Cambridge.

Klinkvort, R., Springman, S., and Hededal, O. (2012). Scaling issues in centrifuge modelling of monopiles. *International Journal of Physical Modelling in Geotechnics*, 13(2):38–50.

Klinkvort, R. T. (2012). *Centrifuge modelling of drained lateral pile - soil response: Application for offshore wind turbine support structures*. PhD thesis. Technical University of Denmark.

Klinkvort, R. T. and Hededal, O. (2012). Lateral response of monopile supporting an offshore wind turbine. *Proceedings of the Institution of Civil Engineers - Geotechnical Engineering*, 166(2):147–158.

Koh, J. H. and Ng, E. Y. (2016). Downwind offshore wind turbines: Opportunities, trends and technical challenges. *Renewable and Sustainable Energy Reviews*, 54:797–808.

Lauder, K. (2010). *The performance of pipeline ploughs*. PhD thesis. University of Dundee-Dundee, UK.

LeBlanc, C., Byrne, B. W., and Houlsby, G. T. (2010a). Response of stiff piles in sand to long-term cyclic lateral loading. *Géotechnique*, 60(2):79–90.

LeBlanc, C., Byrne, B. W., and Houlsby, G. T. (2010b). Response of stiff piles to random two-way lateral loading. *Géotechnique*, 60(9):715–721.

Lesny, K. and Wichtmann, T. (2006). Finite-Element-Modelling of Large Diameter Monopiles for Offshore Wind Energy Converters. *Proc. GeoCongress 2006*, pages 1–6.

Li, Z. S., Thorel, L., and Blanc, M. (2020). Using fbgs to estimate the horizontal response of a monopile in a geotechnical centrifuge. *International Journal of Physical Modelling in Geotechnics*, 20:164–174.

Lin, S. S. and Liao, J. (1999). Permanent strains of piles in sand due to cyclic lateral loads. *Journal of Geotechnical and Geoenvironmental Engineering*, 125(9):798–802.

Little, R. L. and Briaud, J.-L. (1988). Full scale cyclic lateral load tests on six single piles in sand. *Miscellaneous Paper*, pages 1–191.

Long, J. and Vanneste, G. (1994). Effects of Cyclic Lateral Loads on Piles in Sand. *Journal of Geotechnical Engineering*, 120(1):225–244.

Malhotra, S. (2007). Design and Construction Considerations for Offshore Wind Turbine Foundations. *International Conference on Offshore Mechanics and Arctic Engineering*, pages 635–647.

Matlock, H. and Reese, L. (1960). Generalized solutions for laterally loaded piles. *Journal of Soil Mechanics and Foundation Division*, 85(5):1220–1248.

McAdam, R. A., Byrne, B. W., Houlsby, G. T., Beuckelaers, W. J. A. P., Burd, H. J., Gavin, K. G., Igoe, D. J. P., Jardine, R. J., Martin, C. M., Muir Wood, A., Potts, D. M., Skov Gretlund, J., Taborda, D. M. G., and Zdravković, L. (2020). Monotonic laterally loaded pile testing in a dense marine sand at dunkirk. *Géotechnique*, 70(11):986–998.

Murchison, J. M. and O'Neill, M. W. (1984). Evaluation of p-y relationships in cohesionless soils. *Analysis and design of pile foundations: Proceedings of a symposium sponsored by the ASCE Geotechnical Division*, pages 174–197.

Nanda, S., Arthur, I., Sivakumar, V., Donohue, S., Bradshaw, A., Keltai, R., Gavin, K., Mackinnon, P., Rankin, B., and Glynn, D. (2017). Monopiles subjected to uni- and multi-lateral cyclic loading. *Proceedings of the Institution of Civil Engineers - Geotechnical Engineering*, 170(3):246–258.

Oh, K.-Y., Nam, W., Ryu, M., Kim, J.-Y., and Epureanu, B. (2018). A review on the foundation of offshore wind energy convertors: current status and future perspectives. *Renewable and Sustainable Energy Reviews*, 88.

Parker, F. and Reese, L. C. (1970). Experimental and analytical studies of behavior of single piles in sand under lateral and axial loading.

Peralta, P. and Achmus, M. (2010). An experimental investigation of piles in sand subjected to lateral cyclic loads. *Proc. 7th International Conference on Physical Modelling in Geotechnics*, pages 985–990.

Poulos, H. and Hull, T. (1989). The Role of Analytical Geomechanics in Foundation Engineering. *Foundation Engineering: Current Principles and Practices*, pages 1578–1606.

Poulos, H. G. (1971). Behavior of Laterally Loaded Piles: 1-Single Piles. *Journal of Soil Mechanics and Foundations Division*, 97(5):711–731.

Prasad, Y. V. S. N. and Chari, T. R. (1999). Lateral capacity of model rigid piles in cohesionless soils. *Soils and Foundations*, 39(2):21–30.

Randolph, M. and Gourvenec, S. (2017). *Offshore Geotechnical Engineering*. CRC Press.

Randolph, M. F. (1981). The response of flexible piles to lateral loading. *Géotechnique*, 31(2):247–259.

Reddy, K. and Ayothiraman, R. (2015). Experimental studies on behavior of single pile under combined uplift and lateral loading. *Journal of Geotechnical and Geoenvironmental Engineering*, 141:04015030.

Reese, L., Cox, W., and Koop, F. (1974). Analysis of Laterally Loaded Piles in Sand. *Proc. Offshore Technology Conference*, pages 473–483.

Reese, L. C. and Van impe, W. F. (2011). *Single Piles and Pile Groups Un - Lymon C. Reese-1*. Taylor & Francis Group, LLC, 2nd edition.

Remaud, D. (1999). Pieux sous charges laterales: etude experimentale de l'effet de groupe. L'Ecole Centrale de Nantes.

Schofield, A. N. (1980). Cambridge Geotechnical Centrifuge Operations. *Géotechnique*, 30(3):227–268.

Sørensen, S. P. H. (2012). *Soil-Structure Interaction for Non-Slender, Large-Diameter Offshore Monopiles*. PhD thesis, Aalborg University.

Su, D. and Yan, W. M. (2013). A multidirectional p–y model for lateral sand–pile interactions. *Soils and Foundations*, 53(2):199–214.

Suzuki, P., Lehane, B., Zania, V., and Klinkvort, R. T. (2018). Empirical approach based on centrifuge testing for cyclic deformations of laterally loaded piles in sand. *Géotechnique*, 69:1–32.

Taylor, R. N. (1995). *Geotechnical centrifuge technology*. Blackie Academic and Professional, 1 edition.

Terzaghi, K. (1955). Evaluation of Coefficients of Subgrade Reaction. *Geotechnique*, 5(4):297–326.

Vaid, Y. and Negussey, D. (1984). Lateral capacity of model rigid piles in cohesionless soils. *Soils and Foundations*, 24(2):101–105.

Veric, A. B. (1961). Beams on elastic subgrade and the Winkler's hypthesis. *Proc. 5th Iinternational conference on soil mechanics and foundation engineering*, pages 845–850.

Wang, H., Lehane, B., Bransby, M., Askarinejad, A., Wang, L., and Hong, Y. (2022). A simple rotational spring model for laterally loaded rigid piles in sand. *Marine Structures*, 84:103225.

Ward, I. P. (2016). Natural frequency analysis of offshore wind turbine monopiles. *Engineering and Computational Mechanics*, 169(EM4):196–208.

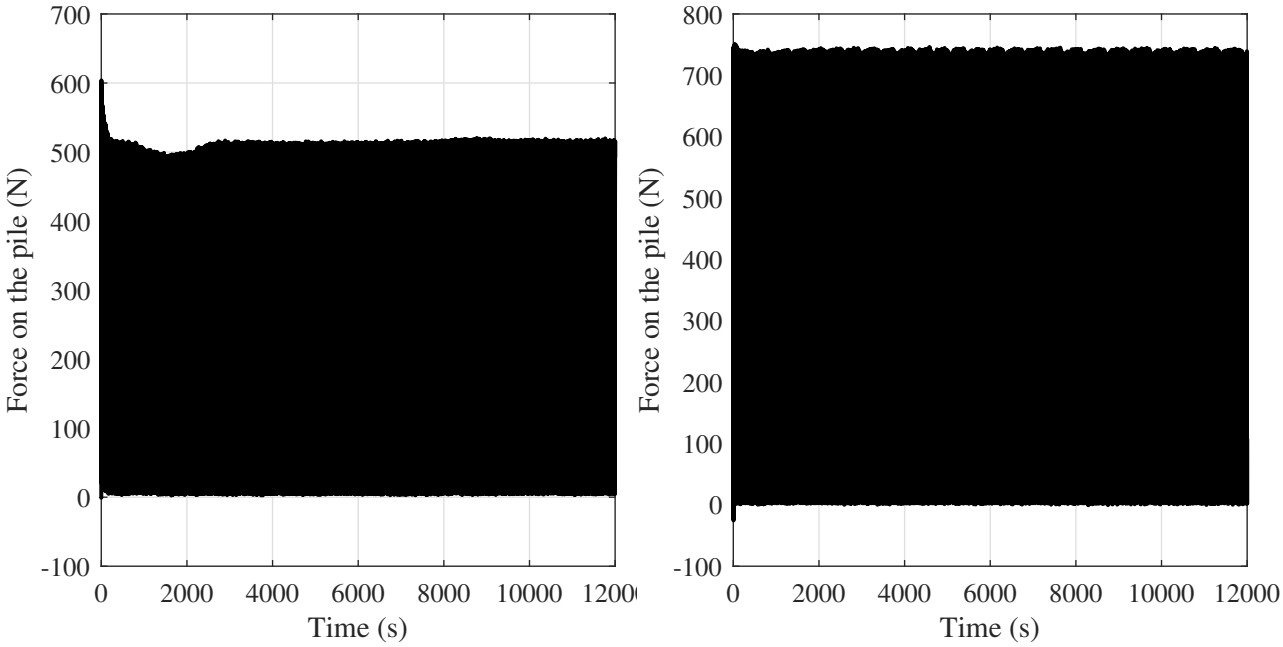
Winkler, E. (1867). Die lehre von elastizitat und festigkeit (on elasticity and fixity). dominicus, prague.

Yang, K. and Liang, R. (2006). Methods for deriving p-y curves from instrumented lateral load tests.

Zhang, L., Silva, F., and Grismala, R. (2005). Ultimate Lateral Resistance to Piles in Cohesionless Soils. *Journal of Geotechnical and Geoenvironmental Engineering*, 131(1):78–83.

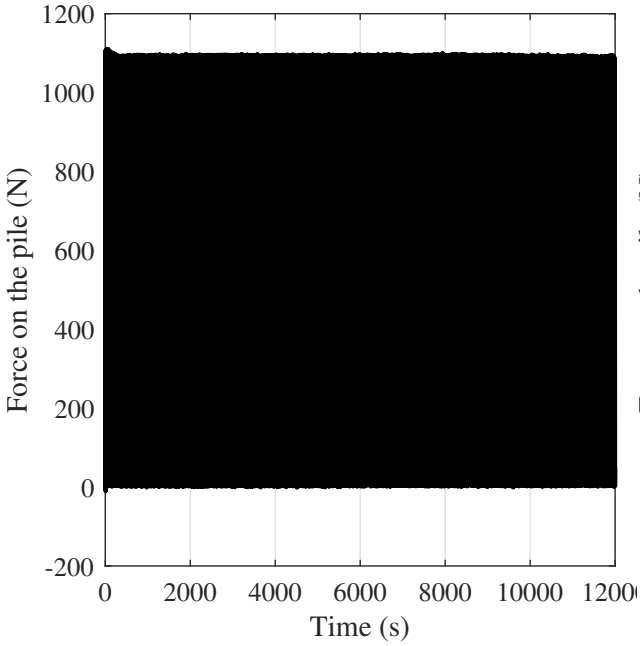
Appendix A

Figures: load and pile head displacement during tests

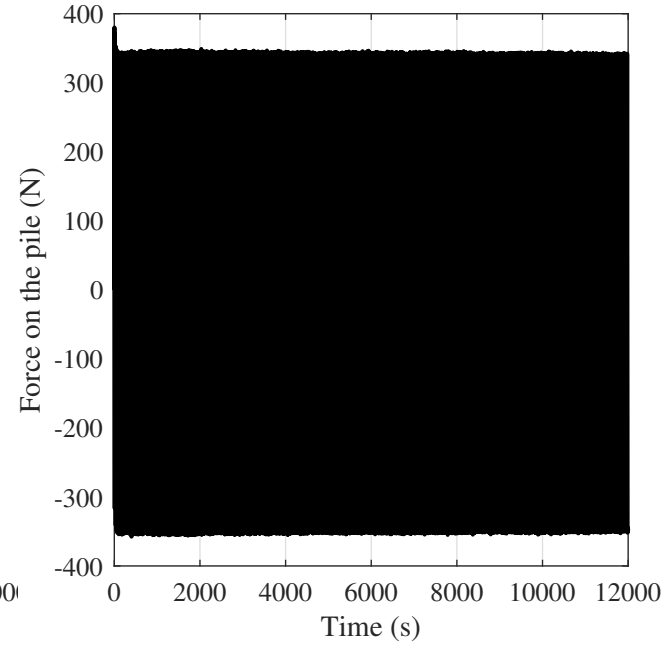


(a) kc01

(b) kc02

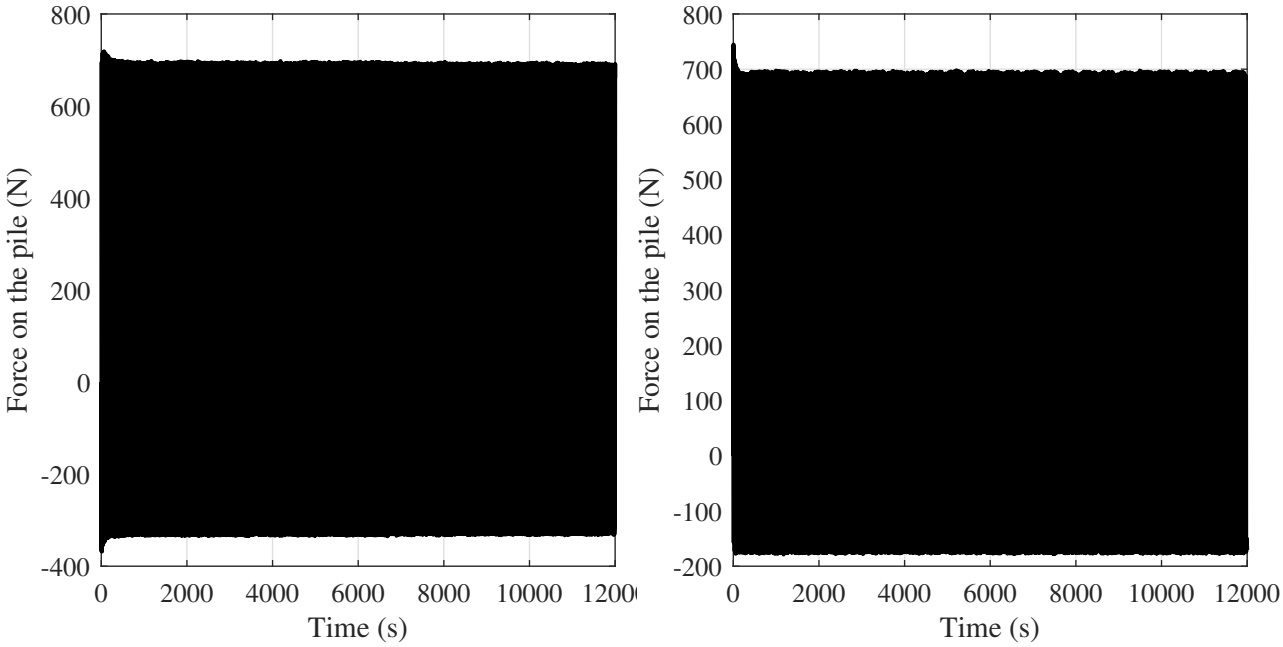


(c) kc03



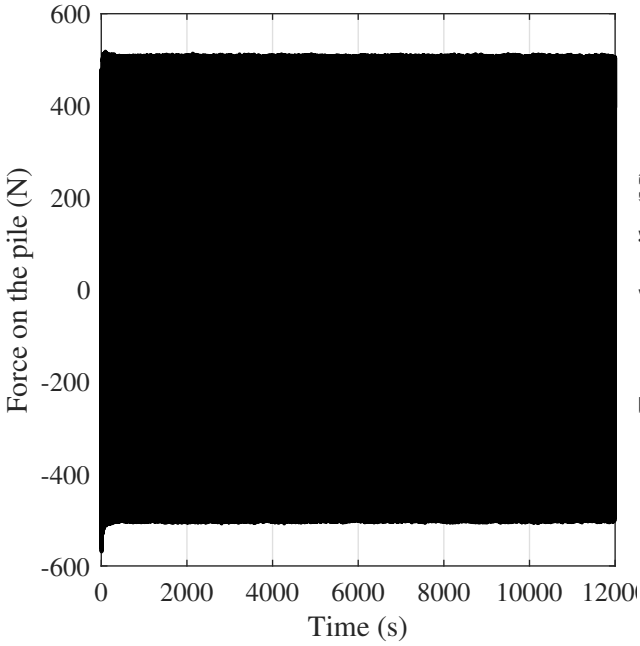
(d) kc04

Figure A.1: load during tests

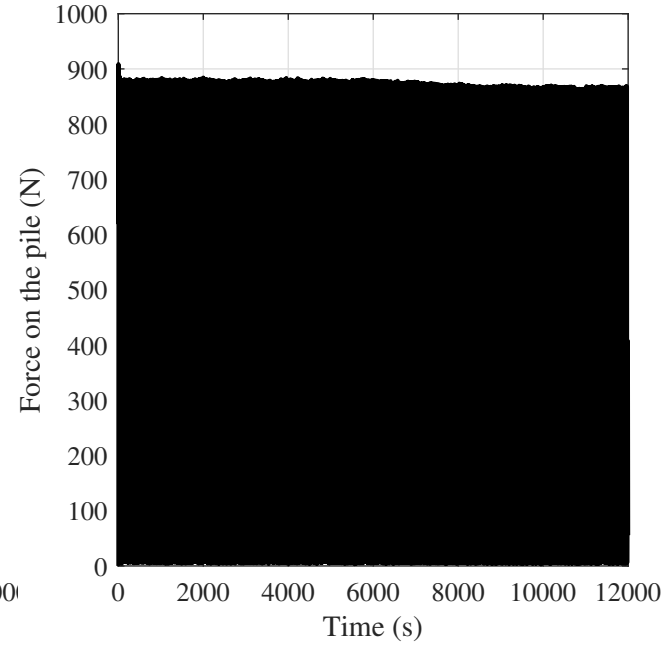


(a) kc05

(b) kc06

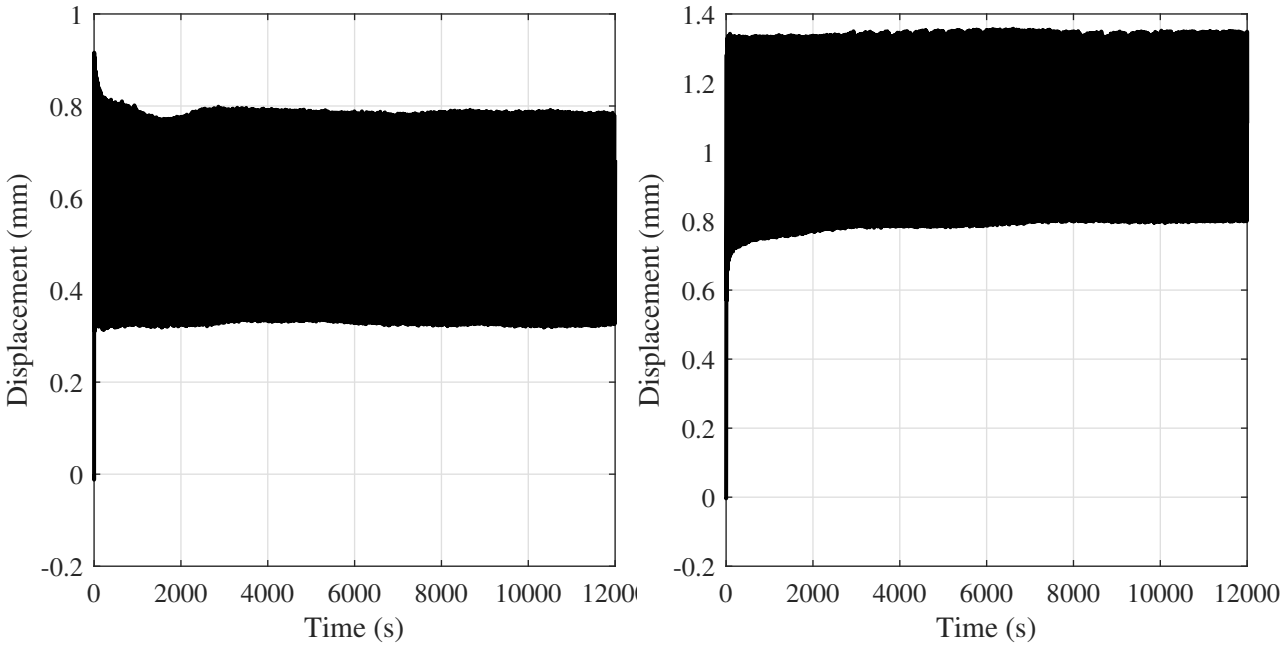


(c) kc07



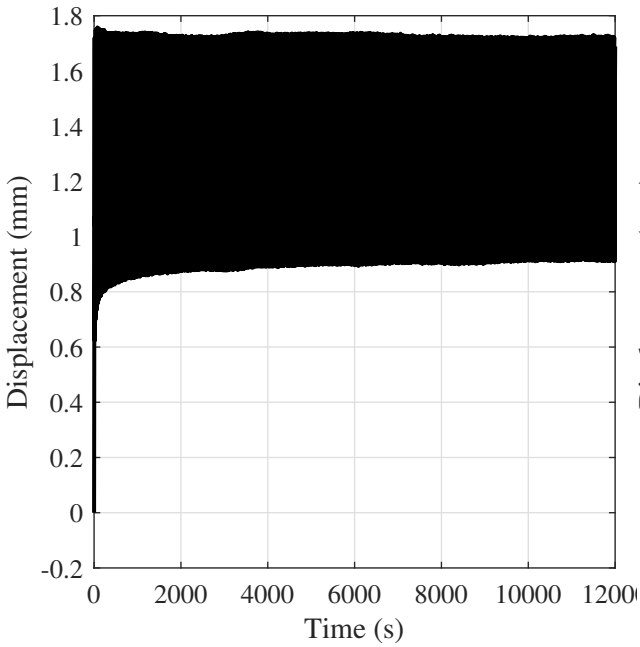
(d) kc08

Figure A.2: load during tests (continued)

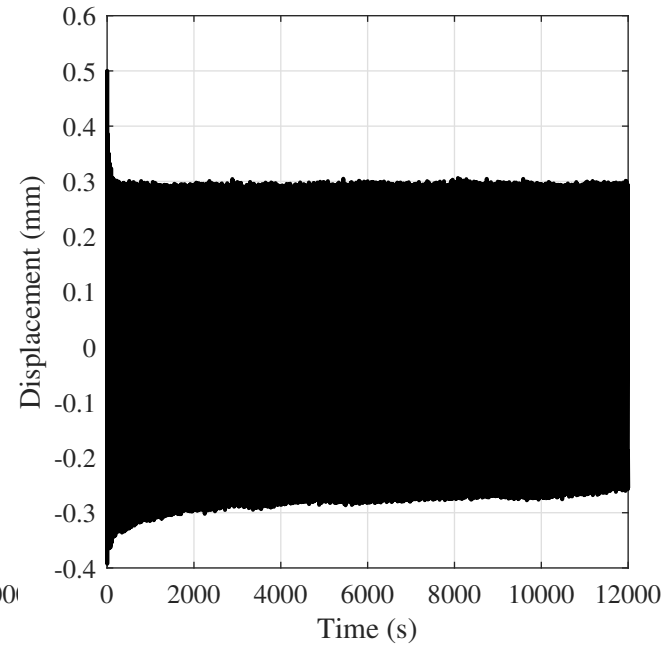


(a) kc01

(b) kc02

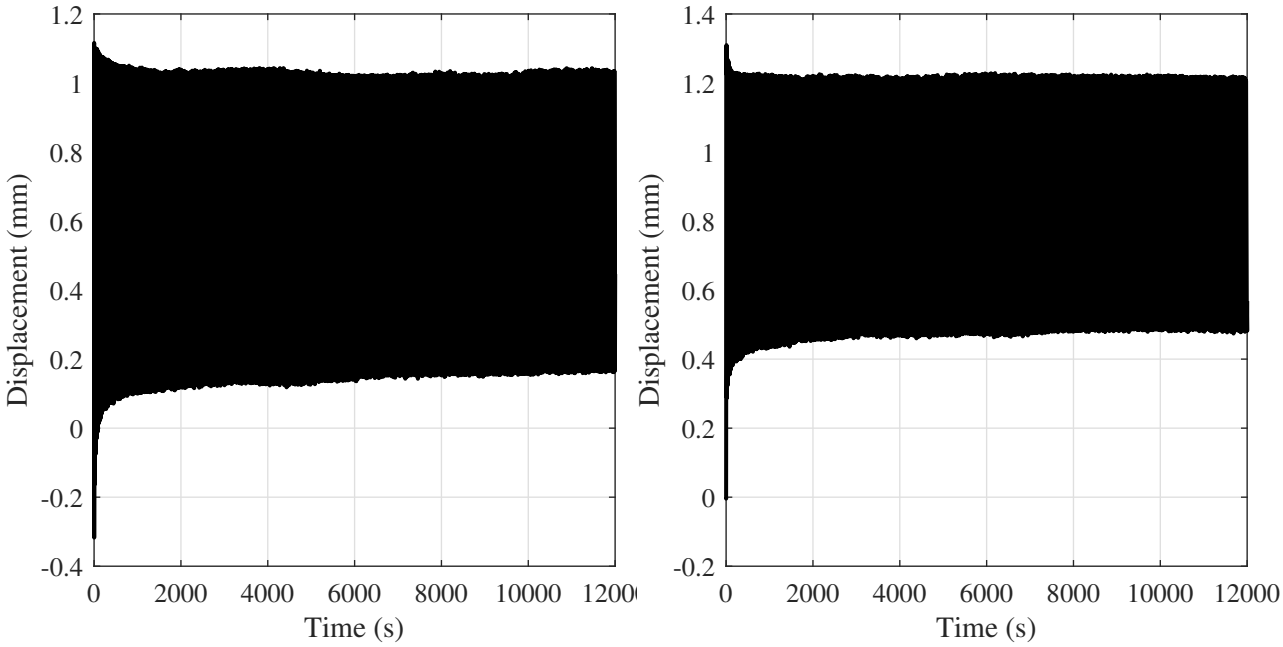


(c) kc03



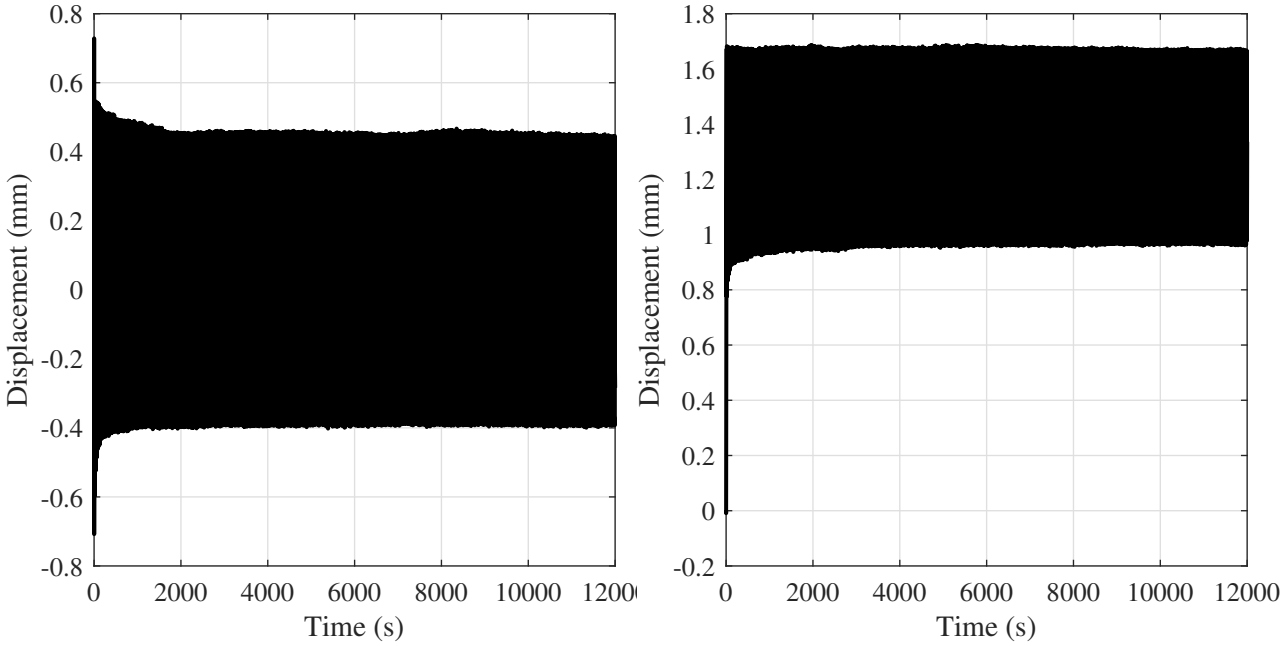
(d) kc04

Figure A.3: Pile head displacement during tests



(a) kc05

(b) kc06



(c) kc07

(d) kc08

Figure A.4: Pile head displacement during tests (continued)